DOE/ET-53088-341 IFSR #341

Two Case Studies of Stochastic Transport: Anomalous Transport in Two Drift Waves, and Collisionless Reconnection

Isidoros Doxas
Institute for Fusion Studies
The University of Texas at Austin
Austin, Texas 78712

September 1988

Chapter 1

INTRODUCTION

The recent understanding that simple dynamical systems with few degrees of freedom can exibit chaotic behavior, is changing the way we approach problems that would traditionally have been considered too complicated for analytical study and tractable only by a statistical approach in which the relevant transport coefficients would be phenomenological. We are now justified to assume that, at least the qualitative features of these complicated systems, can be well approximated by simple, low degree of freedom dynamical systems that are more amenable to analytical techniques at our disposal. Here we study two such simple systems. They represent well known and quite distinct problems of plasma theory, and yet both the mechanism that determines their macroscopic behavior and the mathematical techniques we use to analyze them are remarkably similar.

In Part I we study particle transport in two drift waves. Single particle motion in one drift wave is integrable and has been solved analytically (Horton, 1981). The phase space consists of an infinite two-dimentional lattice of counterrotating rolls separated by a separatrix (Fig. 2.1). The particles cannot cross the separatrix so that any given particle is confined to motion within a single roll. We can, without loss of generality, assume that the amplitude of the second wave is smaller than the first, transform to a frame in which

Two Case Studies of Stochastic Transport: Anomalous Transport in Two Drift Waves, and Collisionless Reconnection

Isodoros Doxas

The recent understanding that simple dynamical systems with few degrees of freedom can exibit chaotic behavior, is changing the way we approach problems that would traditionally have been considered too complicated for analytical study and tractable only by a statistical approach in which the relevant transport coefficients would be phenomenological. We are now justified to assume that, at least the qualitative features of these complicated systems, can be well approximated by simple, low degree of freedom dynamical systems that are more amenable to analytical techniques at our disposal. Here we study two such simple systems. They represent well known and quite distinct problems of plasma theory, and yet both the mechanism that determines their macroscopic behavior and the mathematical techniques we use to analyze them are remarkably similar.

TWO CASE STUDIES OF STOCHASTIC TRANSPORT:
ANOMALOUS TRANSPORT IN TWO DRIFT WAVES,
AND COLLISIONLESS RECONNECTION.

APPROVED BY
SUPERVISORY COMMITTEE:

C. Wendell Horton Jr.

James F. Main

Philip J. Morrison

L. E. Reichl

V. Urbanek

To my wife Kathy

and my parents *Γιῶργο* and *Μαργαρίτα*.

TWO CASE STUDIES OF STOCHASTIC TRANSPORT: ANOMALOUS TRANSPORT IN TWO DRIFT WAVES, AND COLLISIONLESS RECONNECTION.

by

ISIDOROS DOXAS, M.A.

DISSERTATION

Presented to the Faculty of the Graduate School of

The University of Texas at Austin

in Partial Fulfillment

of the Requirements

for the Degree of

DOCTOR OF PHILOSOPHY

THE UNIVERSITY OF TEXAS AT AUSTIN

August, 1988

Acknowledgments

I thank my adviser Wendell Horton for all his help, guidance, support, patience, faith and advice these past four years. He was a constant source of encouragement in the endless ups and downs of graduate-student life and a reassuring reservoir of scientific advice in the numerous times that progress was stalled and no apparent solution was in sight. I also want to thank Spilios Riyopoulos, Bruce Scott, Hamid Biglari and Peter Lyster for valuable discussions during long hours of lunch or coffee breaks. At least as much progress was made at "Captain Quakenbush's Intergalactic Cafe and Espresso" or the Union patio, as in front of my desk. I particularly wish to thank Bruce Scott for patiently guiding me through the MFE operating system and helping me with the finer points of vectorization and parallelism.

I finally want to thank my wife Kathy for all her love and support, and my parents *Γιῶργο* and *Μαργαρίτα* for their unwavering support through some rough times. I suspect that, for all the brave faces they put on when they let me leave the country in search of a better education, they didn't expect that ten years later I would be farther from home than ever, and planning to go even further. *Ευχαριστῶ*.

ISIDOROS DOXAS

The University of Texas at Austin

August, 1988

Table of Contents

List of Figures

the large wave is stationary, and treat the small one as a perturbation. The hamiltonian is no longer time independent and energy is no longer conserved, so a particle is no longer confined to a single roll. The change in the energy of a particle that moves close to the separatrix from the vicinity of one X-point to the next is given by

$$\Delta H = \int_{-T/8}^{T/8} \frac{dH}{dt}\, dt \quad .$$

where T is the particle's period of oscillation around the O-point. We will see that most of the contribution to ΔH comes from a short interaction time around $t = 0$. The particle motion is therefore regular most of the time, except for a small 'kick' the particle receives at the midpoint of its trajectory. We calculate the magnitude of the kick, which depends on the relative phase of the two oscillations around the O-point and around the time torus at the time of the kick, and relate the particle motion near the separatrix to the standard map.

In Part II we study collisionless magnetic reconnection by considering single particle motion in the simplest tearing mode configuration. Since most of the measurements in the plasma collisionless regime come from the geomagnetic tail, we chose a magnetic field configuration that closely parallels that of the magnetotail, given by

$$\begin{aligned} B_x &= B_0 \tanh\left(\frac{z}{a}\right) \\ B_z &= B_0 b + B_0 \psi_0 k \sin(kx) e^{\gamma t} \\ E_y &= B_0 \psi_0 \frac{\gamma}{c} \cos(kx) e^{\gamma t} \end{aligned}$$

where x is the earthward direction, z is northward and y is from dawn to dusk (Fig. 3.1). The parameter ψ_0 is the amplitude of the tearing mode, k its wavenumber, γ its growth rate, and a is the scale length over which the horizontal field reverses direction.

For the tearing instability we need some form of dissipation. In resistive MHD theory (Furth et. al. 1963) the dissipation is provided by Coulomb collisions. In the collisionless regime in which we are interested, we have to find some other mechanism to provide the dissipation. In an analysis very similar to that in Part I, we see that the particle magnetic moment, which is adiabatically conserved outside the reversal layer, changes value in small increments as the particle crosses the reversal layer. For $\kappa > 1$, where

$$\kappa = b\sqrt{\frac{a}{\rho_0}}$$

with ρ_0 the particle gyroradius in the asymptotic field, we can calculate the change in the magnetic moment in half a particle bounce period

$$\Delta\mu = \int_{-T_b/4}^{T_b/4} \frac{d\mu}{dt}\, dt.$$

The functional form of the result is very similar to that for the change in the particle energy ΔH in Part I. The process is equivalent to velocity-space diffusion and can be used as an effective dissipation for the tearing instability (Büchner and Zelenyǐ, 1986, 1987). The effective collisionless dissipation arises from the scattering of the electrons out of the direction of acceleration of the applied electric field.

We see therefore that two different physical problems can be modeled by similar, simple dynamical systems which, although they are strictly hamiltonian, can exibit behavior similar to collisional systems. We exploit that similarity to develop methods that either describe anomalous transport from $\vec{E} \times \vec{B}$ motion or provide the collisionless dissipation necessary for magnetic reconnection instability.

Part I

STOCHASTIC TRANSPORT IN TWO DRIFT WAVES

Chapter 2

THE HAMILTONIAN FOR DRIFT WAVES

Drift wave instabilities arising from plasma density gradients provide a possible mechanism for anomalous particle transport across field lines in magnetic confinement devices. These instabilities, whose characteristic frequencies are much lower than the electron or ion gyrofrequency, move particles across field lines via the $\vec{E} \times \vec{B}$ drift. Test particle motion in a single drift wave is integrable and can only produce localized convective motion inside a cell with no net transport (Horton, 1981), but if a second wave with a different phase velocity is introduced, particle motion becomes stochastic and particles can move from cell to cell in a diffusion-like process.

The first attempts to evaluate the effective diffusion coefficient were based on quasilinear theory (eg. Kadomtsev, 1965) but were unrealistic in their prediction that only the zero frequency component of the spectrum can cause net transport. Dupree, (1967) did a nonlinear calculation of the effective diffusion coefficient and found that it scales linearly with the amplitude of the electrostatic fluctuations. Horton, (1985) also studied single particle motion in a two wave system and derived the corresponding Chirikov-overlap criterion for the onset of stochasticity. Recently Kleva and Drake, (1984) conducted an extensive numerical study of stochastic particle motion in a two wave system. Here we review briefly the one wave system, derive an expression for the effective diffusion coefficient in terms of the perturbing wave parameters and

compare our predictions with numerical simulations.

In Section 2.1 we give a brief account of test particle hamiltonian motion in a single wave. In Section 2.2 we introduce a second wave to the system. The hamiltonian becomes time dependent and particle motion becomes stochastic. We calculate the change in energy of the particle as it moves close to the separatrix from the vicinity of one X-point to the next and relate particle motion to the standard map.

2.1 The Unperturbed System; One Wave.

The equations of motion for the guiding center of an ion or trapped electron with $\omega \gg k_{\|} v_j$ that is $\vec{E} \times \vec{B}$ drifting in an electric field given by the electrostatic potential $\phi(x, y, t)$ are

$$\begin{aligned} \frac{dx}{dt} &= -\frac{cT_e}{eB}\frac{\partial \phi}{\partial y} \\ \frac{dy}{dt} &= \frac{cT_e}{eB}\frac{\partial \phi}{\partial x} \end{aligned} \tag{2.1}$$

where T_e is the electron thermal energy (Horton, 1981). Here ϕ is measured in units of T_e/e. We are considering a slab geometry, in which the x-direction would correspond to the radial direction in a Tokamak, while the y-direction is in the $\hat{x} \times \hat{b}$ direction and corresponds to the poloidal direction in the limit $B_\theta/B_\phi = \epsilon/q \ll 1$. The above equations of motion are equivalent to a hamiltonian system with hamiltonian $H(x, y, t) = (cT_e/eB)\phi$ where y is the canonical position and x the canonically conjugate momentum. For an electrostatic potential with one wave, ϕ is given by

$$\phi = -\frac{eE_r}{T_e}x + a\sin(k_1 x)\cos[q_1(y - v_1 t)] \tag{2.2}$$

where E_r is the radial electric field, a the wave amplitude measured in units of the electron temperature, and v_1 its velocity in the (poloidal) y-direction. The wave is stationary in the (radial) x-direction. Substituting ϕ into the hamiltonian we obtain

$$\begin{aligned} H &= -\frac{cE_r}{B}x + \frac{caT_e}{eB}\sin(k_1 x)\cos[q_1(y - v_1 t)] \\ \dot{x} &= -\frac{\partial H}{\partial y} = \frac{caT_e}{eB}q_1 \sin(k_1 x)\sin[q_1(y - v_1 t)] \\ \dot{y} &= \frac{\partial H}{\partial x} = -\frac{cE_r}{B} + \frac{caT_e}{eB}k_1 \cos(k_1 x)\cos[q_1(y - v_1 t)]. \end{aligned} \tag{2.3}$$

It is convenient to transform to a frame moving with the wave, so that the hamiltonian becomes time-independent. To do this we use the generating function $F_2(x', y, t) = x'(y - v_1 t)$ which gives

$$\begin{aligned} x' &= \frac{\partial F_2}{\partial y} = x \\ y' &= \frac{\partial F_2}{\partial x'} = y - v_1 t \\ H' &= H + \frac{\partial F_2}{\partial t} \end{aligned}$$

so that in the new canonical coordinates

$$\begin{aligned} H &= -\left(\frac{cE_r}{B} + v_1\right)x + \frac{caT_e}{eB}\sin(k_1 x)\cos(q_1 y) \\ \dot{x} &= \frac{caT_e}{eB}q_1 \sin(k_1 x)\sin(q_1 y) \\ \dot{y} &= -\left(\frac{cE_r}{B} + v_1\right) + \frac{caT_e}{eB}k_1 \cos(k_1 x)\cos(q_1 y) \end{aligned} \tag{2.4}$$

where we have dropped the primes in the new coordinates. If we introduce the dimensionless variables

$$x' = k_1 x \qquad y' = q_1 y$$

$$\tau = \omega_E t = A k_1 q_1 t \qquad A = a\frac{cT_e}{eB}$$

$$H' = \frac{H}{A} \qquad u = -\frac{1}{ak_1}(v_1 - v_E) \qquad v_E = -\frac{cE_r}{B}$$

we finally obtain

$$\begin{aligned} H &= ux + \sin x \cos y \\ \dot{x} &= \sin x \sin y \\ \dot{y} &= u + \cos x \cos y \end{aligned} \tag{2.5}$$

where we have again dropped the primes from the new variables. Time derivatives are taken with respect to $\tau = \omega_E t$, where ω_E is the particle's linear frequency around the O-point. We will henceforth refer to Eqs. 2.5 as the unperturbed system. As mentioned earlier one wave cannot by itself induce anomalous transport, although it can enhance any residual collisional diffusion already present (Rosenbluth et. al., 1987). We will therefore add later a second wave to the system as a perturbation and study its effect on the transport properties of 2.5.

The fixed points of the system are obtained by setting $\dot{x} = \dot{y} = 0$ and, for $|u| < 1$, they are given by

$$\begin{aligned} x_0 &= n\pi \\ y_0 &= 2m\pi \pm \cos^{-1}[(-1)^{n+1}u] \quad X - points \\ \\ x_0 &= 2m\pi \pm \cos^{-1}[(-1)^{n+1}u] \\ y_0 &= n\pi \qquad\qquad\qquad\qquad O - points \end{aligned} \tag{2.6}$$

where m and n are integers. Expanding around the fixed points we get

$$\begin{aligned} \vec{x} &= \vec{x}_0 + \delta\vec{x}e^{\pm\sqrt{1-u^2}\tau} \quad X - point \\ \vec{x} &= \vec{x}_0 + \delta\vec{x}e^{\pm i\sqrt{1-u^2}\tau} \quad O - point \end{aligned} \tag{2.7}$$

so that the linear frequency of oscillations around the elliptic fixed points is

$$\frac{\omega_0^b}{\omega_E} = \sqrt{1-u^2} \tag{2.8}$$

while the linear rate of divergence from the hyperbolic fixed point along the unstable manifold is

$$\frac{\lambda_0}{\omega_E} = \sqrt{1-u^2} \tag{2.9}$$

The parameter $u = -(v_1 - v_E)/ak_1$ is the trapping parameter. We distinguish the following cases according to the value of u (cf. Fig. 2.1).

For $u < -1$ all orbits are open and the particles are streaming in the $-y$-direction (cf. Fig. 2.1-a).

For $u = -1$ fixed points appear at $(2n\pi, 2m\pi)$ and $([2n+1]\pi, [2m+1]\pi)$ (points A and E in Fig. 2.1-a). The fixed points are neither elliptic nor hyperbolic; $\dot{x} = \dot{y} = 0$ in first order away from the fixed points.

For $-1 < u < 0$ a pair of X-points and a pair of O-points bifurcate from the fixed points A and E. The X-points move vertically and the O-points horizontally away from the center (cf. Fig. 2.1-b). Trapped-particle regions are formed.

For $u = 0$ the X- and O-points form a regular lattice. The whole of phase space is enclosed in the trapped regions (cf. Fig. 2.1-c).

For $0 < u < 1$ the X-points continue to move vertically and the O-points horizontally (cf. points B, D, G and H in Fig. 2.1-d). A new streaming region appears.

For $u = 1$ the X- and O-points merge again into a single fixed point. In Fig. 2.1-d points B, D, K and L will all merge at point C.

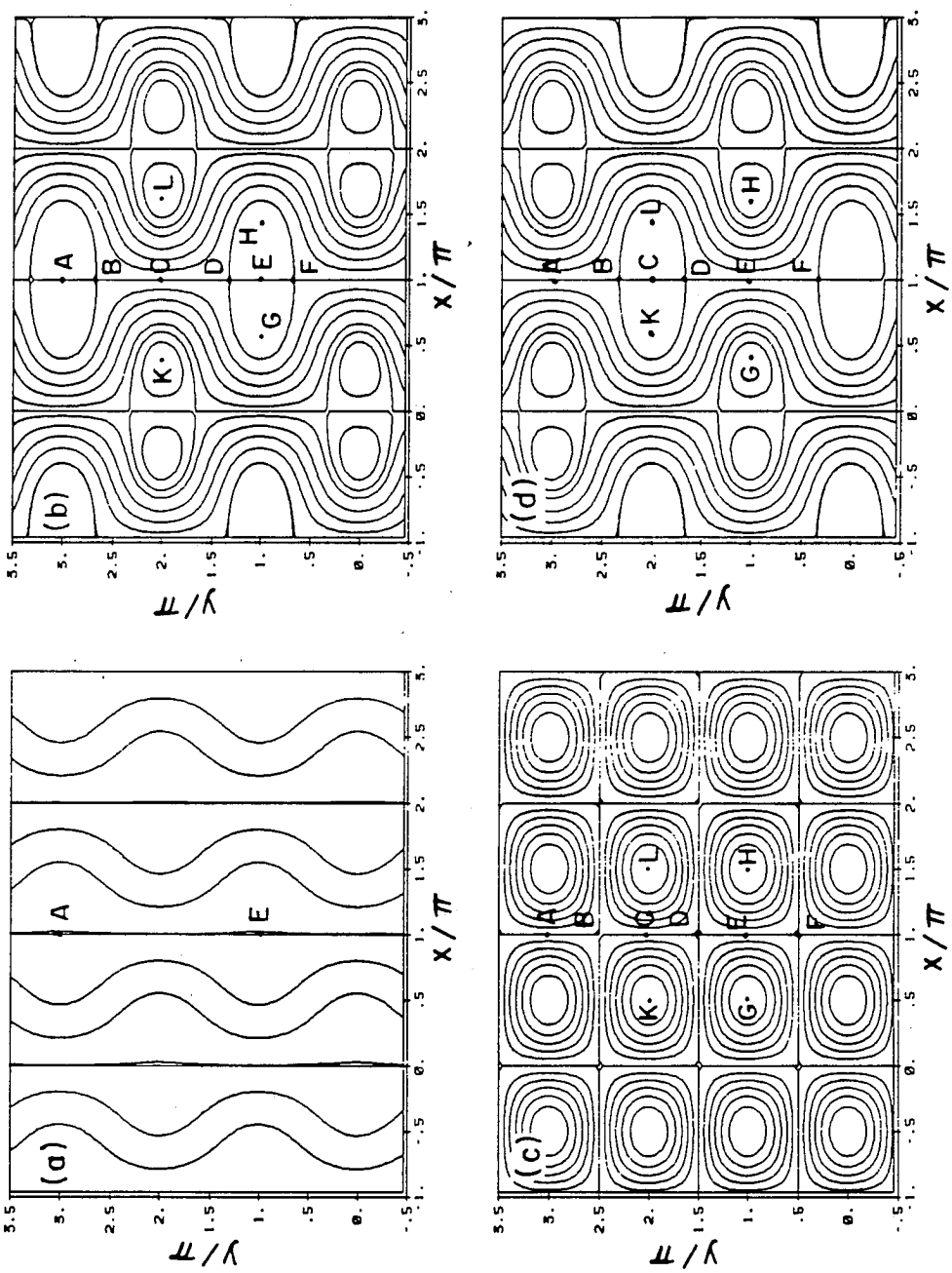

Figure 2.1: Phase space plot for the unperturbed hamiltonian. **a)** $u = -1.5$ b) $u = -0.5$ c) $u = 0$ d) $u = 0.5$.

For $u > 1$ all the particles are streaming in the $+y$-direction.

The equation of the separatrix can be obtained by noting that at an X-point $H_s = nu\pi$. Substituting this into 2.5 we get

$$nu\pi = ux + \sin x \cos y \tag{2.10}$$

which is the equation of the separatrix. If we now choose a new set of coordinates with origin at the point $(n\pi, m\pi)$ (eg. point C or E in Fig. 2.1) so that $x = n\pi + x'$ and $y = m\pi + y'$, the equations of motion 2.5 give

$$\begin{aligned} \dot{x}' &= (-1)^{n+m} \sin x' \sin y' \\ \dot{y}' &= u + (-1)^{n+m} \cos x' \cos y' \end{aligned} \tag{2.11}$$

and the equation of the separatrix 2.10 gives

$$ux' + (-1)^{n+m} \sin x' \cos y' = 0. \tag{2.12}$$

If we now substitute 2.12 into 2.11 we obtain

$$\begin{aligned} \dot{x} &= \pm\sqrt{\sin^2 x - u^2 x^2} \\ \dot{y} &= u - ux \cot x \end{aligned} \tag{2.13}$$

where we have dropped the primes in the new coordinates. Eqs. 2.13 are the equations of motion for a particle moving along the separatrix. For the straight-line part of the separatrix (A–F in Fig. 2.1-d) we have $x = n\pi$ which gives

$$\begin{aligned} \dot{x} &= 0 \\ \dot{y} &= u + (-1)^{n+m} \cos y \end{aligned}$$

which can be integrated to give

$$\tan\left(\frac{y}{2}\right) = \frac{(-1)^{n+m} + u}{\sqrt{1-u^2}} \tanh\left(\frac{\sqrt{1-u^2}}{2}\tau\right). \tag{2.14}$$

Eq. 2.14 is the equation of motion of the particle along the straight-line part of the separartix. For $u > 0$ the centers of the long part of the separatrix (point E in Fig. 2.1) are given by $n + m = 2q$. We then have

$$\begin{aligned}
\tau = 0 \longrightarrow \quad & y = 0 \quad \longleftrightarrow \mathrm{E} \\
\tau \to \infty \longrightarrow \quad & \frac{y}{2} = \tan^{-1}\left(\sqrt{\frac{1+u}{1-u}}\right) = \frac{\cos^{-1}(-u)}{2} \longleftrightarrow \mathrm{D} \\
\tau \to -\infty \longrightarrow \quad & \frac{y}{2} = -\tan^{-1}\left(\sqrt{\frac{1+u}{1-u}}\right) = -\frac{\cos^{-1}(-u)}{2} \longleftrightarrow \mathrm{F}
\end{aligned} \tag{2.15}$$

which gives a motion in the $+y$-direction, in agreement with the sign of $\dot{y}$ from 2.5. Similarly we see that the direction of motion through the point $n + m = 2q + 1$ (point C in Fig. 2.1) is in the $-y$-direction. For $u < 0$ the short and long parts of the separatrix are interchanged, but the direction of the motion through points C and E remains unchanged (cf. Fig. 2.1).

We finally estimate the fractional area occupied by the islands. From the equation of the curved part of the separatrix (Eq. 2.12 with $n+m = 2q+1$ if $u > 0$, $n + m = 2q$ if $u < 0$) we see that

$$y = \pm \cos^{-1}\left(\frac{|u|x}{\sin x}\right)$$

so that the fractional area occupied by an island is given, in units of π^2, by

$$A(u) = \frac{2}{\pi^2}\int_0^{x_m} dx \, \cos^{-1}\left(\frac{|u|x}{\sin x}\right) \tag{2.16}$$

where x_m is given by $y = 0$, i.e. by $\sin x_m + u x_m = 0$. The integral is very closely given by $A(u) = 1 - u^{0.6}$ (cf. Fig. 2.2) throughout the range $0 < |u| < 1$. The integral $A(u)$ is the action bounded by the separatrix orbit. It is the maximum action for the $\vec{E} \times \vec{B}$ trapped particles. For $u \to 0$ all orbits are trapped.

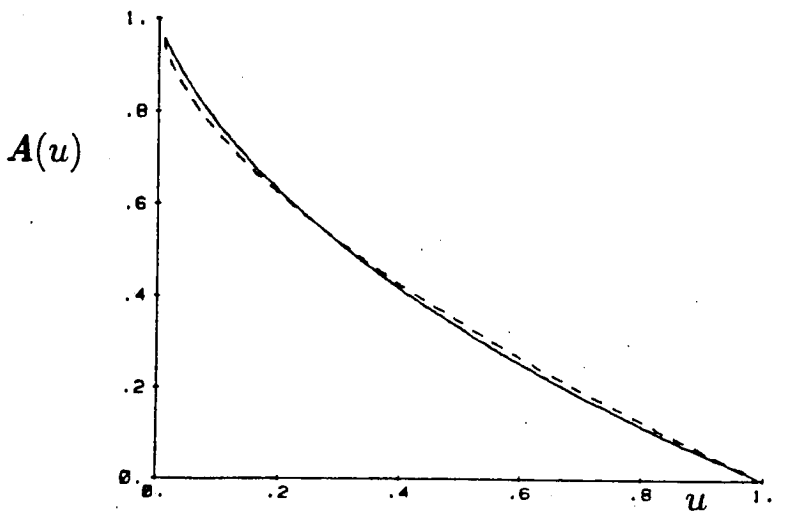

Figure 2.2: $A(u)$ as a function of u. The solid line is the exact expression, the dashed line is given by $A(u) = 1 - u^{0.6}$.

2.2 The Two Wave System.

We will now add a second wave to the electrostatic potential ϕ and treat it as a perturbation. The potential (Eq. 2.2) now becomes

$$\begin{aligned} \phi &= -\frac{eE_r}{T_e}x + a_1 \sin(k_1 x)\cos[q_1(y - v_1 t)] \\ &\quad + a_2 \sin(k_2 x + \alpha)\cos[q_2(y - v_2 t) + \beta] \end{aligned} \tag{2.17}$$

with $a_2 < a_1$. We can again transform into the frame of wave-1 to obtain

$$\begin{aligned} H &= -\left(\frac{E_r c}{B} + v_1\right)x + a_1 \frac{cT_e}{eB}\sin(k_1 x)\cos(q_1 y) \\ &\quad + a_2 \frac{cT_e}{eB}\sin(k_2 x + \alpha)\cos(q_2[y - (v_2 - v_1)t] + \beta). \end{aligned} \tag{2.18}$$

If we now put

$$-\frac{E_r c}{B} - v_1 = V_E - v_1 = u$$

$$a_1 \frac{cT_e}{eB} = A_1 \quad , \quad a_2 \frac{cT_e}{eB} = A_2$$

and then use the transformation

$$k_1 x = x' \qquad q_1 y = y' \qquad A_1 k_1 q_1 t = \omega_E t = \tau$$

we obtain

$$\begin{aligned} H &= ux + \sin x \cos y + \epsilon \sin(kx + \alpha) \cos[q(y - v\tau) + \beta] \\ \dot{x} &= \sin x \sin y + \epsilon q \sin(kx + \alpha) \sin[q(y - v\tau) + \beta] \\ \dot{y} &= u + \cos x \cos y + \epsilon k \cos(kx + \alpha) \cos[q(y - v\tau) + \beta] \end{aligned} \tag{2.19}$$

where

$$\begin{aligned} k &= \frac{k_2}{k_1} & q &= \frac{q_2}{q_1} \\ \epsilon &= \frac{A_2}{A_1} & H' &= \frac{H}{A_1 k_1} \\ u' &= \frac{u}{A_1 k_1} & v &= \frac{v_2 - v_1}{A_1 k_1} \end{aligned}$$

and we have dropped the primes in the new variables and parameters.

The one wave system in Sec. 2.1 has only one parameter, u, while the two wave system has five independent parameters, u, ϵ, k, q and v. We will henceforth consider 2.19 to be the full system and treat the ϵ term as a perturbation, so we will only consider $\epsilon < 1$. This does not limit the generality of our treatment however, since if $\epsilon > 1$ we can interchange indices $1 \leftrightarrow 2$ in the equation for the potential 2.17 and proceed as before. The equation we will obtain will be identical to 2.19 with

$$x' = kx + \alpha \qquad y' = qy + \beta$$

$$\epsilon' = \frac{1}{\epsilon} \quad k' = \frac{1}{k} \quad q' = \frac{1}{q}$$

$$\alpha' = \frac{-\alpha}{k} \quad \beta' = \frac{-\beta}{q} \quad \tau' = \epsilon k q \tau$$
$$u' = \frac{u - v}{\epsilon k} \qquad v' = \frac{-v}{\epsilon k}$$

where the primes denote the new quantities.

2.2.1 Motion Near the Separatrix

The introduction of the perturbation will cause the particle motion near the separatrix to become stochastic. A particle moving along the straight-line part of the separatrix (eg. from point F to point D in Fig. 2.1) will closely follow the streamlines of the unperturbed system until it reaches point E, in the vicinity of which it will receive a 'kick' (see Appendix A) that will change its energy and will place it on a different streamline, which the particle will follow until the next 'kick', and so on. The magnitude of the change in the energy of a particle as it moves from the vicinity of one X-point to the next is given by

$$\begin{aligned} \Delta H &= \int_{-T/8}^{T/8} \frac{dH}{d\tau}\, d\tau \\ &= \epsilon\Omega \int_{-T/8}^{T/8} \sin(kx(\tau) + \alpha) \sin[qy(\tau) - \Omega\tau + \beta]\, d\tau \end{aligned} \tag{2.20}$$

where $T = 2\pi/\omega(H)$ is the period of a particle with energy H around the O-point, $\Omega = qv$ is the frequency of the perturbation, and we are integrating along the particle trajectory.

For the curved part of the separatrix the integral in Eq. 2.20 is two-dimensional and is hard to evaluate. For trajectories close to the straight-line part of the separartix however, we can approximate $x(\tau)$ and $y(\tau)$ in the expression for ΔH by

$$x = n\pi$$

$$y = m\pi + y_{sx}(\tau)$$

where y_{sx} is given by Eq. 2.14. Since $T \to \infty$ for trajectories close to the separatrix, we can extend the limits of integration to infinity to obtain

$$\Delta H \approx \epsilon\Omega \sin(nk\pi + \alpha) \int_{-\infty}^{\infty} \sin(qy_{sx} - \Omega\tau + \beta)\, d\tau \tag{2.21}$$

in effect substituting the trajectory of a particle near the separatrix by the unperturbed separatrix orbit itself, which is called a homoclinic orbit.

With y_{sx} given by Eq. 2.14 the integral in 2.21 is rather complicated and is analyzed approximately in Horton (1985) by using stationary phase integration. We will follow a slightly different approach here. First we note that, for $u = 0$, the homoclinic orbit is $y_{sx} \approx y'_{sx} = 2\tan^{-1}(e^{\tau}) - \pi/2$. For $u > 0$ the approximation breaks down because

$$\lim_{\tau \to \pm\infty} y_{sx} = \pm \cos^{-1}(-u)$$

while

$$\lim_{\tau \to \pm\infty} y'_{sx} = \pm\frac{\pi}{2}.$$

This suggests that we use

$$y_{sx}(\tau) \approx \frac{\cos^{-1}(-u)}{\pi/2} y'_{sx}(\tau) \tag{2.22}$$

as an approximation to y_{sx} in 2.21. Numerical calculations show that y'_{sx} and $y_{sx}\pi/[2\cos^{-1}(-u)]$ are in very good agreement throughout the range $-1 < u < 1$ as shown in Figs. 2.3 and 2.4. Indeed, if we also evaluate the integral in Eq. 2.21 numerically, first with $y(\tau) = y_{sx}$ and then with $y(\tau) = [2\cos^{-1}(-u)/\pi]y'_{sx}$ we see that the agreement is even better throughout the range $-1 < u < 1$ (cf. Fig. 2.5). This was expected since most of the contribution in ΔH comes from a short interaction time around $\tau = 0$ (see Appendix A),

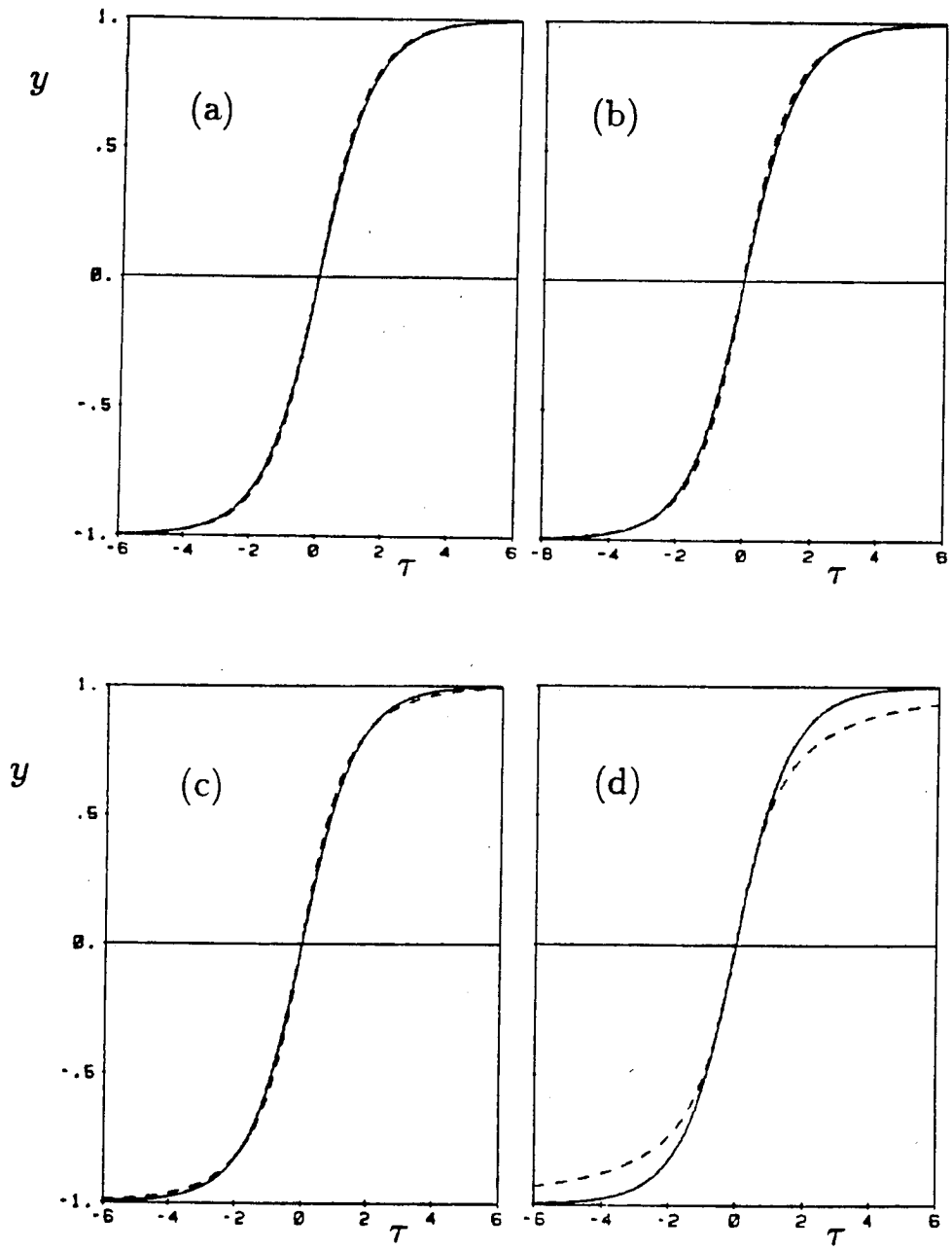

Figure 2.3: Comparative plots of y_{sx} and y'_{sx} as functions of τ. The solid line is $y(\tau) = 2y'_{sx}$,the dashed line is for $y(\tau) = y_{sx}\pi/\cos^{-1}(-u)$. a) $u = 0.20$, b) $u = 0.50$, c) $u = 0.70$, d) $u = 0.99$.

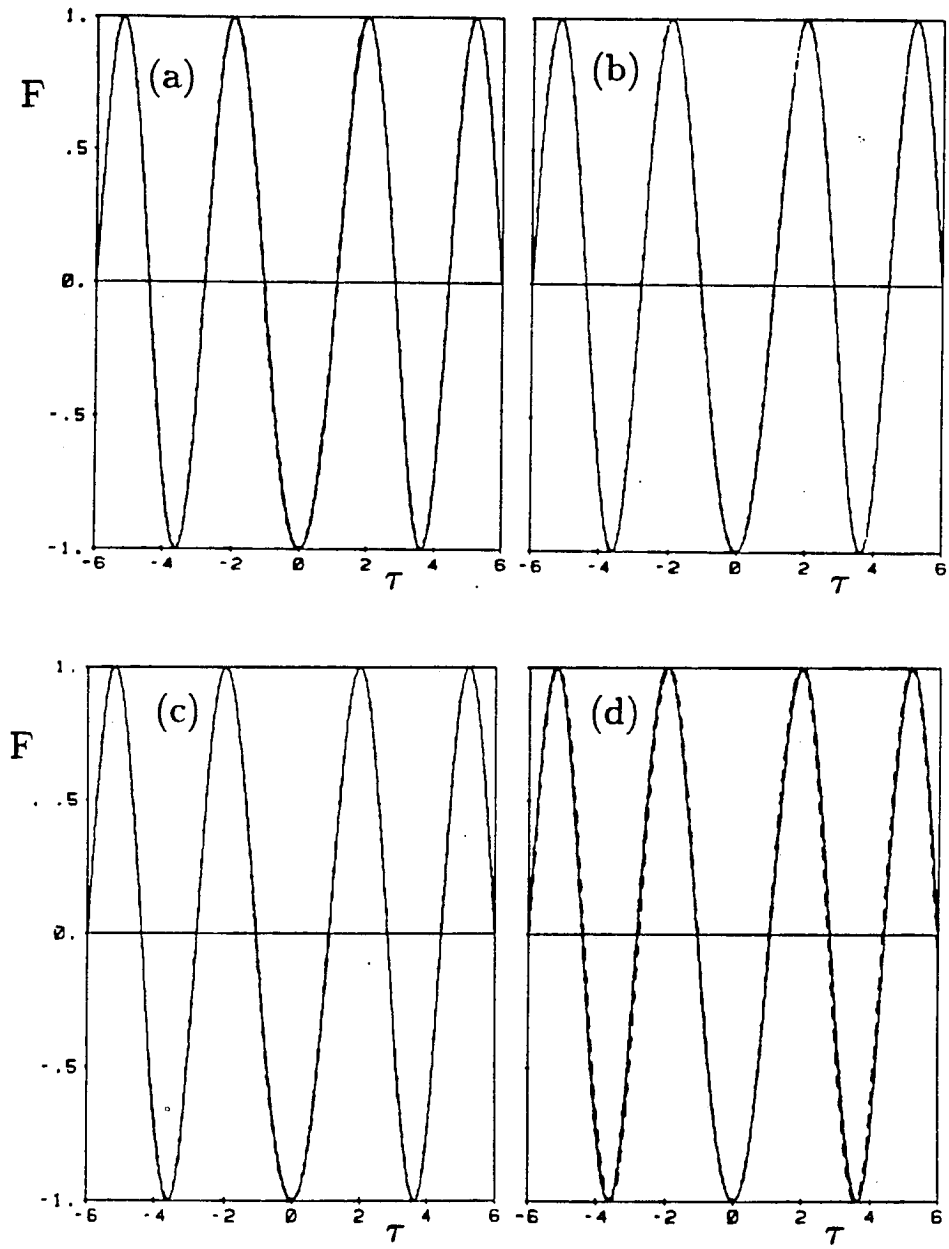

Figure 2.4: Comparative plots of the *integrand* $F(u,\tau)$ of Eq. 2.21. The solid line is calculated using $y(\tau) = y_{sx}$, the dashed line using $y(\tau) = [2\cos^{-1}(-u)/\pi]y'_{sx}$. a) $u = 0.20$, b) $u = 0.50$, c) $u = 0.70$, d) $u = 0.99$.

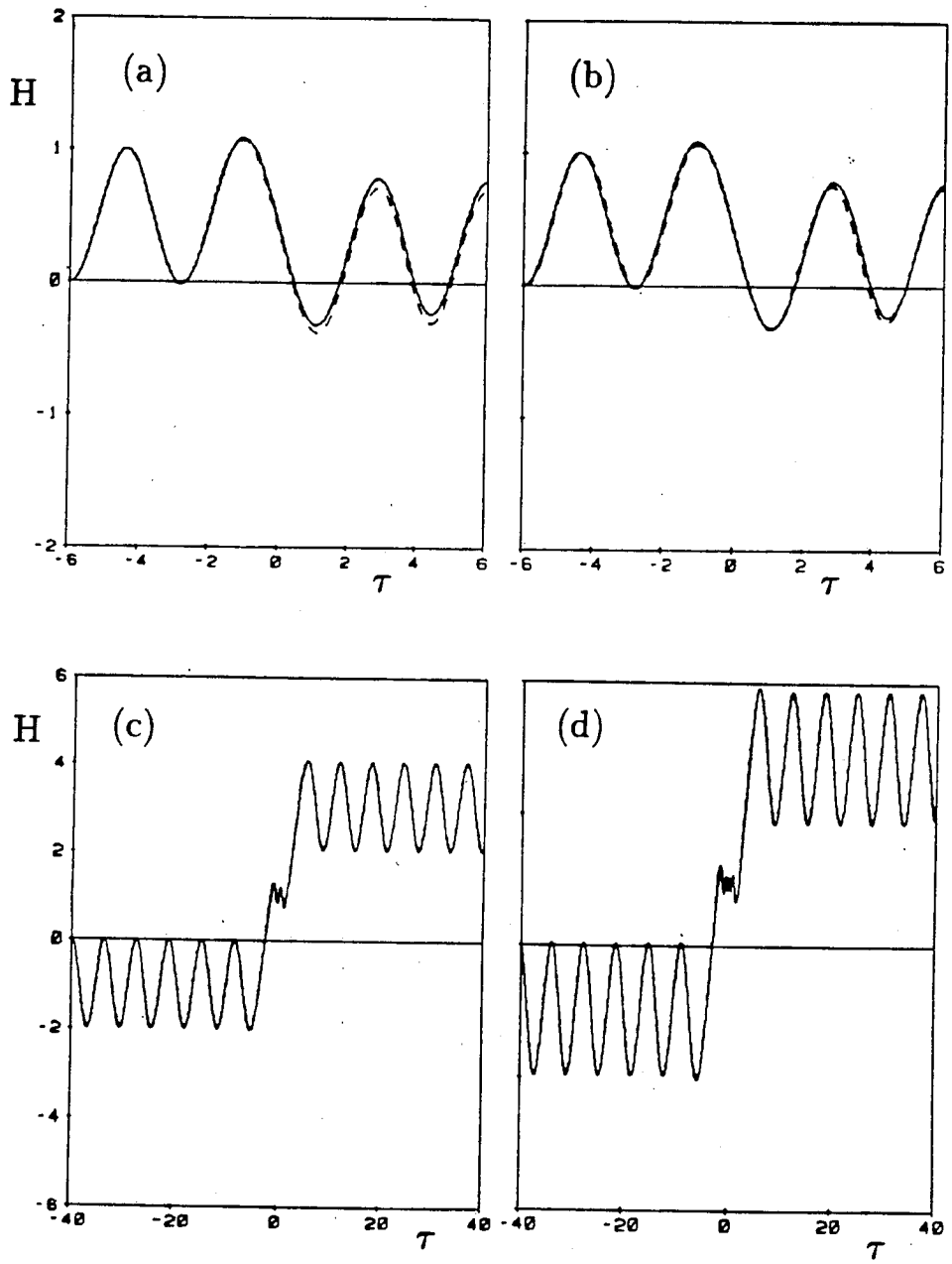

Figure 2.5: The *integral* of Eq. 2.21. The jump in the oscillations is ΔH. The solid line was evaluated with $y(\tau) = y_{sx}$, the dashed line with $y(\tau) = [2\cos^{-1}(-u)/\pi]y'_{sx}$. a) $u = 0.20$, b) $u = 0.50$, c) $u = 0.70$, d) $u = 0.99$.

where the agreement between the two expressions is closest (cf. Fig. 2.3). We can therefore substitute $[2\cos^{-1}(-u)/\pi]y'_{sx}$ instead of y_{sx} in Eq. 2.21 and define

$$s = 2q\frac{\cos^{-1}(-u)}{\pi} \tag{2.23}$$

to obtain

$$\begin{aligned}\Delta H &\approx \epsilon\Omega\sin(kn\pi+\alpha)\int_{-\infty}^{\infty}\sin\left(\frac{1}{2}sy_{sx}^{ch}-\Omega\tau+\beta\right)d\tau \\ &= \epsilon\Omega\sin(kn\pi+\alpha)\sin\beta\int_{-\infty}^{\infty}\cos\left(\frac{1}{2}sy_{sx}^{ch}-\Omega\tau\right)d\tau \\ &= \epsilon\Omega\sin(kn\pi+\alpha)A_s(\Omega)\sin\beta \end{aligned} \tag{2.24}$$

where $y_{sx}^{ch} = 2y'_{sx}$ and we have used the fact that y_{sx}^{ch} is odd in τ. $A_s(\Omega)$ is called the Melnikov-Arnold integral. For $s \in \mathcal{R}$ an approximate value for the integral is given by Chirikov, (1979):

$$A_s(\Omega) \approx \frac{4\pi}{\Gamma(s)}(2\Omega)^{s-1}e^{-\Omega\pi/2} \qquad \Omega > s. \tag{2.25}$$

We can also evaluate the integral by the method of steepest descent (see Appendix A) to obtain

$$A_s(\Omega) \approx 2\left[\frac{2\pi}{\Omega\sqrt{1-R^2}}\right]^{1/2}\cos\left[\left(\frac{\cos^{-1}R}{R}-\ln\gamma\right)\Omega-\frac{\pi}{4}\right] \qquad \Omega < s \tag{2.26}$$

where $R = \Omega/s$ and $\gamma = R/(1-\sqrt{1-R^2})$. These two approximate expressions for $A_s(\Omega)$ are compared with numerical calculations of the exact integral in Figs. 2.6 and 2.7 for different values of s.

There are two points that should be mentioned here. One is that Ω, which is the frequency of the Hamiltonian, i.e. the frequency of going around the time torus, is given by $\Omega = q_2(v_2 - v_1)/\omega_E = \omega_2^1/\omega_E$, which is the ratio of the frequency of the second wave in a frame moving with the first, over the frequency of linear oscillations around the O-point. The other point is that

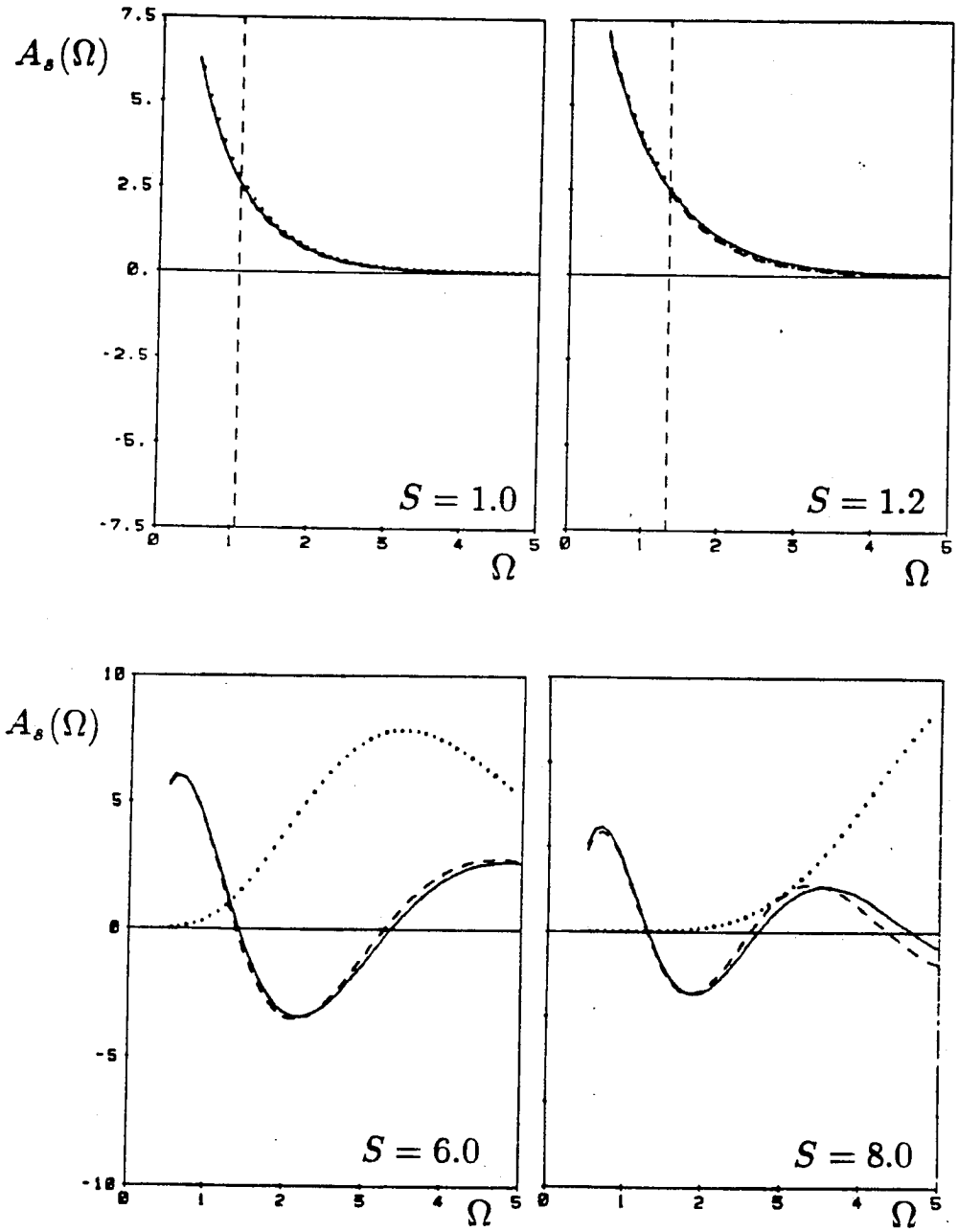

Figure 2.6: $A_s(\Omega)$ is plotted against Ω for different values of s. The solid line is the exact integral. The dashed line is the integral with $y(\tau) = (\cos^{-1}(-u)/\pi)y_{sx}^{ch}$. The dotted line is the expression in Eq. 2.25, which is only a good approximation to $A_s(\Omega)$ for $\Omega > s$. It is in excellent agreement with the exact value for $\Omega > s$ (a, b) and fails as expected for $\Omega < s$ (c, d).

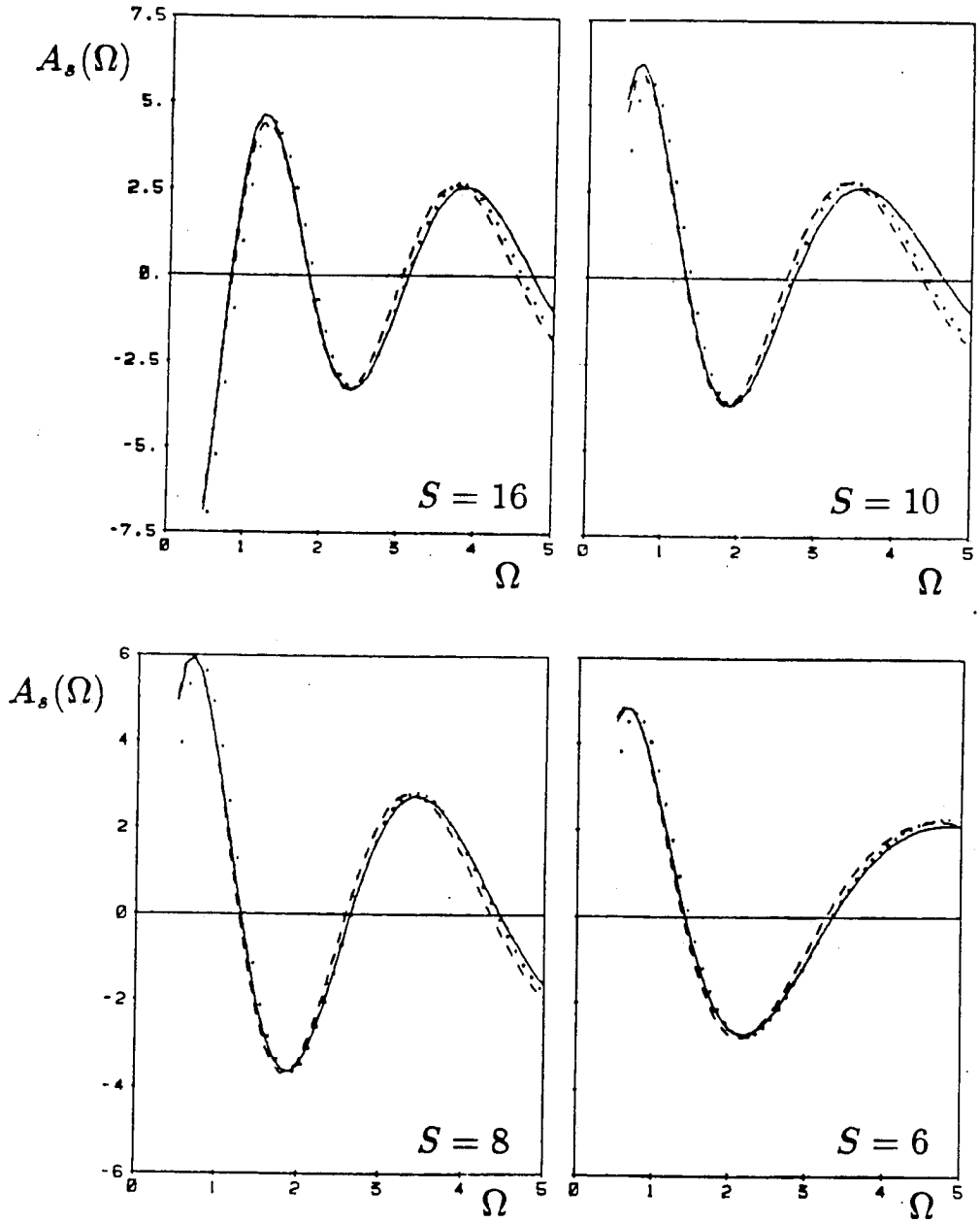

Figure 2.7: $A_s(\Omega)$ is plotted against Ω for different values of s. The solid line is the exact integral. The dashed line is the integral with $y(\tau) = (\cos^{-1}(-u)/\pi)y_{sx}^{ch}$. The dotted line is the expression in Eq. 2.26, which is only a good approximation to $A_s(\Omega)$ for $\Omega < s$.

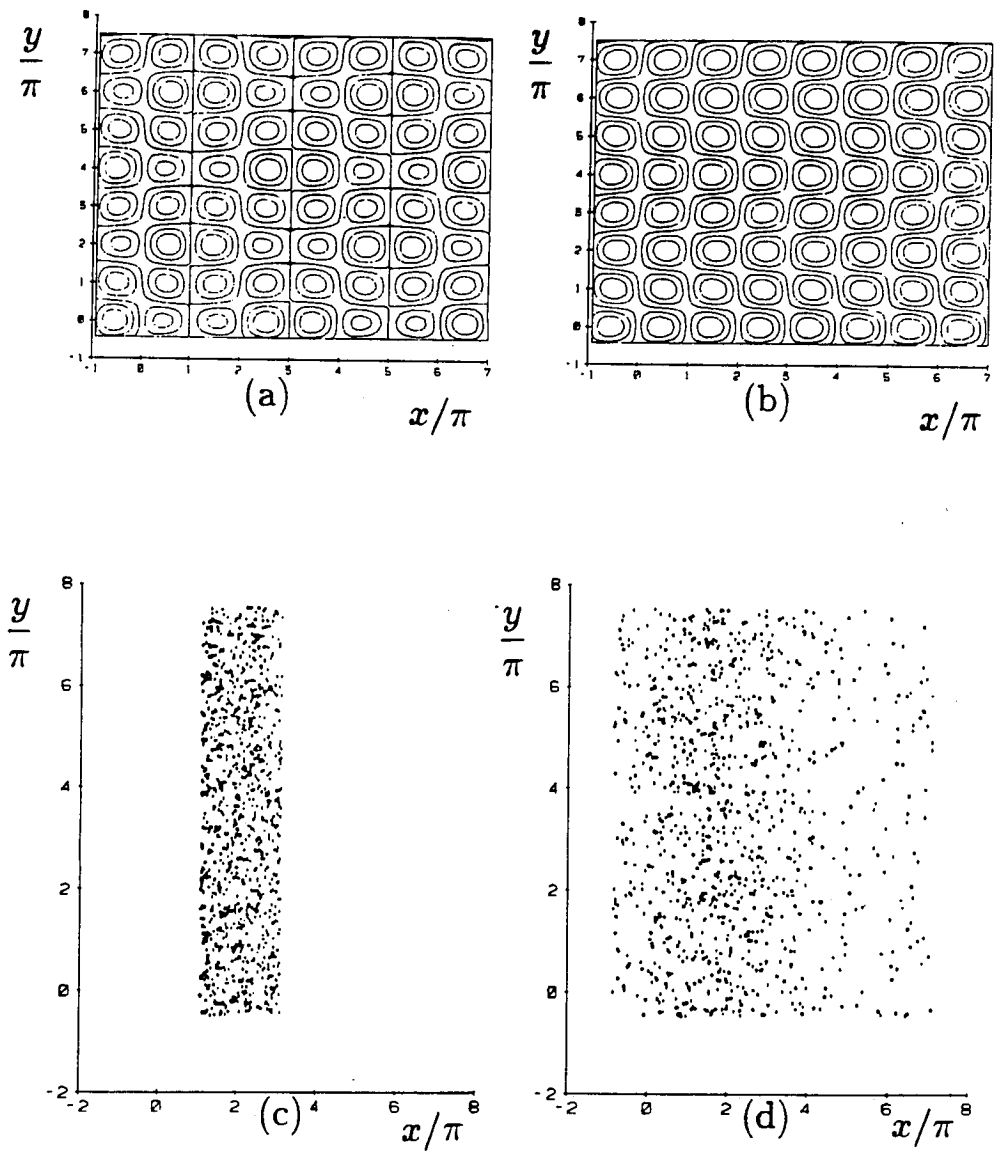

Figure 2.8: plots of the phase-space (a,b) and Poincaré surface of section plots (c, d) for $k = (m\pi - \alpha)/n\pi$ (a, c) and $k \neq (m\pi - \alpha)/n\pi$ (b, d). Notice the invariant lines formed (a) and how the particles are confined between them (c).

from Eqs. 2.19 we see that, if there is an x_0 such that $\sin x_0 = \sin(kx_0 + \alpha) = 0$, then $\dot{x} = 0 \ \ \forall\tau$, and no particles can cross the line $x = x_0$ (cf. Fig. 2.8). This condition gives

$$\left.\begin{array}{l} x_0 = n\pi \\ \\ kx_0 + \alpha = m\pi \end{array}\right\} \Longrightarrow k = \frac{m\pi - \alpha}{n\pi}. \tag{2.27}$$

If we now apply 2.27 to 2.24 we see that $\Delta H = 0 \ \ \forall\tau$. This effect is independent of the amplitude of the perturbation. So we see that, for this particular relation between k and α, the separatrix, instead of being the first to become stochastic, becomes a 'fixed line' and a barrier to particle motion. In general condition 2.27 is not satisfied in plasmas, but in simulations with only a small number of field Fourier component it could block radial motion. It is worth noting here that the existence of the condition is independent of the number of components or the type of functions in the equations of motion, the only requirement being that all components be stationary in that direction. If we had for instance

$$\dot{x} = J_0(x)f_0(y,t) + a_1 J_0(k_1 x)f_1(y,t) + a_2 J_0(k_2 x)f_2(y,t) + \cdots$$

and if x_0 is a root of the Bessel function J_0, then $\dot{x} = 0 \ \ \forall t$ and $x = x_0$ is a barrier, if $k_j = x_r/x_0$ where x_r are the roots of J_0. Clearly the more components there are, the harder it is to satisfy all conditions simultaneously, (there is one condition for each wavenumber) but as long as all components are stationary, (all argument are time-independent) there is *always* a set of conditions that, if satisfied, will block motion in that direction.

2.2.2 Standard Map

We saw in the previous section that the change in the energy of the particle as it moves from the vicinity of one X-point to the next along a tra-

jectory close to the separatrix is given by

$$\begin{aligned}
\Delta H &\approx 2\epsilon\pi \frac{(2\Omega)^s}{\Gamma(s)} e^{-\Omega\pi/2} \sin(k\pi + \alpha)\sin\beta \qquad \Omega > s \\
\Delta H &\approx 2\epsilon \left[\frac{2\Omega\pi}{\sqrt{1-R^2}}\right]^{1/2} \\
&\qquad \cos\left[\left(\frac{\cos^{-1} R}{R} - \ln\gamma\right)\Omega - \frac{\pi}{4}\right] \\
&\qquad \sin(k\pi + \alpha)\sin\beta \qquad \Omega < s
\end{aligned} \tag{2.28}$$

We can also calculate the change in phase $\Delta\beta$ in one quarter-period

$$\bar{\beta} = \beta + \frac{\pi}{4}\frac{\Omega}{\omega(\bar{H})} \tag{2.29}$$

where $\omega(H)$ is the frequency of motion around the O-point of a particle with energy H, and the bar denotes the new value (after the jump). Horton (1981) has solved the unperturbed system for $u = 0$ to obtain

$$\omega(H) = \frac{\omega_E \pi}{2\ln(4/H)}. \tag{2.30}$$

If we now put $H = W_n + W$, where W_n is a resonance of the map, given by $\bar{\beta} = \beta + 2n\pi$, then

$$\ln\left(\frac{4}{H}\right) = \ln\left[\frac{4}{W_n(1 + W/W_n)}\right] \approx \ln\left(\frac{4}{W_n}\right) - \frac{W}{W_n}$$

and we have

$$\bar{\beta} \approx \beta + \frac{\Omega}{2}\left[\ln\left(\frac{4}{W_n}\right) - \frac{W}{W_n}\right] \tag{2.31}$$

where $\Omega = qv$ is the frequency of the perturbation. Since however W_n is defined by

$$\bar{\beta} = \beta + \frac{\pi}{4}\frac{\Omega}{\omega(W_n)} = \beta + 2n\pi \tag{2.32}$$

which, using Eq. 2.30, gives

$$\ln\left(\frac{4}{W_n}\right) = \frac{4n\omega_E\pi}{\Omega} \tag{2.33}$$

we see that Eq. 2.31 becomes

$$\bar{\beta} = \beta + 2n\pi - \frac{\Omega}{2}\frac{W}{W_n}$$

which is equivalent to

$$\bar{\beta} = \beta - \frac{\Omega}{2}\frac{W}{W_n}. \tag{2.34}$$

In deriving the last two equations we use the fact that, for the normalization we chose, $\omega_E = 1$.

We can now put

$$I = -\frac{\Omega}{2}\frac{W}{W_n}$$

and we see that the change in energy and phase of the particle over a quarter-period is given by the standard map

$$\begin{aligned} \bar{I} &= I + K\sin\theta \\ \bar{\theta} &= \theta + \bar{I} \end{aligned} \tag{2.35}$$

where

$$\begin{aligned} \theta &= \beta \\ I &= -\frac{\Omega}{2}\frac{W}{W_n} \\ K &= \frac{\Omega}{2}\frac{\|\Delta H\|}{W_n} \end{aligned} \tag{2.36}$$

with $\Delta H = \|\Delta H\| \sin\beta$ given by Eq. 2.28.

We need to note here that the above expressions for the standard map are only correct for the $u = 0$ case where the particle receives four 'kicks' per cycle. For $u \neq 0$ the particle receives only two 'kicks' per period, since in the case of the open orbits the y velocity never vanishes, and in the case of the closed orbits it only vanishes at the X-points. In this case we need to make

the substitution $\Omega/2 \rightarrow \Omega$ in the above expressions to obtain the standard map description of the motion near the separatrix.

Having reduced the perturbed problem locally close to the separatrix to the standard map problem, all the theorems of the break-up of the last KAM torus at the golden mean winding number, the partial barriers of Cantori (MacKay et. al., 1984), the onset of large scale stochasticity (Escande, 1982), the scaling of the flux across the partial barriers near the critical K

$$\Delta W \sim (K - K_c)^{3.1}$$

(Mackay et. al., 1987, Meiss, 1986) and the approach of the diffusion coefficient

$$D_I(K) = \lim_{n\rightarrow\infty} \frac{(I_n - I_0)^2}{2n} \approx \frac{K^2}{4}$$

to the quasilinear value $K^2/4$ (Ichikawa et. al., 1984) can be applied to the present problem.

2.3 Stochastic Transport

We use a test particle code to measure numerically the global effective diffusion coefficient for the two-wave system. Particles are loaded at time $t = 0$ along the separatrix of the unperturbed system (cf. Fig. 2.9-a) and the running effective diffusion coefficient is given as a function of time by

$$D^*(t) = \frac{1}{n}\sum_{i=1}^{n} \frac{\langle x^2\rangle - \langle x\rangle^2}{2t} \tag{2.37}$$

while the global effective diffusion coefficient is given by

$$D^* = \lim_{t\rightarrow\infty} D^*(t). \tag{2.38}$$

Stochasticity quickly destorts the line (Fig. 2.9-b) and,depending on the parameter values, the particles are either distributed evenly within a stochastic layer

around the separatrix (Fig. 2.9-c) or, if we have global stochasticity, throughout the whole phase space (Fig. 2.9-d). In either case the value of the running diffusion coefficient quickly settles to a constant value (Fig. 2.10-a and -b) and the particle distribution function is a good fit to a gaussian (Fig. 2.10-c and -d). A statistical test (the χ^2 goodness-of-fit test) is also used to determine if the particle distribution is a good fit to a gaussian, and reject the values of $D^*(t)$ that came from a distribution with a bad fit.

We can also calculate a local background diffusion coefficient close to the separatrix, by noting that

$$\Delta H \approx \frac{\partial H_0}{\partial x}\Delta x + \frac{\partial H_0}{\partial y}\Delta y = \cos(n\pi)\Delta x + \sin(m\pi)\Delta y = \Delta x$$

since most of the contribution to the integral for ΔH comes from a short interaction time around the midpoint of the particle's trajectory (cf. Fig.2.5). We therefore see that the change in energy of a particle moving close to the separatrix is equivalent to a 'kick' in x of magnitude ΔH. We then estimate the local background diffusion coefficient to be given by

$$D = \frac{\langle(\Delta H)^2\rangle}{2\tau_c} \tag{2.39}$$

where ΔH^2 is averaged over the phase β. For the characteristic kick time τ_c we use

$$\tau_c = \frac{1}{2}T(\Delta H) = \frac{2}{\omega_E}\ln\left(\frac{4}{\Delta H}\right) \tag{2.40}$$

i.e. half the period around the O-point of a particle that is ΔH away from the separatrix, and therefore can cross the separatrix in one jump (the value of H on the separatrix is zero). The background diffusion coefficient D is enhanced by the unperturbed flow (Rosenbluth et. al., 1987) to give the global effective diffusion coefficient D^* which is given in terms of D by an asymptotic series

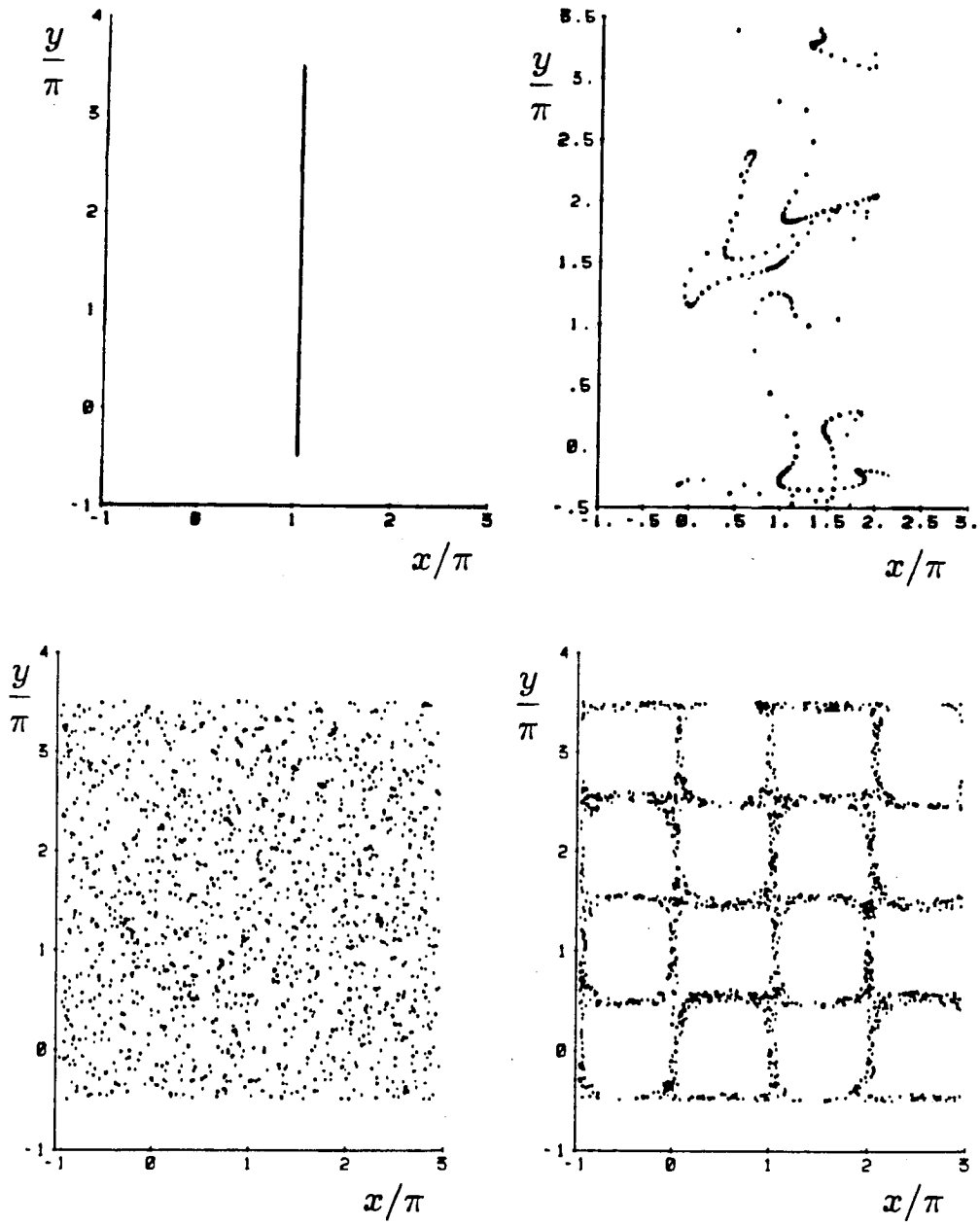

Figure 2.9: Poincaré surface of section plots for the two-wave system. a) $t = 0$ b) $t = 0.05\,\Omega^{-1}$ c) $t = 85\,\Omega^{-1}$, $\Omega/\omega_E = 12.5$ d) $t = 70\,\Omega^{-1}$, $\Omega/\omega_E = 1.6$.

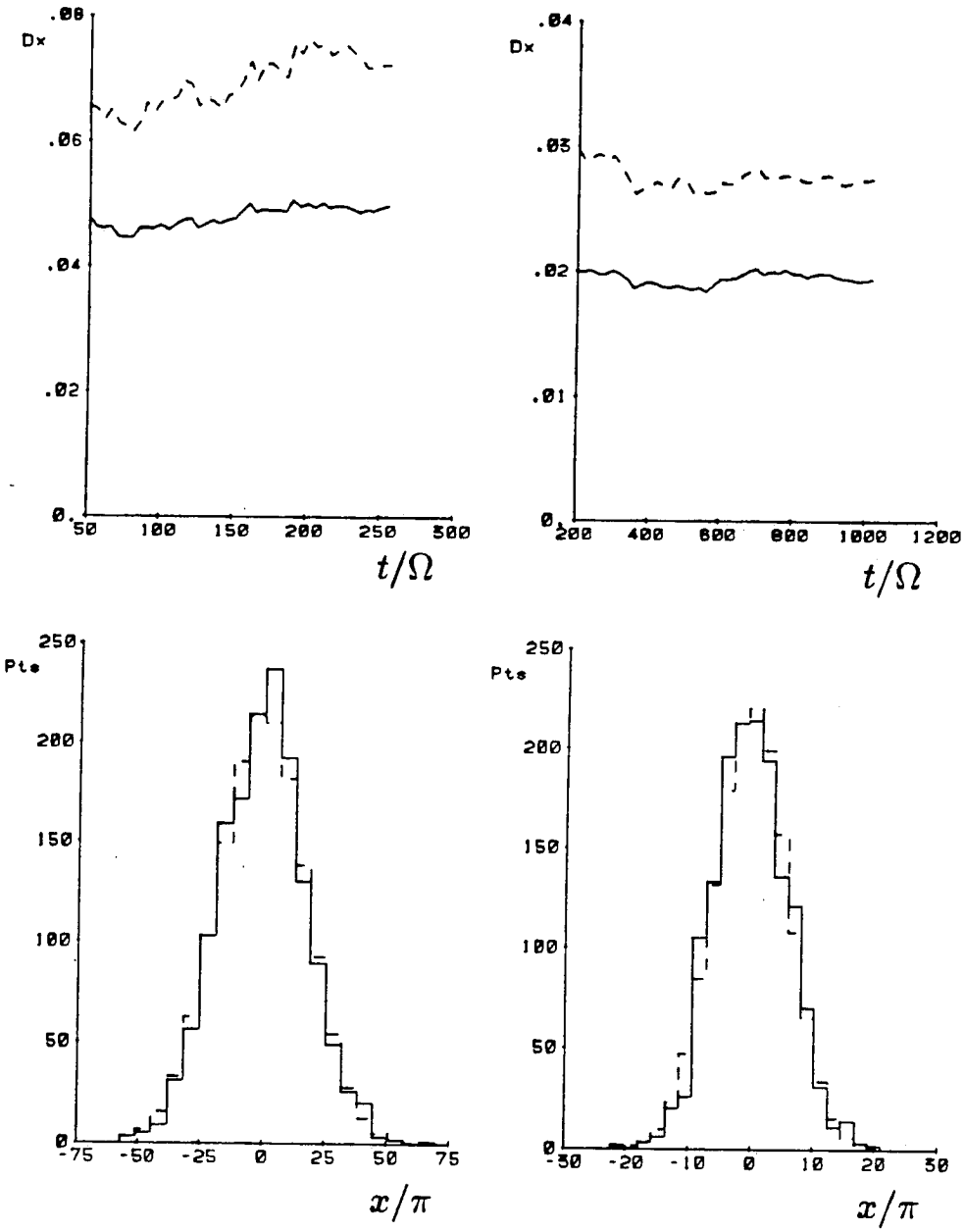

Figure 2.10: Typical plots of the running diffusion coefficient and particle distribution functions. a), c) $\Omega/\omega_E = 12.5$, b), d) $\Omega/\omega_E = 1.6$.

whose first term is

$$D^* = \frac{\sqrt{u\beta LD}}{\pi A(\beta)} = a\sqrt{D} \tag{2.41}$$

Here u is the maximum velocity of the particles in the unperturbed flow, L the size of the cell, β the aspect ratio of the cell, and $A(\beta)$ a numerical factor. For the flow we are considering the theoretical value of a is $a = 1.076$. The expansion is a good approximation to the global effective diffusion coefficient for large Peclet number ($P = uL/D \gg 1$), and for small kick lenght (see Rosenbluth et. al., 1987). We find that the theoretical value for D^* given by Eq. 2.41 agrees well with numerical simulations provided we have global stochasticity, and ΔH is small enough.

We therefore see that a purely hamiltonian system can exibit behaviour indistinguishable from a collisional system (the particle distribution functions in Fig.2.10 are good Gaussians, and we get a well defined diffusion coefficient). We also showed that the resemblance is more than phenomenological, since, at least for a certain range of parameters, we can model the effective global diffusion coefficient by small 'kicks' the particle receives as it moves close to the separatrix.

Part II

STOCHASTICITY IN COLLISIONLESS RECONNECTION

Chapter 3

COLLISIONLESS RECONNECTION AND THE GEOMAGNETIC TAIL

A general problem of plasma theory is to predict the rate of magnetic reconnection in a collisionless plasma. We consider here the simplest geometry of a reversed magnetic field due to a plasma current sheet. In its simplest form the problem is called the Harris plasma sheet. The magnetic fusion experiments of the field reversed configuration (FRC) are its simplest laboratoty realizations. The most detailed measurments however of collisionless, reactor-regime plasmas in an FRC come from the geomagnetic tail plasma sheet. Thus we have researched the collisionless reconnection regime with the idea of applying the results both to the geomagnetic tail and to the FRC.

3.1 The Magnetotail Geometry

Since Dungey (1953, 1961) posed the problem of magnetic field line reconnection in the Earth's magnetotail, a search has been on for a mechanism that would allow the release of the stored magnetic energy. A large part of that search has been directed toward the tearing mode (eg. Coppi et. al., 1966; Shindler, 1974; Galeev and Zelenyĭ, 1976). In the present work we use numerical results from a test particle code to elucidate some of the collisionless transport processes that take place in the tail and to help us derive analytical expressions

for the tearing mode growth rate.

The main features of the geomagnetic tail, which is similar to one half of a long FRC, are a horizontal (earthward–tailward) magnetic field which reverses direction within a thin layer of width a, and a small normal (northward) component (cf. Fig. 3.1). B_0 is the asymptotic value of the horizontal field and B_n the normal component. The tail can remain in this state, called the 'quiescent' state, for a long time (days or even weeks), and then, suddenly, things can begin to change rapidly. B_0 increases, B_n decreases, the reversing layer gets thinner ($a \downarrow$) and the plasma sheet temperature increases. The reversed field lines reconnect at some point downtail from the earth and a neutral line is formed. A blob of plasma, sometimes called a plasmoid, is separated from the rest of the plasma in the tail and ejected tailward (cf. Fig. 3.2). The whole process lasts 15–30 minutes, which is of the order of 200-400 Alfven times a/v_A with $v_A = B_0/(4\pi m_i n_i)^{1/2}$. Taking $a \sim R_e$, where $R_e = 6380\,km$ is the Earth's radius, we obtain $v_A \approx 1400\,km/s$.

Since the earth's magnetotail is highly collisionless, with the collisional mean free path being $\lambda_{mfp} \approx 10^9\,R_e$ (Speiser, 1987), Coulomb collisions are totally inadequate for providing the necessary dissipation for reconnection, and the reconnection time given by resistive MHD theory (Furth et. al. 1963) is several orders of magnitude too long. A collisionless Ohm's law is therefore required.

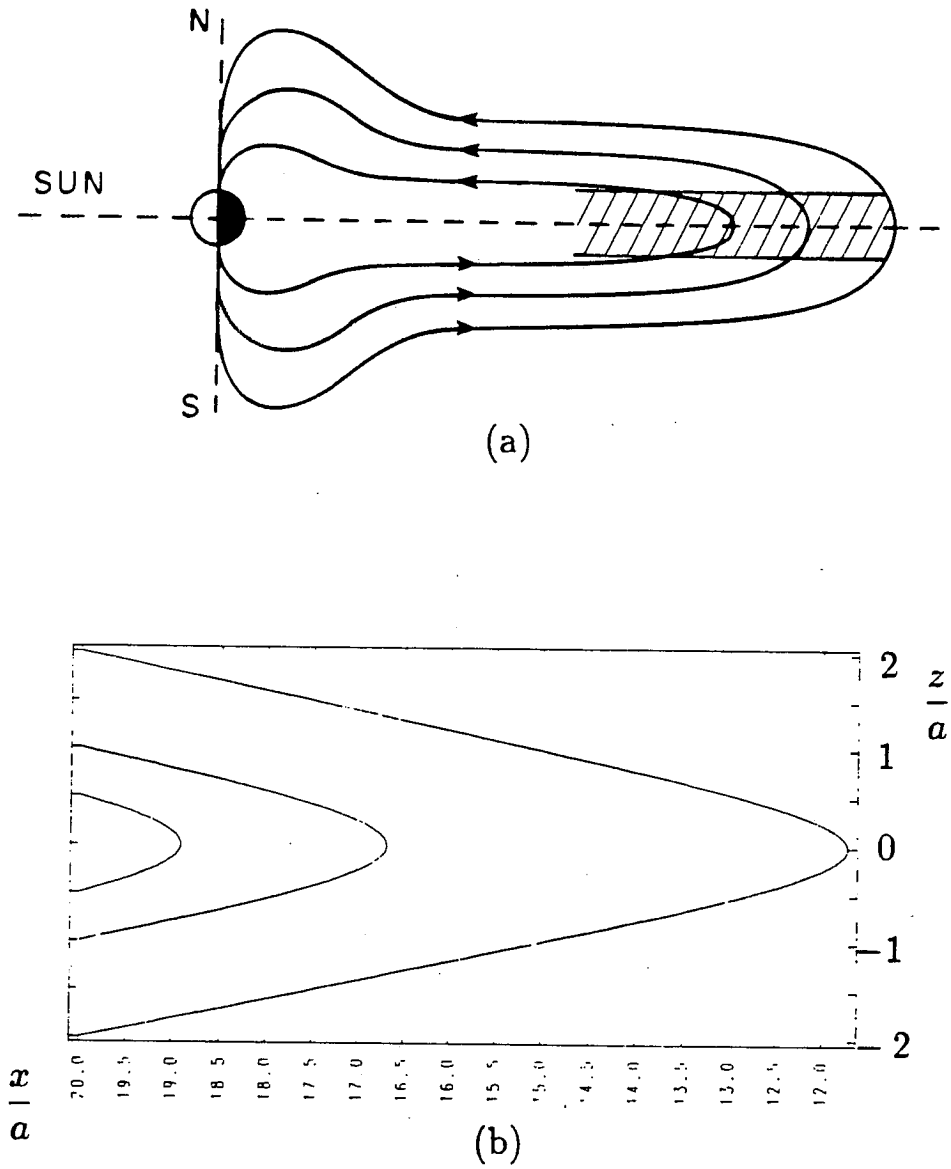

Figure 3.1: a)The geomagnetic tail in its quiescent state. The shaded region is the region of interest. It is expanded in (b).

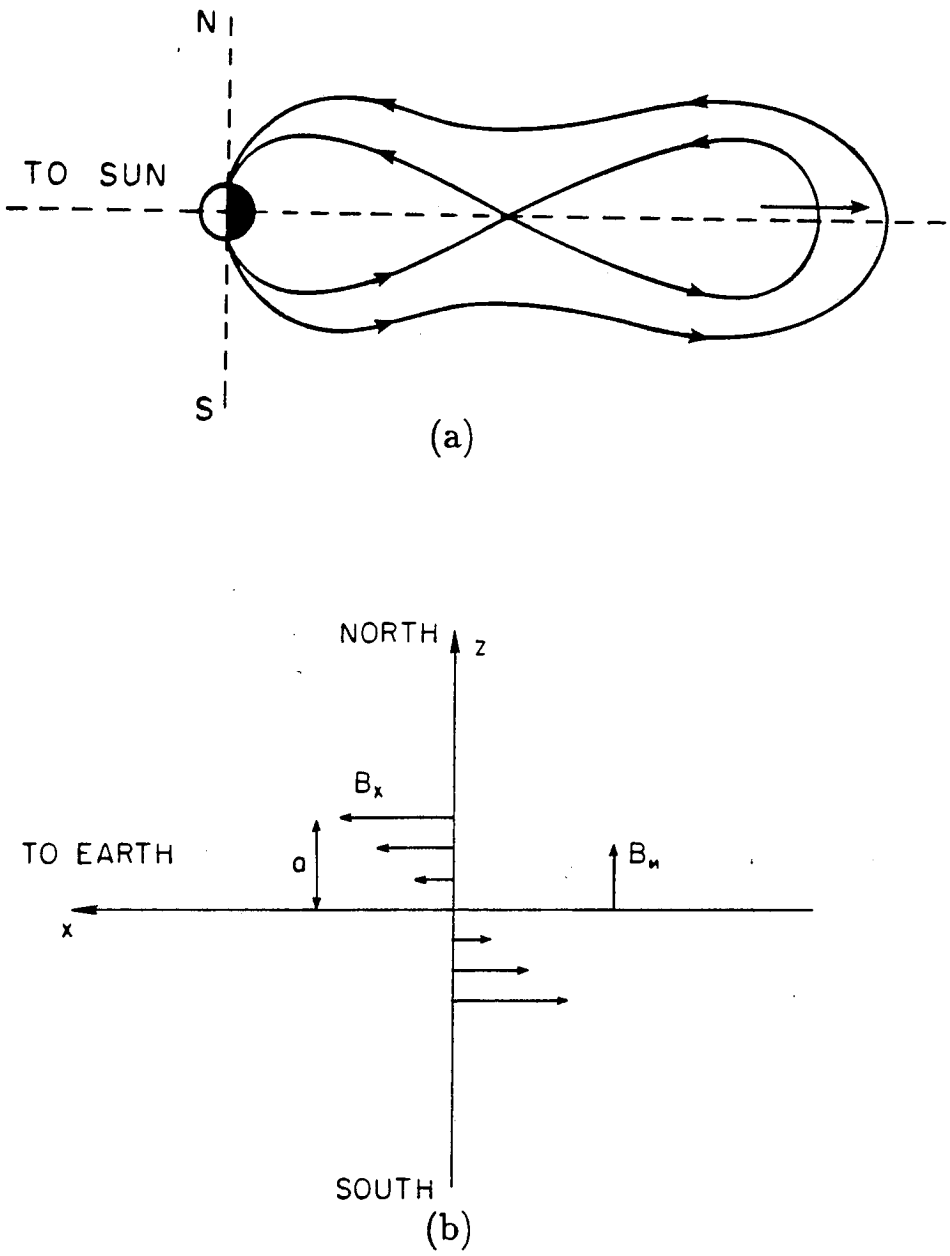

Figure 3.2: a) The geomagnetic tail during reconnection. b) The field configuration used in the model.

3.2 Ohm's Law

The reversed magnetic field with a reconnection mode of amplitude ψ_0 and wavenumber k is given by

$$\begin{aligned} B_x &= B_0 \tanh\left(\frac{z}{a}\right) \\ B_z &= B_0 b + B_0 \psi_0 k \sin(kx) e^{\gamma t} \\ E_y &= B_0 \psi_0 \frac{\gamma}{c} \cos(kx) e^{\gamma t} \end{aligned} \tag{3.1}$$

which is the model we are using in the present work. These fields can be derived from the flux function

$$\psi = B_0[a \ln(\cosh(z/a)) + \psi_0 \cos(kx) e^{\gamma t} - bx] \tag{3.2}$$

where the vector potential is $\vec{A} = -\psi(x, y, z)\hat{e}_y$ and the fields are given by $\vec{B} = \hat{y} \times \nabla\psi$ and $E_y = (1/c)\partial_t \psi$. Here ψ_0 is the amplitude of the tearing perturbation, k its wavenumber and γ the growth rate. We define $b = B_n/B_0$ to be the ratio of the normal component to the asymptotic field. In our analysis we will treat the tearing mode and the normal field as a perturbation, so we will henceforth refer to 3.1 as the full system, while the system defined by 3.1 with $b = \psi_0 = 0$,which has integrable orbits, will be referred to as the unperturbed system.

For a particle of mass m_j, charge e_j and thermal velocity v, there are two important dimensionless parameters. One is the particle gyroradius in the asymptotic field $\rho_{0j} = v/\omega_{0j}$ where $\omega_{0j} = e_j B_0/m_j c$. If we write the reversing magnetic field close to $z = 0$ as $B_x = B_0(z/a)$, and then define the half-width of the unmagnetized layer by

$$\Delta z = \rho_{(\Delta z)} = \frac{v}{\omega_{(\Delta z)}} = \frac{v}{\omega_0 \Delta z/a}$$

we find

$$\Delta z = \sqrt{av\omega_0} = \sqrt{a\rho_0} \tag{3.3}$$

for the half-width of the unmagnetised layer. The second important parameter is the number of cyclotron orbits in the vertical field during a transit across the unmagnetized layer, given by

$$\kappa = b\omega_0 \frac{\sqrt{a\rho_0}}{v} = \frac{b}{\sqrt{\epsilon}} \tag{3.4}$$

where

$$\epsilon = \sqrt{\frac{\rho_0}{a}} \tag{3.5}$$

is the small variable in the adiabatic approximation. As we will see later, the parameter κ plays a very important role in the chaotic dynamics of the system.

In the linear, collisionless regime the solution for the distribution of particles of species j can be found in principle by the orbit integral over the unperturbed trajectories

$$\delta f_j(\vec{x},\vec{v},t) = -\frac{e_j}{m_j}\int_{-\infty}^{t}\Big[v_y\frac{\partial\psi}{\partial t'}\frac{\partial f_0}{\partial \mathcal{E}} + \frac{\partial\psi}{\partial t'}\frac{\partial f_0}{\partial P_y} + \vec{v}\cdot\nabla\psi\frac{\partial f_0}{\partial P_y}\Big]\,dt' \tag{3.6}$$

where the perturbed current is given by

$$\delta j_y(x,z,t) = \sum_j e_j \int v_y\,\delta f_j\; d^3v \tag{3.7}$$

In the geomagnetic tail problem the orbits are so complex (cf. Section 4.1), that it is simply not feasible to evaluate the integrals in Eqs. 3.6 and 3.7 and then calculate the current j_y.

In the present work Eqs. 3.6 and 3.7 are evaluated numerically by statistically sampling the long time response of the initial particle distribution $f_0(\mathcal{E}, P_y)$ and are used to derive a collisionless Ohm's law. Since however, the ∇B and curvature $\vec{K}(z=0) = (\hat{b}\cdot\nabla)\hat{b} = \hat{e}_x(B_0/B_z)a$ of the field lines produce

a large equilibrium drift velocity, we must extract from j_y the part that is in phase with the electric field $E_y \sim \cos(kx)$. It is this phase-coherent part of the current that determines the reconnection growth rate. We therefore take a projection of Ampère's law and obtain

$$\int_{-\Delta z/2}^{\Delta z/2} dz \int_{-\pi/k}^{\pi/k} dx \, \cos(kx) \nabla^2 \Psi(x,z,t) = \frac{4\pi}{c} \int_{-\Delta z/2}^{\Delta z/2} dz \int_{-\pi/k}^{\pi/k} dx \, \cos(kx) j_y(x,z,t) \tag{3.8}$$

where we have taken the phase-coherent k Fourier component of the current and integrated over the current layer thickness Δz. $\Psi(x,z,t)$ is the exact flux function. Ampère's equation then reduces to

$$\left.\frac{d\Psi_k(z,t)}{dz}\right|_{-\Delta z/2}^{\Delta z/2} = \frac{4\pi}{c} \int_{-\Delta z/2}^{\Delta z/2} dz \langle j_y \cos(kx) \rangle_{(z,t)}. \tag{3.9}$$

The projection in Eq. 3.8 can also be motivated from conservation of energy, given by the Poynting theorem

$$\frac{\partial}{\partial t} \int \frac{(\nabla \psi)^2}{2} \, dx \, dy + \left(\int \frac{c E_y B_x}{4\pi} dx \right) \Bigg|_{-\Delta z/2}^{\Delta z/2} = - \int j_y E_y \, dx \, dz \tag{3.10}$$

with $E_y = B_0 \psi_0 (\gamma/c) \cos(kx)$. We see then that the height integrated moment $\int_{-\Delta z/2}^{\Delta z/2} dz \, j_y \cos(kx) = \langle j_y \cos(kx) \rangle$ controls the transfer of energy from the field to the particles which determines the reconnection growth rate.

The right hand side of 3.9 can also be evaluated by elementary principles to give

$$\int_{-\Delta z/2}^{\Delta z/2} dz \, \langle j_y \cos(kx) \rangle = \frac{Qe \langle E \cos(kx) \rangle}{m} \tau = \frac{ne^2}{m} \frac{E_{0k}}{2} (\Delta z) \tau \tag{3.11}$$

where we used $j = Qv$ with $Q = en(\Delta z)\lambda^2$, so that Q is the total charge inside a layer of width Δz, $v = a\tau = (E/m)\tau$ where τ is the decorrelation time, or the time the particle is accelerated coherently by the electric field. Finally

$$\langle E \cos(kx) \rangle = \frac{1}{2\pi} \int_{-\lambda/2}^{\lambda/2} E_{0k} \cos^2(kx) \, dx = \frac{E_{0k}}{2}.$$

Equations 3.9 and 3.11 are then solved simultaneously to give the growth rate

$$\gamma = \frac{c^2 \Delta_k'}{\omega_p^2(\Delta z)\tau} \tag{3.12}$$

where $\Delta_k' = [\Psi_k'(\Delta z/2) - \Psi_k'(-\Delta z/2)]/B_0\psi_0$ is the jump in the derivative of the flux function across the current layer (Furth et. al. 1963). Note that the growth rate depends on the current layer width Δz and the effective decorrelation time τ.

In the present work we use a test particle code to evaluate the moment $\langle j \cdot E \rangle$ and the width of the current layer Δz numerically, and then we solve Eq. 3.11 for τ. We then use the numerical values to help us derive analytical expressions for Δz and τ. In the next sections we give for reference some well known estimates of Δz and τ.

3.3 Previous Work

The tearing mode was studied in the context of resistive MHD theory by Furth et. al. (1963). The width of the current layer is given in terms of the resistivity as

$$\Delta z = \left(\frac{ac}{\omega_{pe}}\right)^{1/2} \left(\frac{\gamma \nu e}{k^2 v_A^2}\right)^{1/4} \tag{3.13}$$

where $v_A = B/(4\pi n m_i)^{1/2}$ is the Alfvén speed and the resistivity η is given by $\eta = (m_e/ne^2)\nu$ so that the decorrelation time $\tau = 1/\nu$ is

$$\tau = \frac{m_e}{ne^2\eta}. \tag{3.14}$$

Substituting Eqs. 3.13 and 3.14 into 3.12 we obtain the mode growth rate, given by

$$\gamma_{FKR} = \left(\frac{v_A}{a}\right)^{2/5} \left(\frac{c^2\nu}{\omega_{pe}^2 a^2}\right)^{3/5} (a\Delta_k')^{2/5}. \tag{3.15}$$

In the earth's magnetotail $n \approx 0.1\ cm^{-3}$, $B \approx 20\ nT$, $T_e \approx 1\ keV$, $T_i \approx 2\ keV$ and $a \approx R_e = 6380\ km$ (eg. Lyons and Williams, 1984). When substituted into Eq. 3.15 these parameters give $\gamma_{FKR}^{-1} \sim 2200\ yrs$ which is eight orders of magnitude longer than the observed substorm time. This is to be expected since the magnetotail is highly collisionless and resistive MHD theory relies on collisions to provide the dissipation necessary for the growth of the tearing mode (cf. Eq. 3.14). Furth (1962) also discussed the kinetic theory of the collisionless tearing mode. He obtained a growth rate $\gamma \sim kv\sqrt{nae^2/m_e c^2}$, where $v \gg v_{th}$ is the flow velocity, and claimed that the MHD result can be extended to the collisionless regime by substituting $\eta = \eta_c + \eta_i$ to the MHD result, where η_c is the collisional resistivity and η_i the inertial resistivity.

The first systematic attempt to derive a collisionless growth rate for the magnetotail was made by Coppi et. al. (1966) and Laval et. al.(1966). They considered a current sheet flowing in the neutral layer of a reversing field with no normal component (cf. Fig. 3.1 with $B_n = 0$; the current flows out of the page). For this one-dimensional configuration a self consistent solution of the Vlasov equation can be obtained (Harris, 1962). Since the Vlasov equation is equivalent to the Liouville theorem, any function that is only a function of the constants of motion will be a solution. Harris considered a distribution function of the form

$$f_s = \left(\frac{m_s}{2\pi T_s}\right)^{3/2} n_s \exp\left[-\left(\frac{m_s}{2T_s}\right)(\alpha_1^2 + (\alpha_2 - v_s)^2 + \alpha_3^2)\right] \tag{3.16}$$

where the α's are functions of the constants of motion only. Using this distribution function to obtain the charge and current density, and substituting those into the Poisson equation and Ampère's law, we obtain two coupled differential equations for the electrostatic potential ϕ and the vector potential $\vec{A}$.

The solution that has $\phi = 0$ gives

$$\begin{aligned} A_y &= B_0 a \ln\left(\cosh\left(\frac{z}{a}\right)\right) \\ B_x &= B_0 \tanh\left(\frac{z}{a}\right) \\ j_y &= j_0 \mathrm{sech}^2\left(\frac{z}{a}\right) \end{aligned} \tag{3.17}$$

which is the same field configuration as that given by 3.1 for $b = \psi_0 = 0$. Coppi et. al. and Laval et. al. studied the stability of the Harris sheet and found it to be unstable to the tearing mode with a growth rate of

$$\gamma_{CL} = \pi^{1/2}\left(\frac{\rho_e}{2a}\right)^{3/2}\left(\frac{v_e}{a}\right)\left(\frac{T_e + T_i}{T_e}\right) \tag{3.18}$$

which gives a growth time of ~ 4.5 days. The current layer thickness and the decorrelation time are given by

$$\Delta z = \sqrt{a\rho_e} \quad , \quad \tau = \frac{1}{kv_e}. \tag{3.19}$$

Galeev and Zelenyĭ (1976) made a similar calculation for the two-dimensional case (nonzero normal component) and found that, as was proposed by Shindler (1974) and later confirmed in a more detailed calculation by Lembège and Pellat (1982), the normal field stabilizes the mode. The mode stabilization is due to the fact that the normal magnetic field component magnetizes the electrons in the quasineutral layer (where the horizontal field vanishes) and forces an adiabatic response to the tearing perturbation. The electron Landau interaction, which provided the dissipation necessary for the growth of the tearing mode in the one-dimensional case, is inhibited and the mode is stabilized. From the energy balance point of view, the energy required to produce the adiabatic electron response to the tearing mode exeeds the free energy available in the current sheet for instability (Lembège and Pellat, 1982; Coroniti, 1980). It was therefore suggested (Shindler, 1974) that the

ions might provide the necessary dissipation to destabilize the tearing mode. Galeev and Zelenyĭ (1976) calculated the tearing mode growth rate taking into account finite Larmor radius effects, and found that the growth rate, current layer width and decorrelation time are now given by

$$\begin{aligned} \gamma_e &= 0 \\ \gamma_i &= \pi^{-1/2}\left(\frac{\rho_i}{a}\right)^{3/2}\left(\frac{v_i}{a}\right)\left(\frac{T_e+T_i}{T_i}\right)(1-k^2a^2) \\ \Delta z &= \sqrt{a\rho_i} \quad , \quad \tau = \frac{1}{kv_i}. \end{aligned} \tag{3.20}$$

which gives a growth time of approximately $40\,min$.

We see that the expressions for the growth rate, the current layer width and the decorrelation time in Eqs. 3.18, 3.19 and 3.20 are very similar. At this point however it has to be emphasized that despite the formal similarity between Eqs. 3.18 and 3.20 this is still an *ion* tearing mode. The electrons are going to be magnetized and not contribute to the growth rate even for very small values of the normal field, and even for the ion mode there is only a narrow window in B_n for which we can have $\gamma_e = 0$ and $\gamma_i > 0$ (Shindler, 1974; Galeev and Zelenyĭ, 1976; Galeev, 1979). Furthermore, Lembège and Pellat (1982) showed in a more detailed calculation, which included the effect of the particle drift in the normal field as well as the finite Larmor radius, that the adiabaticity of the electrons will even stabilize the *ion* tearing mode. It was therefore becoming obvious that a mechanism would be needed to destabilize the electrons.

3.3.1 Destabilization of the Electron Tearing Mode

Turbulent

Coroniti (1980) first calculated the effect of turbulence-induced pitch-angle

scattering on the stabilization of the electron tearing mode. He followed the suggestion of Huba et. al. (1978), who proposed that lower hybrid drift wave turbulence might scatter the electrons, effectively introducing an electron-electron collisionality. Although the effective elctron-electron collision frequency produced by the pitch angle scattering by the waves is insufficient to produce the degree of collisional resistivity required by resistive MHD theory, it could be enough to break the adiabaticity of the electrons and destabilize the electron tearing mode. Coroniti followed a similar calculation done earlier by Hagege et. al. (1973) that used whistler mode turbulence to destabilize drift waves in the magnetosphere, and found that pitch angle scattering does indeed destabilize the electrons. The growth rate is proportional to the velocity-space diffusion D_0 introduced by the turbulence, and is given by

$$\gamma = \frac{3}{4\sqrt{\pi}\beta_e}\left(\frac{b}{ka}\right)^2 D_0 \tag{3.21}$$

Similar calculations have been done by many authors for different types of turbulence (eg. Drake and Lee, 1977; Esarey and Molvig 1987). Lower hybrid drift turbulence, ion accoustic turbulence and broadband electrostatic noise have all been invoked to provide the stochastic driving necessary to break the adiabaticity and destabilize the electrons. Esaray and Molvig (1987) in particular show that *spatial* diffusion (as opposed to velocity-space diffusion that results from pitch angle scattering) can also destabilize the electrons.

Stochastic

We therefore see that the main point of any mechanism that can destabilize the electrons is the existence of a stochastic driving force that would break the electron adiabaticity, and the physical mechanism that provides that driving is secondary. That conclusion, together with the fact that turbulence is

indeed observed in the magnetotail but either in the wrong place (lower hybrid drift wave turbulence in the Plasma Sheet Boundary Layer) or with the wrong magnitude (small amplitude broadband electrostatic noise), prompted our investigations and independetly the work of Büchner and Zelenyĭ (1986, 1987), who proposed that the intrinsic stochasticity of the particle orbits in the magnetotail could be sufficient to destabilize the electrons. Single particle motion in the magnetotail fields can indeed be stochastic.In the simpler but related geometry of elliptic magnetic flux surfaces given by

$$\psi = \psi_0 \left[\left(\frac{z}{a} \right)^2 + \left(\frac{\epsilon x}{a} \right)^2 \right]$$

where ϵ parametrises the ellipticity of the flux surfaces, Kim and Cary, (1983) found that for

$$\epsilon^{3/2} < \sqrt{2mE}/p_y < 1$$

where E is the particle energy, most of the particle trajectories are stochastic. Also numerical and analytical work by Chen and Palmadesso, (1986) and Büchner and Zelenyĭ, (1986) on the same magnetic field geometry we are considering here (Eqs. 3.1) shows that some particle orbits are stochastic. But in order to explore that line of investigation we have to backtrack a little and look at single-particle orbits.

Chapter 4

PARTICLE ORBITS

4.1 The Unperturbed System

The particle orbits for the unperturbed system (Eqs. 3.1 with $b = \psi_0 = 0$) have been analytically obtained by Speiser (1965). The theory of the stochasticity of the orbits is also treated by Kim and Cary (1983), Chen and Palmadesso (1986) and Büchner and Zelenyi (1986, 1987) for $\psi_0 = 0$. We will give here for completeness a brief review of particle motion in the unperturbed system before we study the effect of chaotic orbits on the effective conductivity.

The equations of motion for a single particle of charge q in the fields described by the full system of Eqs. 3.1 are determined by the Lorenz force and are given by

$$\begin{aligned}
\dot{x} &= v_x \qquad \dot{y} = v_y \qquad \dot{z} = v_z \\
\dot{v}_x &= \omega_0 b v_y + \omega_0 \psi_0 v_y k \sin(kx) e^{\gamma t} \\
\dot{v}_y &= -\omega_0 b v_x + \omega_0 v_z \tanh\left(\frac{z}{a}\right) + \omega_0 \psi_0 \gamma \cos(kx) e^{\gamma t} - \\
&\quad -\omega_0 \psi_0 v_x k \sin(kx) e^{\gamma t} \\
\dot{v}_z &= -\omega_0 v_y \tanh\left(\frac{z}{a}\right)
\end{aligned} \tag{4.1}$$

where $\omega_0 = qB_0/mc$ is the particle gyrofrequency in the asymptotic field. After normalizing time to the ion gyroperiod $T_0 = 2\pi/\omega_0$, length to the perturbation

wavelength $\lambda = 2\pi/k$ and magnetic induction to B_0, we find that the system given by Eqs. 4.1 has five parameters. The amplitude of the tearing mode ψ_0, the magnitude of the normal field component b, the aspect ratio of the tearing mode ka, its growth rate γ and the total particle energy E.

The hamiltonian of the system is given by

$$H = \frac{p_x^2}{2m} + \frac{p_z^2}{2m} + \frac{1}{2m}\left(P_y + \frac{e}{c}\psi\right)^2$$

with ψ given by Eq. 3.2. For small z we can approximate $\tanh(z/a)$ by z/a; if we also have $\psi_0,\ b = 0$, (unperturbed system) then the particle dynamics can be described using the hamiltonian

$$H = \frac{p_x^2}{2m} + \frac{p_z^2}{2m} + \frac{1}{2m}\left(P_y + \frac{eB_0}{2ac}z^2\right)^2$$

The value of H is the total energy $\mathcal{E}$. It is trivial to show that the above hamiltonian gives the same equations of motion as Eqs. 4.1 for $\psi_0 = b = 0$ and $\tanh(z/a) \to z/a$. Since H has no explicit dependence on y, we can redefine the hamiltonian by

$$H_0 = H - \frac{P_y^2}{2m} = \frac{p_x^2}{2m} + \frac{p_z^2}{2m} + V(z)$$

where (4.2)

$$V(z) = \frac{\omega_0}{2a}P_y z^2 + \frac{m\omega_0^2}{8a^2}z^4$$

The hamiltonian has no explicit dependence on x either, so we could have also subtracted $p_x^2/2m$, but we will not do so in anticipation of the x-dependent perturbation we will add later. The canonical momentum $P_y = mv_y - eB_0z^2/2ac$ is a constant of the motion. It defines the magnetic flux surface the particle follows for $m/e \to 0$. P_y/m is the y-velocity of the particle as it crosses the $z = 0$ plane. The value of H_0 is the reduced energy $\mathcal{E}' = \mathcal{E} - P_y^2/2m$.

$\mathcal{E}'$ is therefore the energy relative to the y-component of the kinetic energy $mv_y^2/2$ at the reversal layer. For $\mathcal{E}' = 0$ the particle has only v_y kinetic energy as it crosses the reversal layer ($v_x = v_z = 0$), and its maximum z-excursion is

$$z_{max}^2 = (2m\mathcal{E})^{1/2}\frac{2ac}{eB_0}$$

where $2m\mathcal{E} = (mv_y - eB_0z^2/2ac)^2$ since $\mathcal{E}' = 0$.

The orbits described by Eqs. 4.2 fall into four categories according to the shape of the potential $V(z|P_y)$ and the value of the relative energy $\mathcal{E}' = \mathcal{E} - P_y^2/2m$.

a) $P_y > 0$ The potential $V(z)$ is a parabolic-like well (Fig. 4.1-a) and the particles are streaming in the $+y$-direction, (from dawn to dusk, Fig. 4.2-a). In a $z - p_z$ phase diagram the system traces ellipses around the origin (Fig. 4.3-a).

b) $P_y < 0$, $\mathcal{E}' < 0$ The potential is a double well with the relative energy below the local maximum (Fig. 4.1-b) and the particles are grad-B drifting in the $-y$-direction (Fig. 4.2-b). In phase space the system goes around one of the O-points (Fig. 4.3-b). These are located at

$$\begin{aligned} z = z_0 &= \pm\sqrt{-2P_y a/m\omega_0} \\ p_z &= 0 \end{aligned}$$

and the linear frequency of oscillation around them is

$$\omega_{0b} = \sqrt{-2\omega_0 P_y/ma} = \omega_0\frac{z_0}{a}$$

which is the local cyclotron frequency at the O-point expressed in units of $\omega_0 = eB_0/mc$. The origin is now an X-point, and the linear rate of divergence along the unstable manifold is $\lambda = \sqrt{-\omega_0 P_y/ma}$.

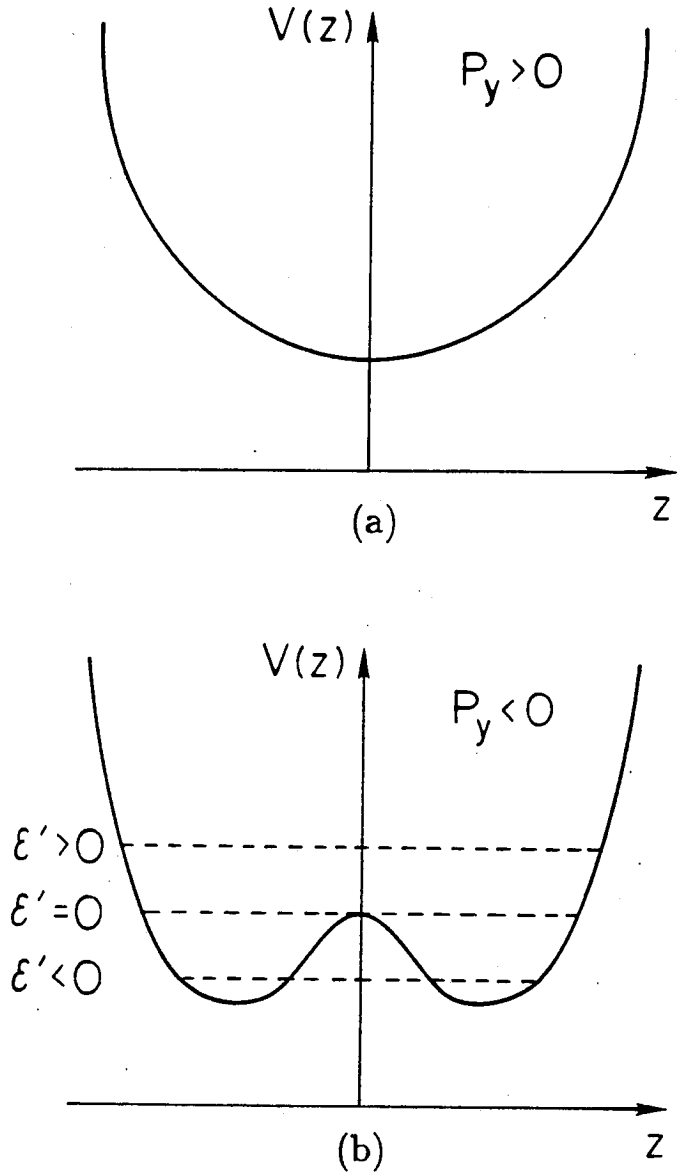

Figure 4.1: The potential $V(z|P_y)$. **a)** $P_y > 0$, **b)** $P_y < 0$.

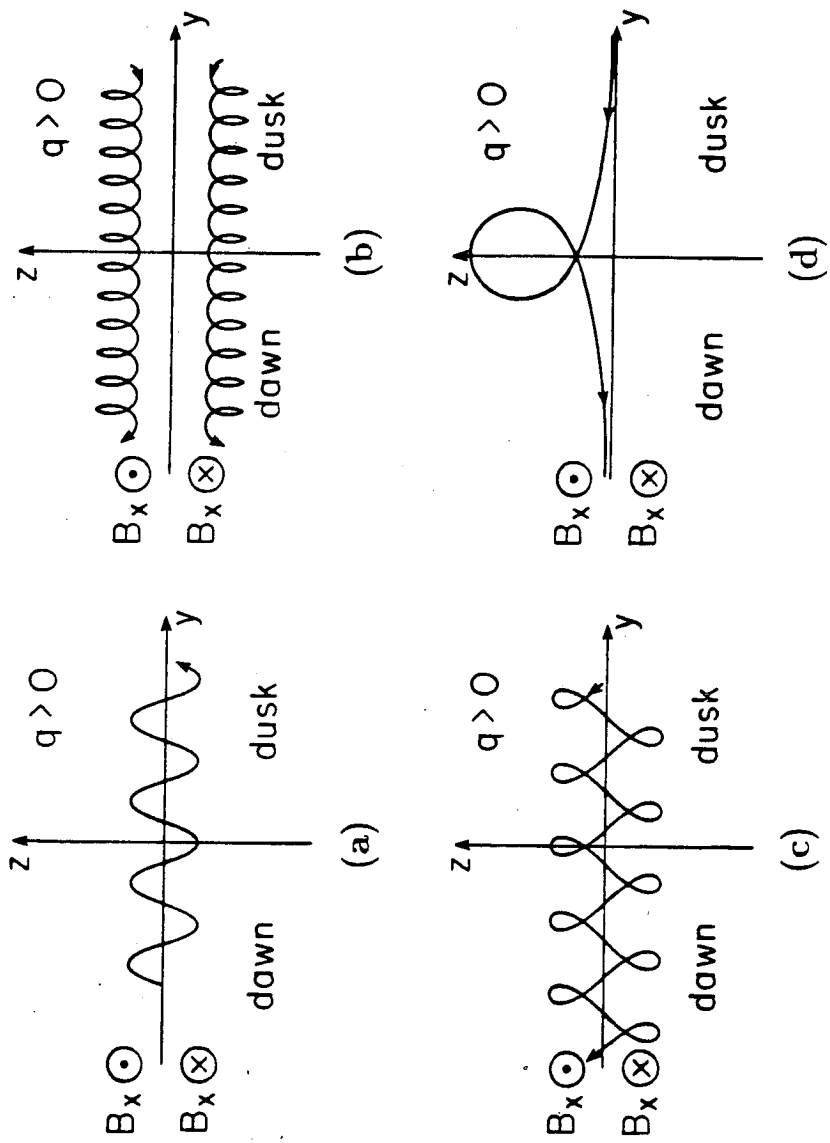

Figure 4.2: Particle trajectories in configuration space for a positively charged particle moving in the potential $V(z|P_y)$. **a)** $P_y > 0$, **b)** $P_y < 0$, $\mathcal{E}' > 0$, **c)** $P_y < 0$, $\mathcal{E}' < 0$, **d)** $P_y < 0$, $\mathcal{E}' = 0$.

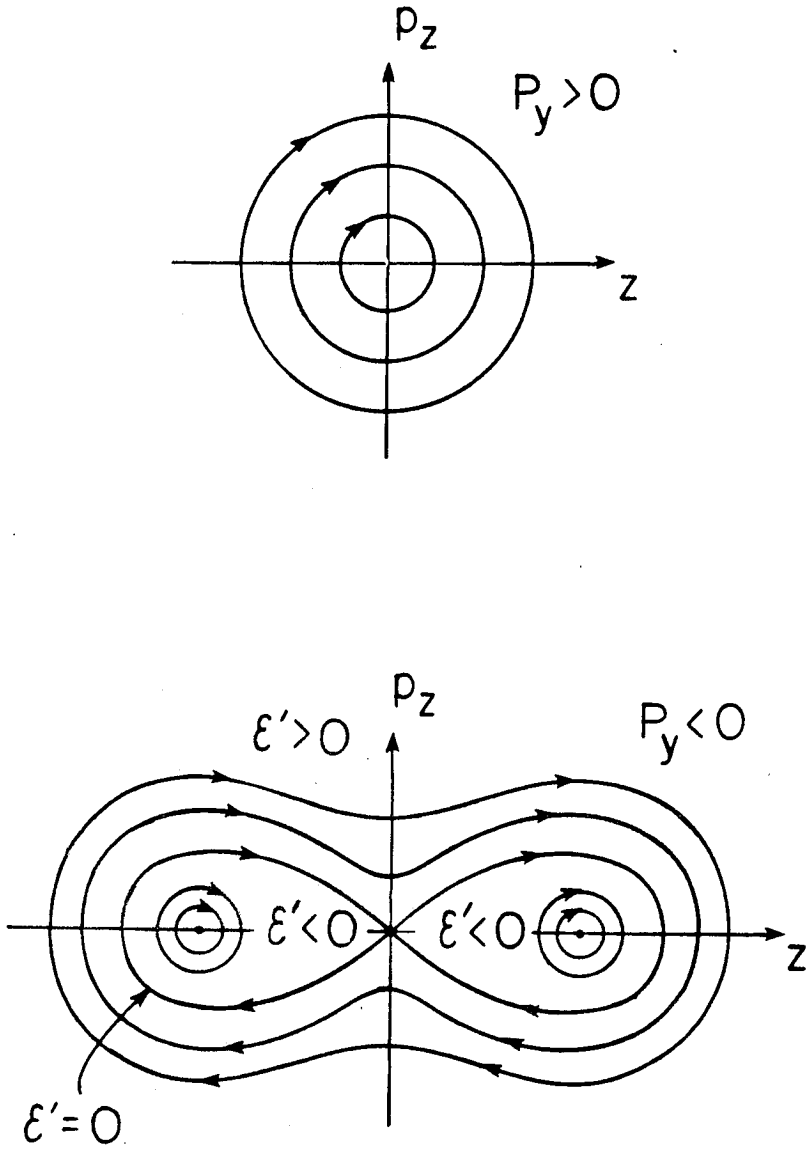

Figure 4.3: Particle trajectories in phase-space for a positively charged particle moving in the potential $V(z|P_y)$.

c) $P_y < 0$, $\mathcal{E}' > 0$ The potential is the same double well as in (b) above, but the relative energy places the system above the local maximum (Fig. 4.1-b). The particle trajectories are 'figure-eights' (Fig. 4.2-c), and in phase space the system goes around both O-points (Fig. 4.3-b). There are large-orbit particles that repeatedly cross the neutral layer.

d) $P_y < 0$, $\mathcal{E}' = 0$ This is the separatrix orbit. The relative energy places the system exactly at the local maximum (Fig. 4.1-b), and the particle makes only one loop in configuration space (Fig. 4.2-d) taking an infinite amount of time to complete a cycle along the homoclinic orbit in phase space (Fig. 4.3-b).

4.2 Adding the Normal Component; Chaos

The equations for the particle trajectories described in Sec. 4.1 above are given in Appendix B. In this section we will add the normal field component and study its effect on the particle orbits. When we put $0 < b \ll 1$, $\psi_0 = 0$ in Eq. 3.1, we get

$$\begin{aligned} B_x &= \tanh\left(\frac{z}{a}\right) \\ B_z &= B_0 b. \end{aligned}$$

The equations of motion are

$$\begin{aligned} \dot{x} &= v_x \qquad \dot{y} = v_y \qquad \dot{z} = v_z \\ \dot{v}_x &= \omega_0 b v_y \\ \dot{v}_y &= -\omega_0 b v_x + \omega_0 v_z \tanh\left(\frac{z}{a}\right) \\ \dot{v}_z &= -\omega_0 v_y \tanh\left(\frac{z}{a}\right) \end{aligned}$$

and the hamiltonian becomes (for $z \ll a$)

$$\begin{aligned} H' &= H - \frac{P_y^2}{2m} \\ &= \frac{p_x^2}{2m} + \frac{p_z^2}{2m} + \frac{m\omega_0^2}{8a^2}z^4 + \frac{m\omega_0^2}{2}b^2x^2 - \frac{m\omega_0^2}{2a}bxz^2 + \frac{P_y\omega_0}{2a}z^2 - P_y\omega_0 bx. \end{aligned}$$

In Fig. 4.4 we show a perspective view of the magnetic field lines and a typical trajectory for a particle governed by the above equations. In the case shown $b = 0.01$. The particle is injected at $1b$, follows the magnetic field lines to the quasineutral layer, executes one half turn around the normal field component while at the same time oscillating across the neutral layer, and is finally ejected into the strong field region where it follows the field lines to its mirroring point. As we shall see in Sec. 4.3.1, if $\kappa = b\sqrt{a/\rho_0} < 1$ and the particle crosses the reversal layer more than once before being reinjected into the strong field region, the time the particle spends in the neutral layer is approximately equal to half a gyroperiod around the normal field component $\pi/b\omega_0$.

If we rescale our units so that $t' = t\omega_0\sqrt{\rho_0/a}$, $x' = x/\sqrt{a\rho_0}$ and $z' = z/\sqrt{a\rho_0}$, and redefine the origin in x' by $x'' = x' - (P_y/mv\kappa)$, we obtain

$$H = \frac{1}{2}(\dot{x}^2 + \dot{z}^2) + \frac{1}{2}\left(\frac{1}{2}z^2 + \kappa x\right)^2 \tag{4.3}$$

where we have dropped the primes in the new variables. The parameter

$$\kappa = b\left(\frac{a}{\rho_0}\right)^{1/2}, \tag{4.4}$$

where $\rho_0 = v/\omega_0$ is the Larmor radius in the asymptotic field, controls the stochasticity of the orbits (Büchner and Zelenyĭ, 1986). For $\kappa \gg 1$ the magnetic moment μ is a good adiabatic invariant, and particle motion is regular

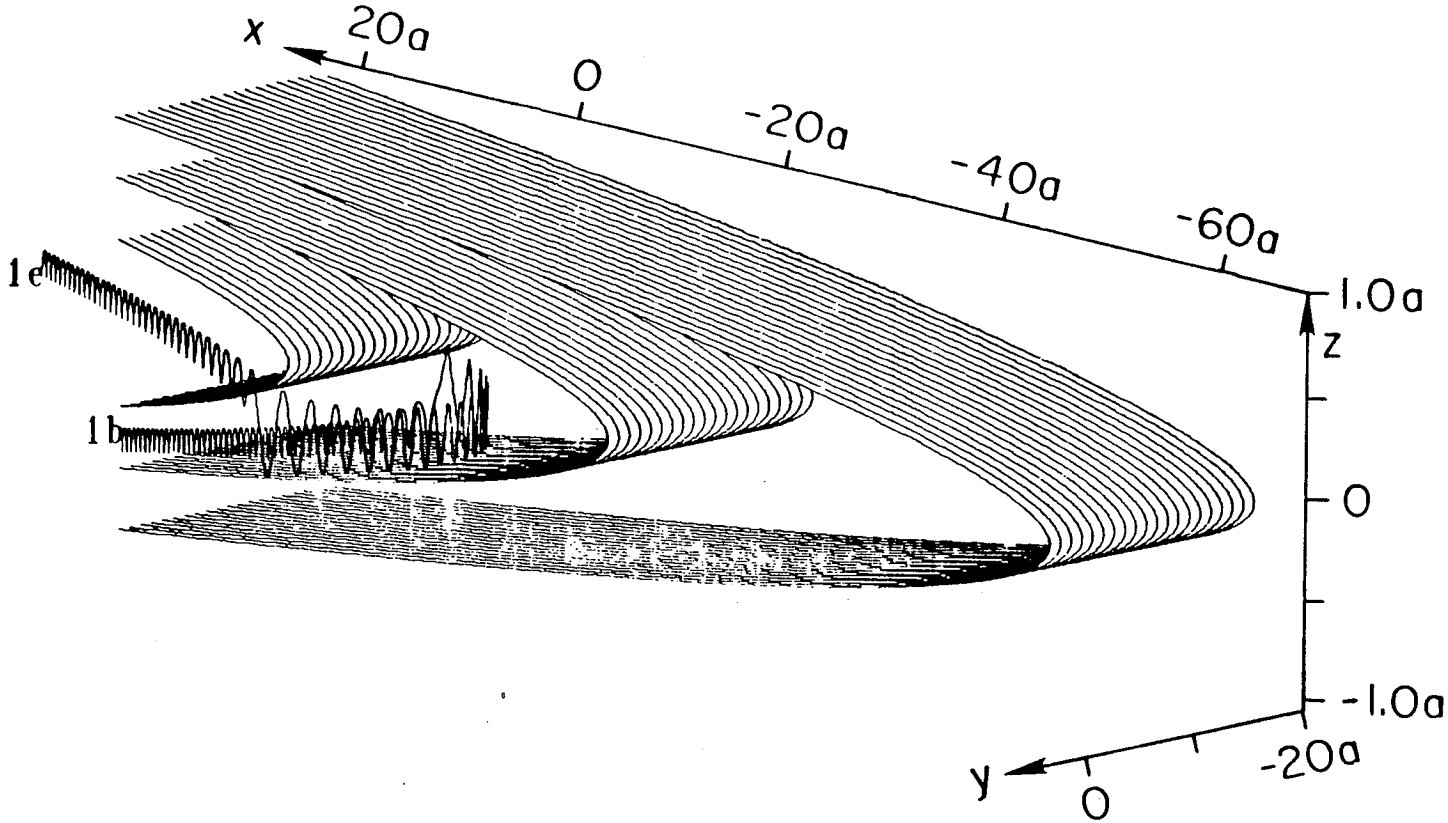

Figure 4.4: Typical particle trajectory. $\psi_0 = 0$, $\kappa < 1$. The particle crosses the reversal layer several times before being reinjected into the strong field region.

everywhere. For $\kappa \ll 1$ an adiabatic invariant that is good for most of phase space can still be found (Sonnerup, 1971). It is given by the action integral

$$J_n = \frac{1}{2\pi} \oint p_z \, dz \tag{4.5}$$

for the noncrossing orbits (cf. Fig. 4.2-b) and by

$$J_c = \frac{1}{\pi} \oint p_z \, dz \tag{4.6}$$

for the crossing orbits (cf. Fig. 4.2-c), so that on approaching the separatrix

$$J_c = 2J_n. \tag{4.7}$$

The tori defined by Eqs. 4.5 and 4.6 are shown in Fig. 4.5-a. The separatrix orbit after the addition of the perturbation is shown in Fig. 4.5-b. The stable and unstable manifolds of the hyperbolic fixed point, W_s and W_u respectively, cross an infinite number of times at the homoclinic points. The area of phase space enclosed between the two manifolds between any two homoclinic points (darkened area in the figure) is constant and is a measure of the probability a particle has of moving from an orbit inside the separatrix to one outside the separatrix (MacKay et. al., 1987).

The invariants J_n and J_c are good on either side of the separatrix, so the motion is regular everywhere except for a thin layer around the separatrix (cf. Fig. 4.5). The width of that layer can be estimated (eg. Chirikov, 1979) to be

$$\delta J = 4\pi J \left(\frac{\Omega}{\kappa}\right) e^{-(\pi\Omega/2\kappa)} \tag{4.8}$$

where Ω is the frequency of the fast z-oscillation at the time the particle crosses the $z = 0$ plane. Since the width of the stochastic layer falls off exponentially with Ω/κ, the values of the two adiabatic invariants J_n and J_c can still be matched before and after separatrix crossing as long as $\kappa \ll 1$.

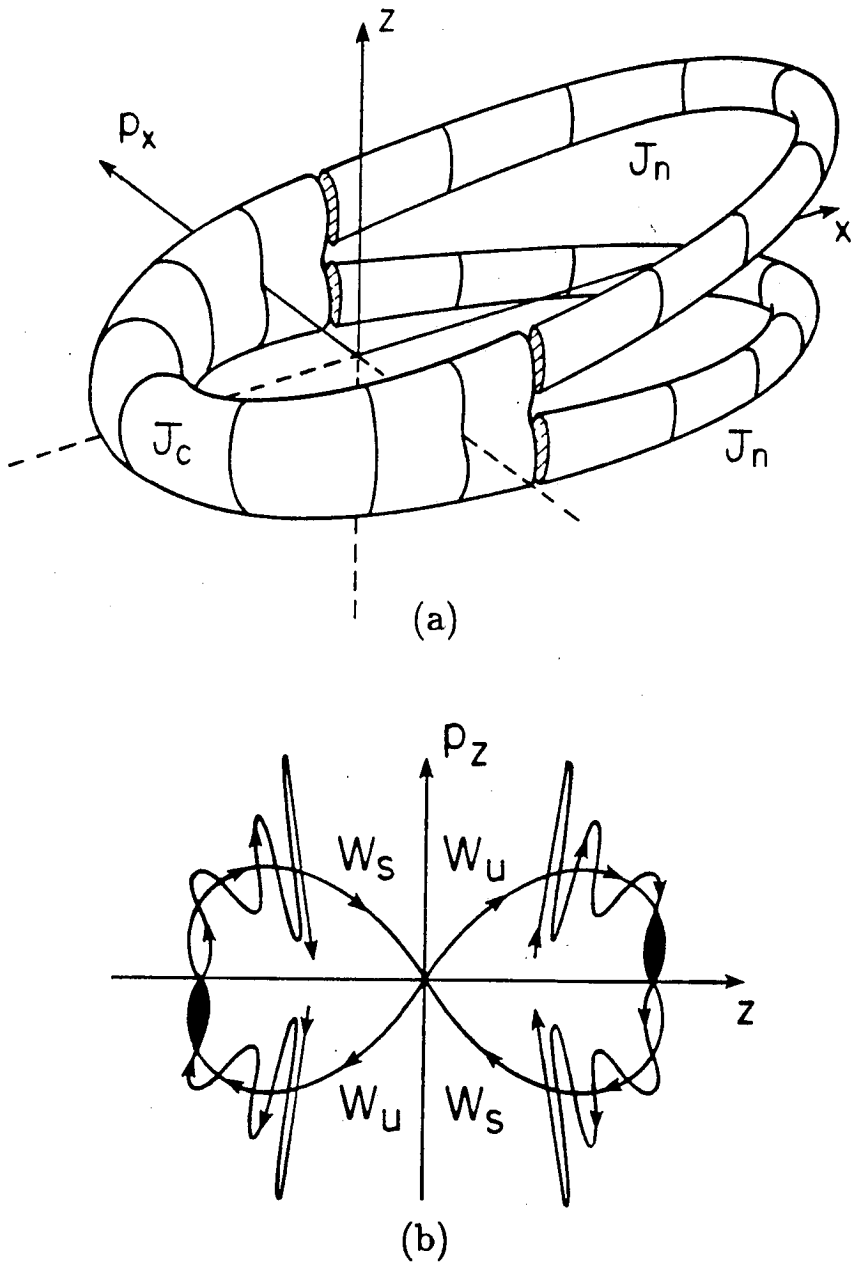

Figure 4.5: **a)** Invariant tori for J_c, J_n. Part c is the crossing part, part n the noncrossing part. The thin slice of torus that is missing represents the stochastic layer. **b)** The separatrix orbit for the perturbed system.

As κ increases the width of the stochastic layer also increases, until it occupies all of the crossing part of the torus, so that J_c is not a good adiabatic invariant anymore. For large x however, J_n transforms to the magnetic moment μ and is still a good invariant, although the value of μ changes as the particle goes through the crossing part of the torus (see next section).

This picture is typical of systems like the one described by Eq. 4.3 and reminiscent of the behavior of the system studied in Part I. The hamiltonian describes two coupled oscillators, one linear (x–p_x) and one nonlinear (z–p_z). The linearized frequency of the nonlinear oscillations, which is directly related to Ω, is of order 1 while the frequency of the linear oscillations is κ. So for $\kappa \ll 1$ or $\kappa \gg 1$ the motion can be described in terms of a fast oscillation superimposed on a slow one. As soon as the two frequencies become comparable however ($\kappa \sim 1$), an adiabatic approach is not possible anymore; the system becomes chaotic.

4.3 The Tearing Mode

We will now add the tearing mode to the fields and recover the full system 3.1. For $\psi_0 \ll b$ the tearing mode will only introduce a ripple on the normal field (cf. Fig. 4.6-a). As time increases we will eventually have $\psi_0 k e^{\gamma t} = b$ and a neutral line will appear (cf. Fig. 4.6-b). The time at which this happens for any particular value of ψ_0 can be obtained by putting $B_z = 0$ in Eq. 3.1, and is given by

$$t_c = \frac{1}{\gamma} \ln \left(\frac{b}{k\psi_0} \right). \tag{4.9}$$

When it first appears, the neutral line is located at $x = 3\lambda/4$, where $x = 0$ is the maximum positive E_y. For $t > t_c$ there are two neutral lines, one moving

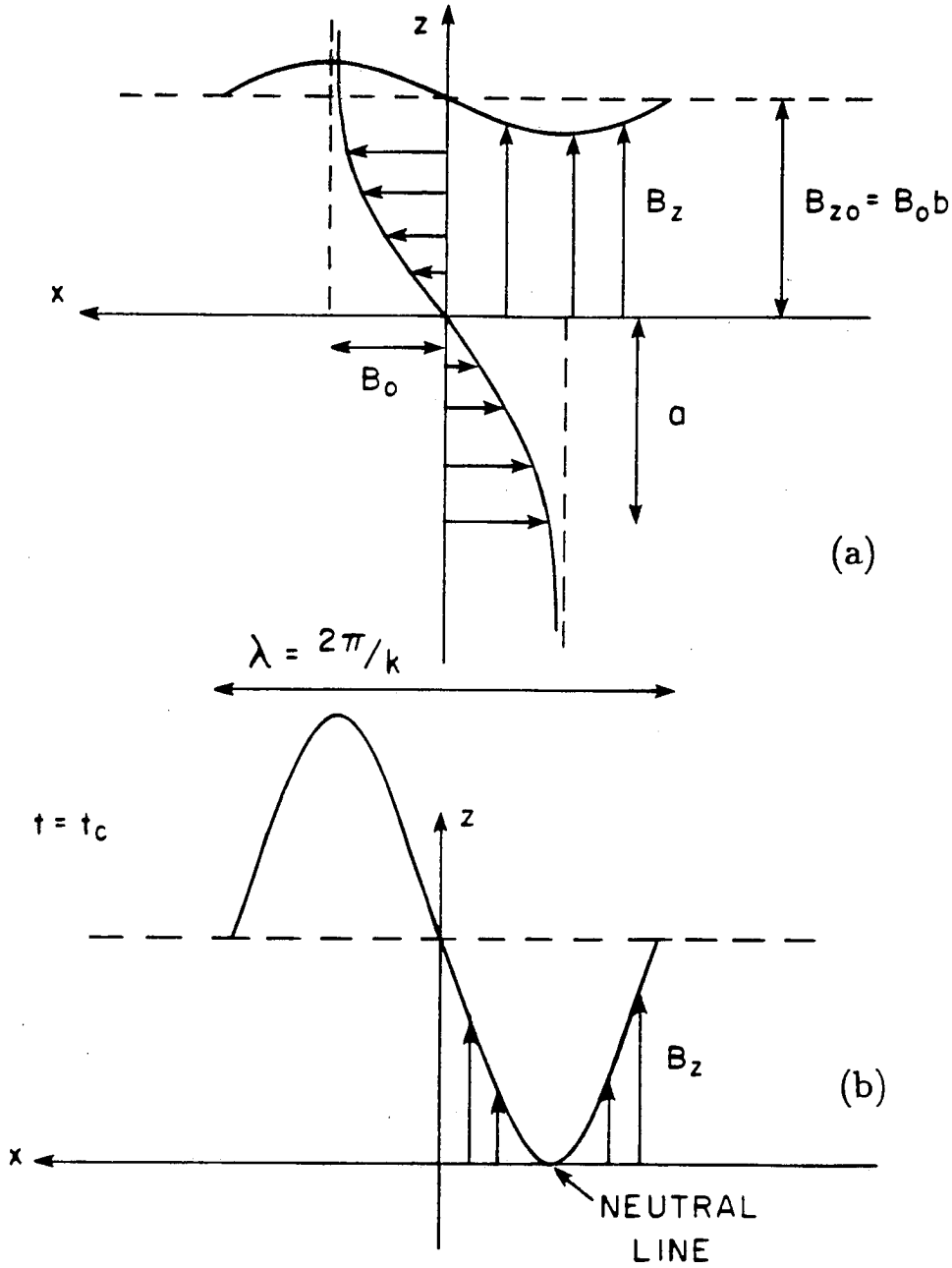

Figure 4.6: The magnetic field in the tail, including the tearing mode. $\psi_0 \ll b$. a) $t \ll t_c$, b) $t = t_c$.

earthward and one moving tailward, located at

$$x_{nl} = \frac{1}{k}\sin^{-1}\left(\frac{-b}{\psi_0 k e^{\gamma t}}\right). \tag{4.10}$$

As $\psi_0 k e^{\gamma t}$ gets to be much bigger than b, a series of islands appears with alternating X- and O-points.

Fig. 4.7 shows a perspective plot of the magnetic field lines and a few typical particle trajectories in the case $\psi_0 k e^{\gamma t} \gg b$. Fig. 4.8 shows the field lines and a typical particle trajectory for $\psi_0 k e^{\gamma t} \gtrsim b$. The magnetic field lines are generated by integrating $d\vec{x}/d\tau = \vec{B}(\vec{x})$. In the case shown, the dimensionless parameters are $b = .05$, $\psi_0 = 0.1$, $ka = .09$ and $\gamma/\omega_{0i} = 10^{-3}$. For $a = R_e = 6380\,km$ and $B_{x0} = 20\,nT$ this gives $B_z = 1\,nT$, the island width $\Delta_z = a\sqrt{2\psi_0} = 2840\,km$ and the growth rate $\gamma = 2 \times 10^{-3}\,sec^{-1}$ or 10 seconds for 20 e-foldings. The electric field is $E_y = B_0\psi_0\gamma/c = 1.22 \times 10^{-5}\,V/m$. The distance from the O-point to the X-point is $\pi/k = 33R_e$ where we have in mind that the magnetic field near the O-point connects to the near Earth dipole field and the expansion of the magnetic cavity at $2\pi/k = 66R_e$ eliminates the second X-point.

The particle orbit shown in Fig. 4.8 is typical of those in the ensembles used to calculate the net plasma currents and flow velocities (cf. Chapter 5.1). In the example shown the particle starts at 1b and arrives at 1e after $T\omega_{0i} \simeq 2 \times 10^3$, or $10^3\,sec$ for an ion. The particle's energy is given by $\mathcal{E} = (1/2)\,m(a\omega_{0i})^2\epsilon$ with $\epsilon = 5 \times 10^{-3}$ in the case shown. For ions the scale velocity is $a\omega_{0i} \approx 12200\,km/s$ and the energy is $\mathcal{E} = 3.9\,keV$. The initial pitch angle is $\theta = \cos^{-1}(v_{\|}/v) = \pi/4$. The particle follows the magnetic field surface into the region near the quasineutral sheet (where $B_x = 0$) with increasing $v_{\|}$ and decreasing $H_\perp = H - p_x^2/2m$ until $H_\perp$ is small enough that the effective z potential traps the particle in the well $V(z) \sim e^2B_0^2z^4/8m$ whereupon

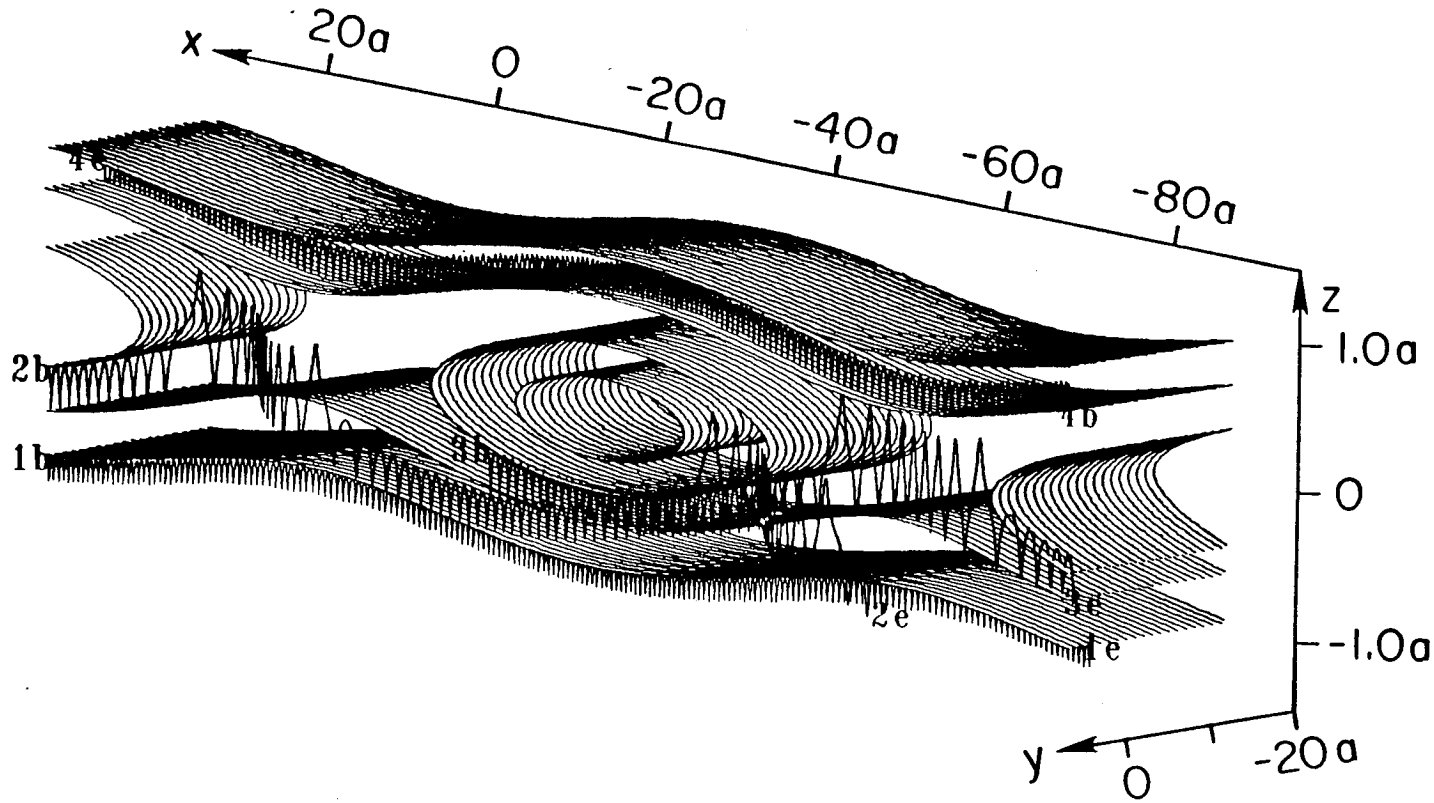

Figure 4.7: Typical particle trajectories in the full magnetotail fields. $\psi_0 \gg b$.

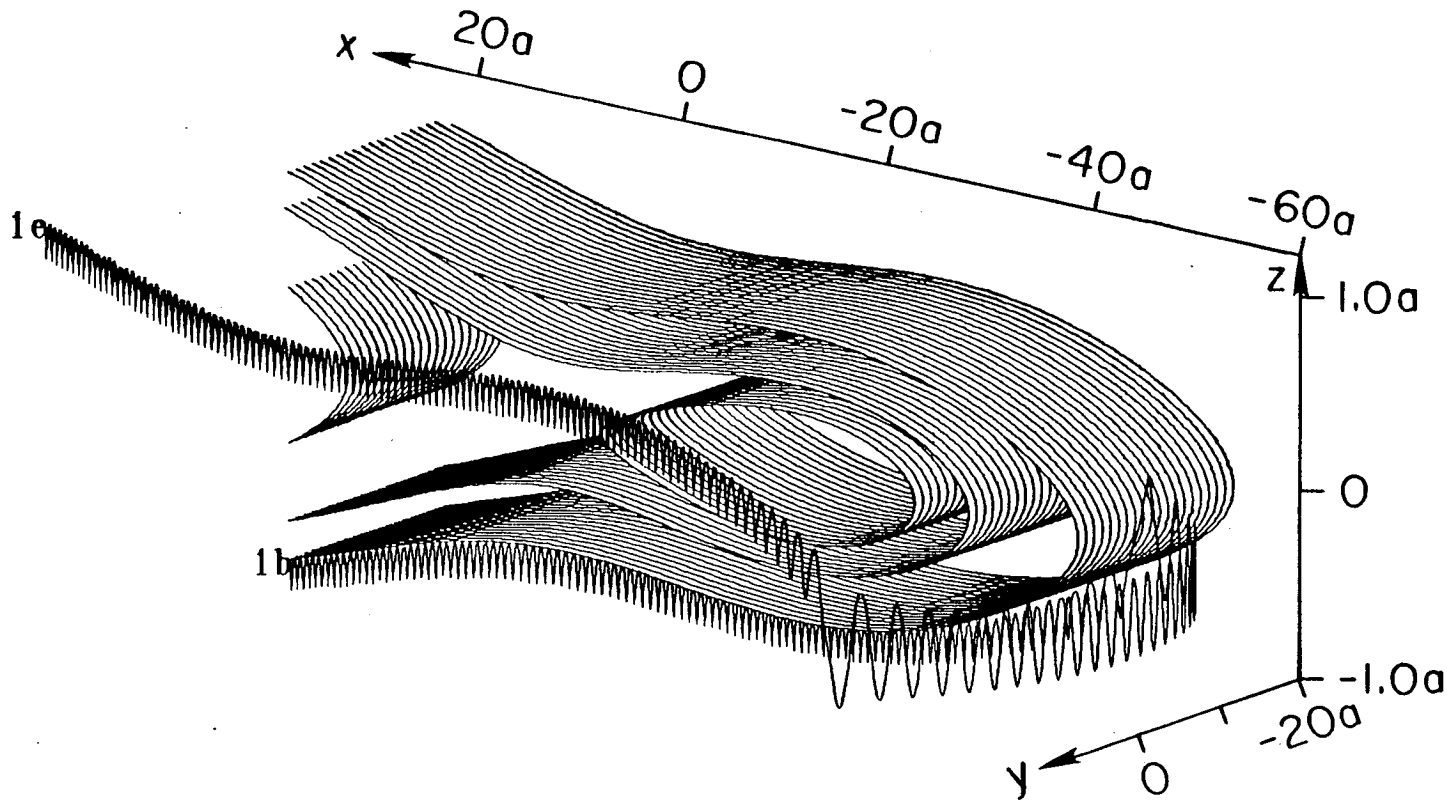

Figure 4.8: Typical particle trajectories in the full magnetotail fields. $\psi_0 k e^{\gamma t} \gtrsim b$.

the particle oscillates with the large vertical $z \sim \sqrt{va/\omega_{0i}}$ excursions across the quasineutral sheet. During these vertical oscillations the particle rotates around the vertical magnetic field until $p_x = mv_x \to -mv_x$ and then, at some moment depending on the phase of the z oscillations, connects on to a different magnetic surface and leaves the quasineutral sheet region. For not too small a vertical field the time in the sheet region is observed to be $\Delta t \simeq \pi/\omega_{z0} = \pi/b\omega_0$ (cf. Sec. 4.3.1). For $b \to 0$ (i.e. near the X-point) the relevant time in the neutral sheet is a fraction of the transit time π/kv_x across the X-point region. Thus we estimate the time for the particle to be in the sheet region as $\Delta t_x = \pi/(b\omega_0 + kv_x)$ (cf. Sec. 5.2). During this time the particle increases its Δv_y by the amount necessary to conserve $P_y = mv_y + (e/c)\psi(x,y,t)$ or $\Delta v_y \simeq (e/mc)\Delta t_x\, \partial_t\psi$. For particles outside the sheet region the conservation of P_y is satisfied by $d\psi/dt = \partial_t\psi + v_x\partial_x\psi + v_z\partial_z\psi \approx 0$ with little change to mv_y as shown by particles 1 and 4 in Fig. 4.7.

4.3.1 Electron Destabilization Revisited

We saw in Sec. 4.3 that the magnetic moment $\mu = E_\perp/B$ changes as the particle enters the chaotic region. That change, $\Delta\mu$, can be calculated in the same way ΔH was calculated in Part I, by evaluating

$$\Delta\mu = \int_{t_i}^{t_f} \frac{d\mu}{dt}\, dt$$

where at $t = t_i$ and $t = t_f$ the particle is on either side of the neutral sheet and far enough from it for the magnetic moment μ to be well defined. This calculation has been done for a number of different magnetic field configurations (eg. Hastie et. al., 1978; Chirikov, 1978; Birmingham, 1984). We outline the general method and calculate $\Delta\mu$ for our case in Appendix C. The change is

given by

$$\Delta\mu = \frac{\pi}{2^{3/4}\Gamma(9/8)}\left(\frac{\mu E}{B_0 b}\right)^{1/2}\cos\zeta_0\,\kappa^{1/4}e^{-\kappa^2}$$
$$\text{for} \quad \kappa > 1 \quad \text{and} \quad \epsilon < 1 \tag{4.11}$$

where ζ_0 is the gyrophase of the particle the moment it crosses the $z = 0$ plane, and

$$\epsilon = \frac{\rho_0}{a} \quad \text{and} \quad \kappa = \frac{b}{\sqrt{\epsilon}}. \tag{4.12}$$

The integral for $\Delta\mu$ is evaluated by first changing it to an integral over gyrophase and then deforming the path in the complex ζ-plane. The main contribution to the expression in Eq. 4.11 comes from the poles associated with the vanishing of the magnetic field, i.e. the neutral line (Hastie et. al., 1969). For $b \neq 0$ the poles are in the complex z-plane at $z_p = \pm iab$. The condition $\kappa > 1$ comes from the fact that in the analysis we only consider single crossings of the reversal layer (see Appendix C for details). Epsilon is the small parameter in the adiabatic approximation. The adiabatic invariant can be expanded in a power series in ϵ, in which the magnetic moment $\mu = E_\perp/B$ is only the first term. Since $\kappa = b\sqrt{(a/\rho_e)} = b/\sqrt{\epsilon}$, we see from Eq. 4.11 that $\Delta\mu \sim e^{-b^2/\epsilon}$, so the integral picks up the part of the change that cannot be expanded in a power series in ϵ.

A point of interest for us in Eq. 4.11 is the dependence of $\Delta\mu$ on the gyrophase, a dependence reminiscent of the dependence of ΔH on the phase β in Part I. It is this sensitive dependence of the change of the adiabatic constant on the phase of the fast oscillation that is the source of chaos in both systems.

In Figs. 4.11–4.15 we plot the time histories of the magnetic moment, pitch angle and gyrophase for particles in trajectories similar to the ones shown in Figs. 4.4, 4.7, 4.8, 4.9 and 4.10. The magnetic moment is defined by $\mu =$

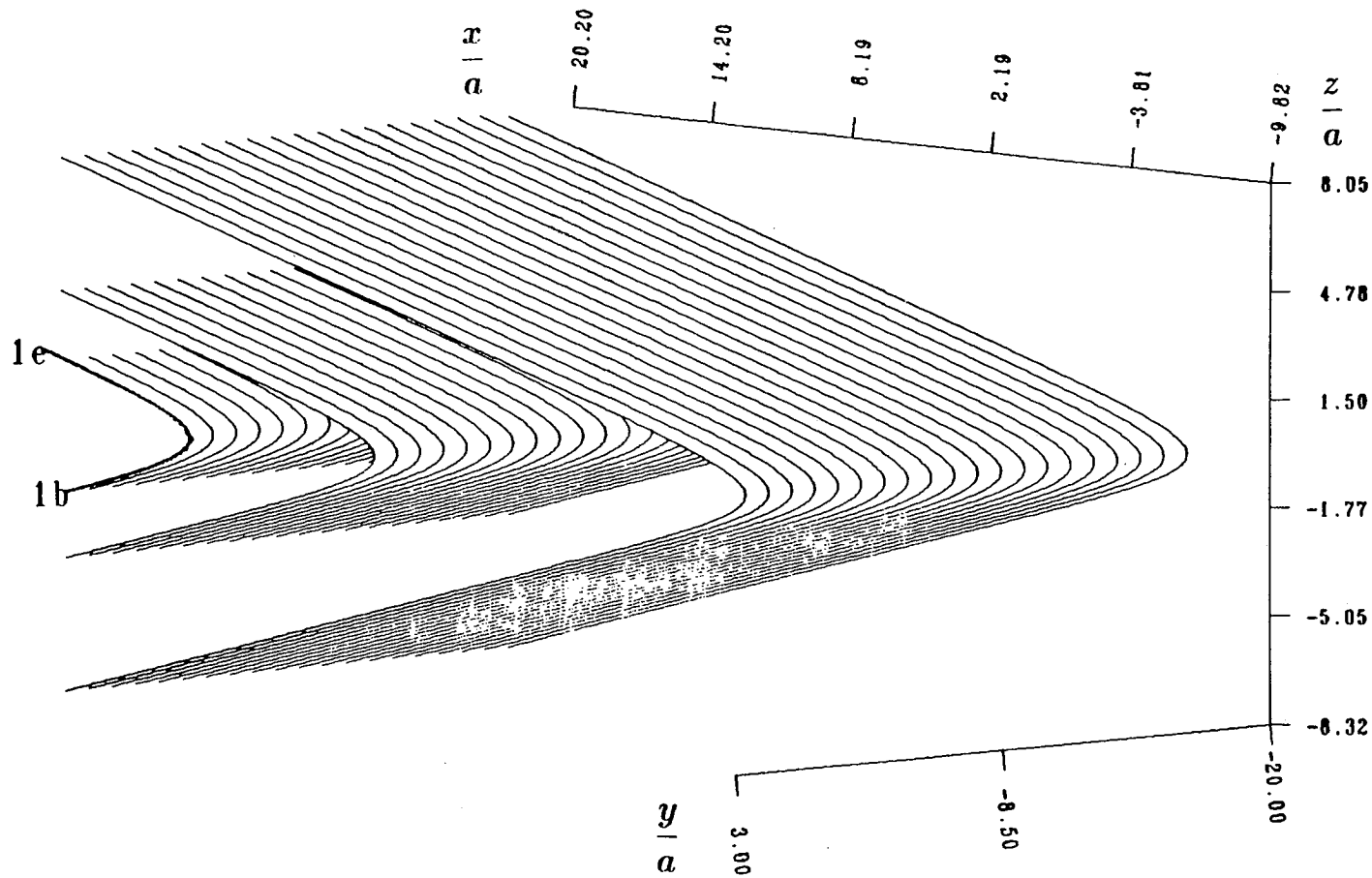

Figure 4.9: Particle trajectory for $\kappa > 1$. The particle only crosses the reversal layer once as it passes through the reversal layer.

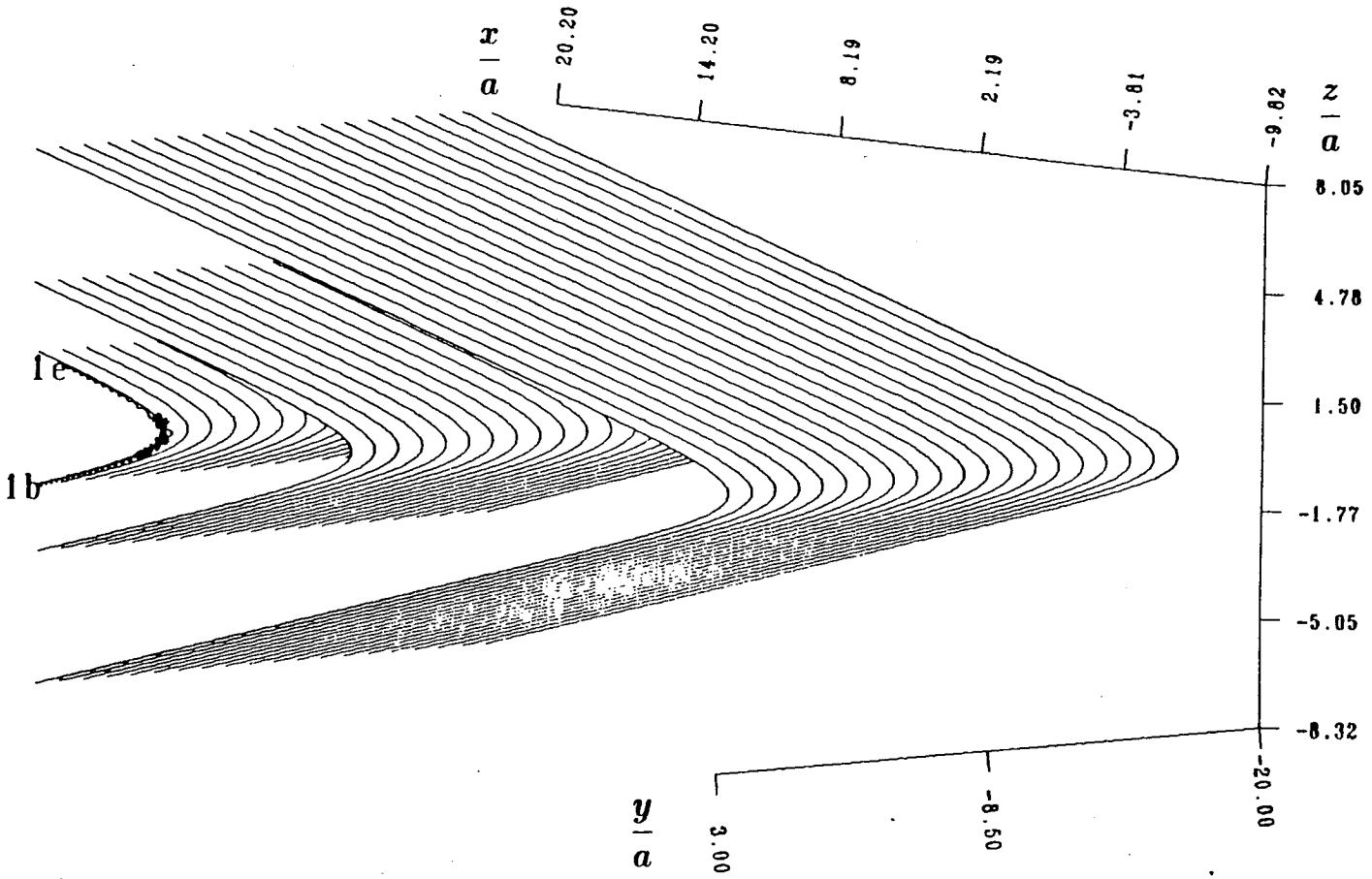

Figure 4.10: Particle trajectory for $\kappa > 1$. The particle can be seen mirroring twice as it enters the high field region.

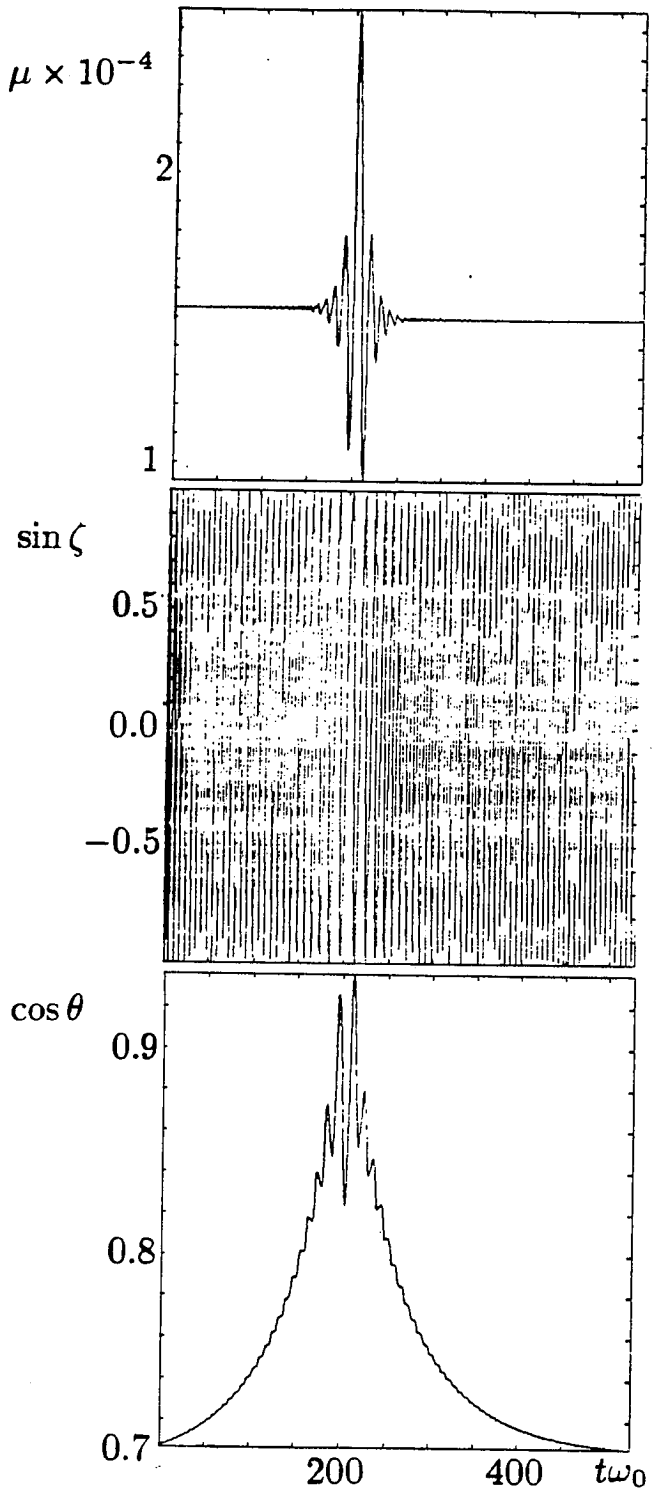

Figure 4.11: Time histories of μ, $\cos\theta$ and $\sin\zeta$. $b = 0.4$, $\epsilon = 0.018$, $\kappa = 2.99$.

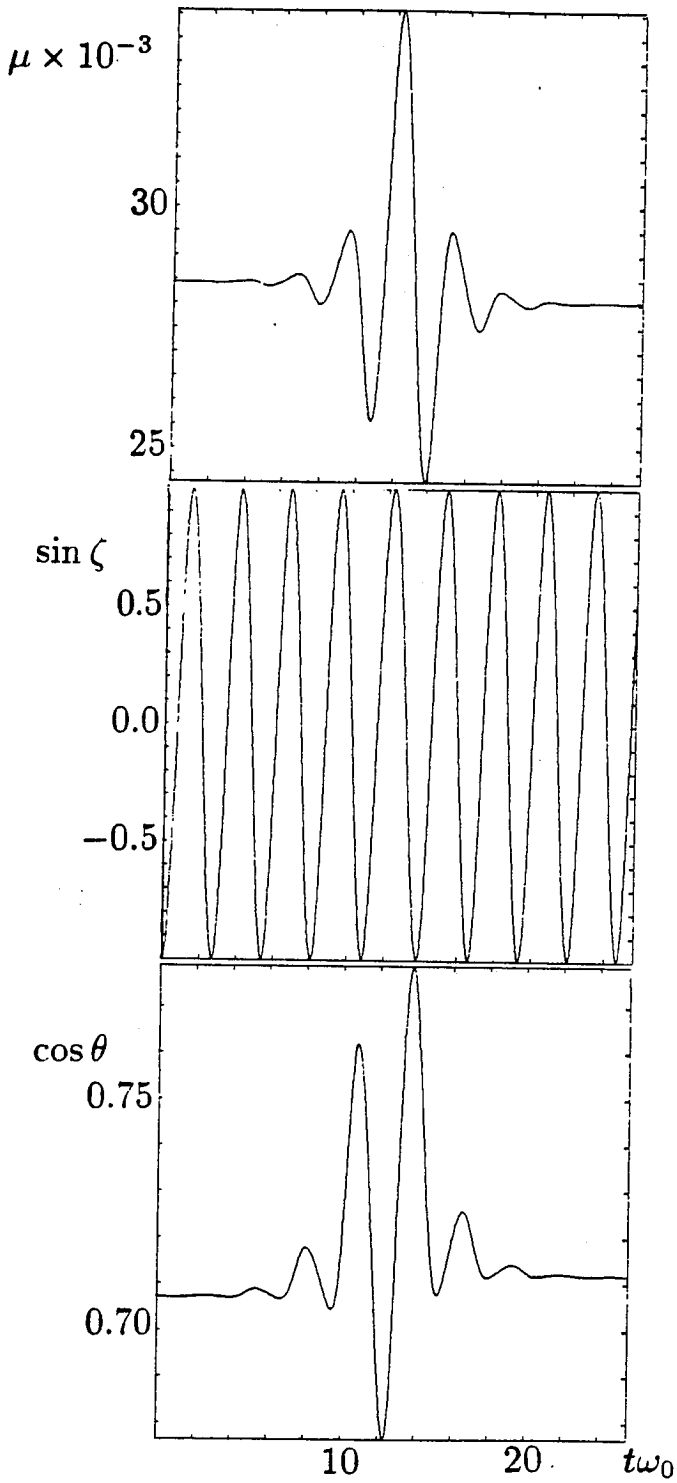

Figure 4.12: Time histories of μ, $\cos\theta$ and $\sin\zeta$. $b = 2.115$, $\epsilon = 0.365$, $\kappa = 3.5$.

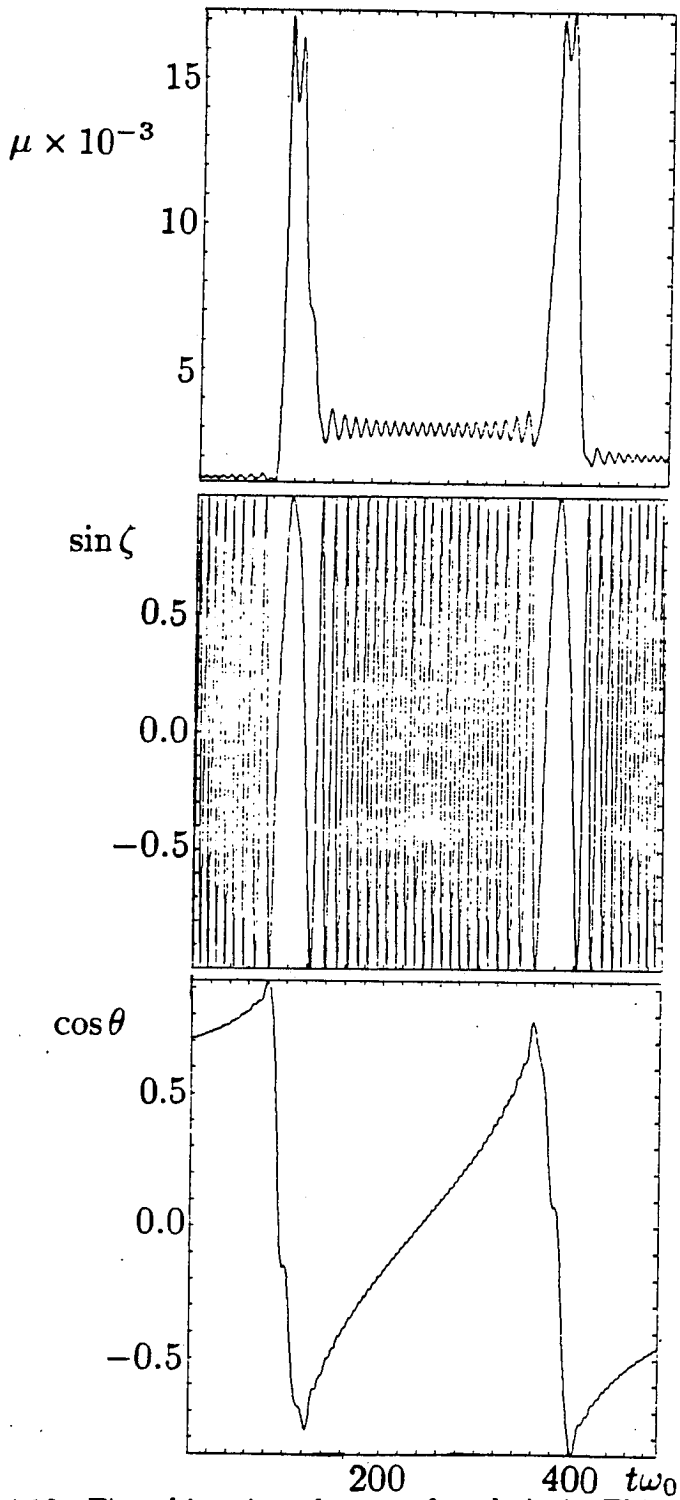

Figure 4.13: Time histories of μ, $\cos\theta$ and $\sin\zeta$. This particle has mirrored twice.

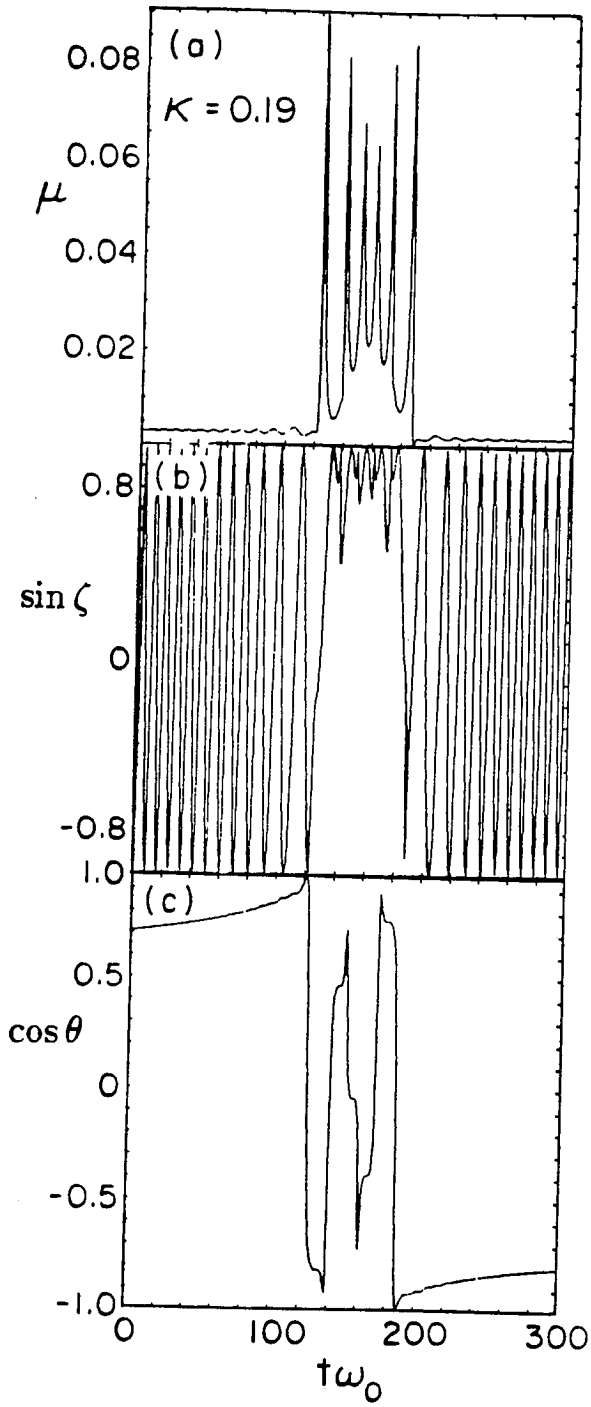

Figure 4.14: Time histories of μ, $\cos\theta$ and $\sin\zeta$. $\kappa = 0.19$. **The particle** is reflected at the reversal layer.

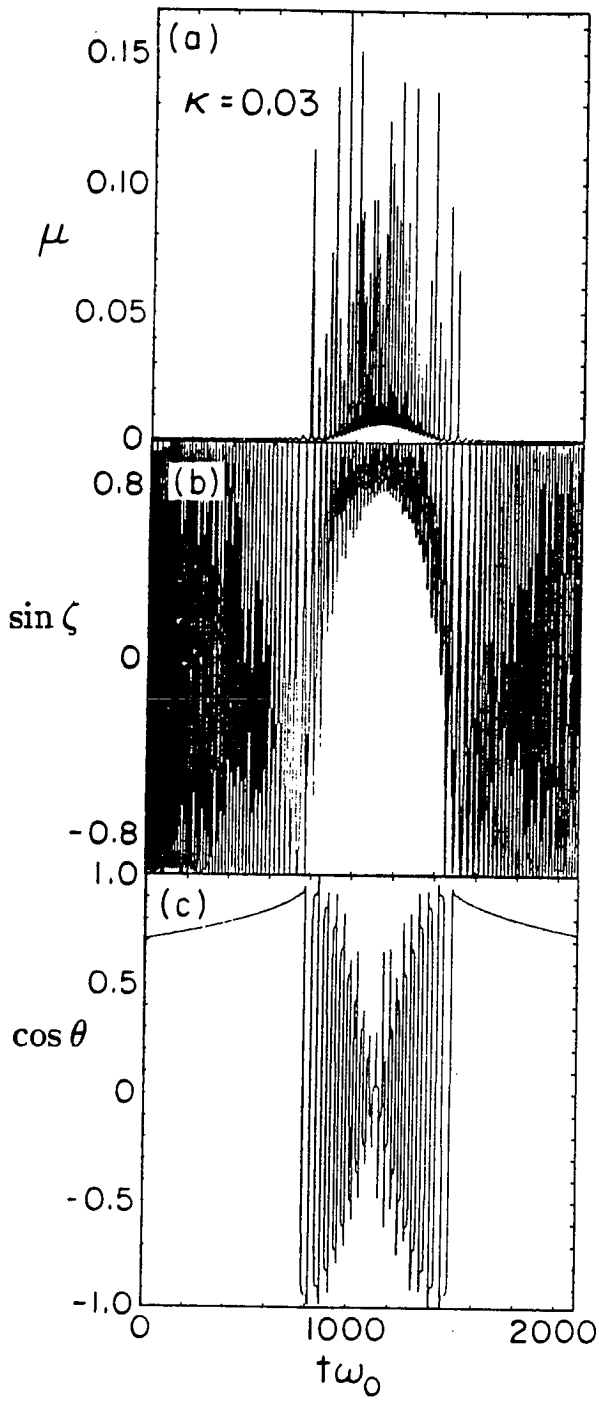

Figure 4.15: Time histories of μ, $\cos\theta$ and $\sin\zeta$. $\kappa = 0.03$. The particle goes through the reversal layer.

$E_\perp/B = mv_\perp^2/2B$ with $\vec{v}_\perp = \vec{v} - \hat{b}v_\parallel$ and $v_\parallel = \vec{v}\cdot\hat{b}$. The pitch angle is defined by $\cos\theta = v_\parallel/v$ and the gyrophase by $\cos\zeta = \vec{v}_\perp \cdot \hat{n}/|\vec{v}_\perp|$ where $\hat{n}$ is the direction of the magnetic field curvature and is given by $\hat{n} = (\hat{b}\cdot\nabla)\hat{b}/|(\hat{b}\cdot\nabla)\hat{b}|$. In Figs. 4.11 and 4.12 we plot the time histories of the magnetic moment, pitch angle and gyrophase for particles that have $\kappa > 1$. The trajectories correspond to the one shown in Fig. 4.9. The particle crosses the reversing layer only once between mirroring, and expression 4.11 for $\Delta\mu$ holds. In Figs. 4.14 and 4.15 the particles have $\kappa < 1$. The trajectories are similar to that in Fig. 4.4 and the particle crosses the reversing layer many times while gyrating around the normal field component. The particle in Fig. 4.15 is also reflected at the reversal layer back in the direction it came from (notice how $\cos\theta$ changes sign on either side of the crossing). Finally in Fig. 4.13 we show a particle that crosses the reversal layer, mirrors at the high-field region and crosses the reversal layer again, changing its magnetic moment by a different amount at every crossing. It corresponds to the trajectory shown in Fig. 4.10.

To show the exponential dependence of $\Delta\mu$ on κ, a feature similar to the dependence of ΔH on Ω in Part I, we write Eq. 4.11 as

$$G = -\ln\left[\frac{\Delta\mu}{\cos\zeta_0}\left(\frac{b}{\mu E}\right)^{1/2}\kappa^{-1/4}\right] \sim \kappa^2$$

and plot the values of G we calculate numerically against κ^2 in Fig. 4.16. The fact that the graph is a straight line means that the change in μ has an exponential dependence in κ^2 as predicted by 4.11. The slope of the graph is the coefficient of $-\kappa^2$. The slope is not constant with b, because in the analysis the coefficient of $-\kappa^2$ is not one (cf. Appendix C) but is rather given by

$$S(u') = \int_0^1 \frac{1-x^2}{[1-u'\sqrt{1-x^2}]^{1/2}}\,dx \tag{4.13}$$

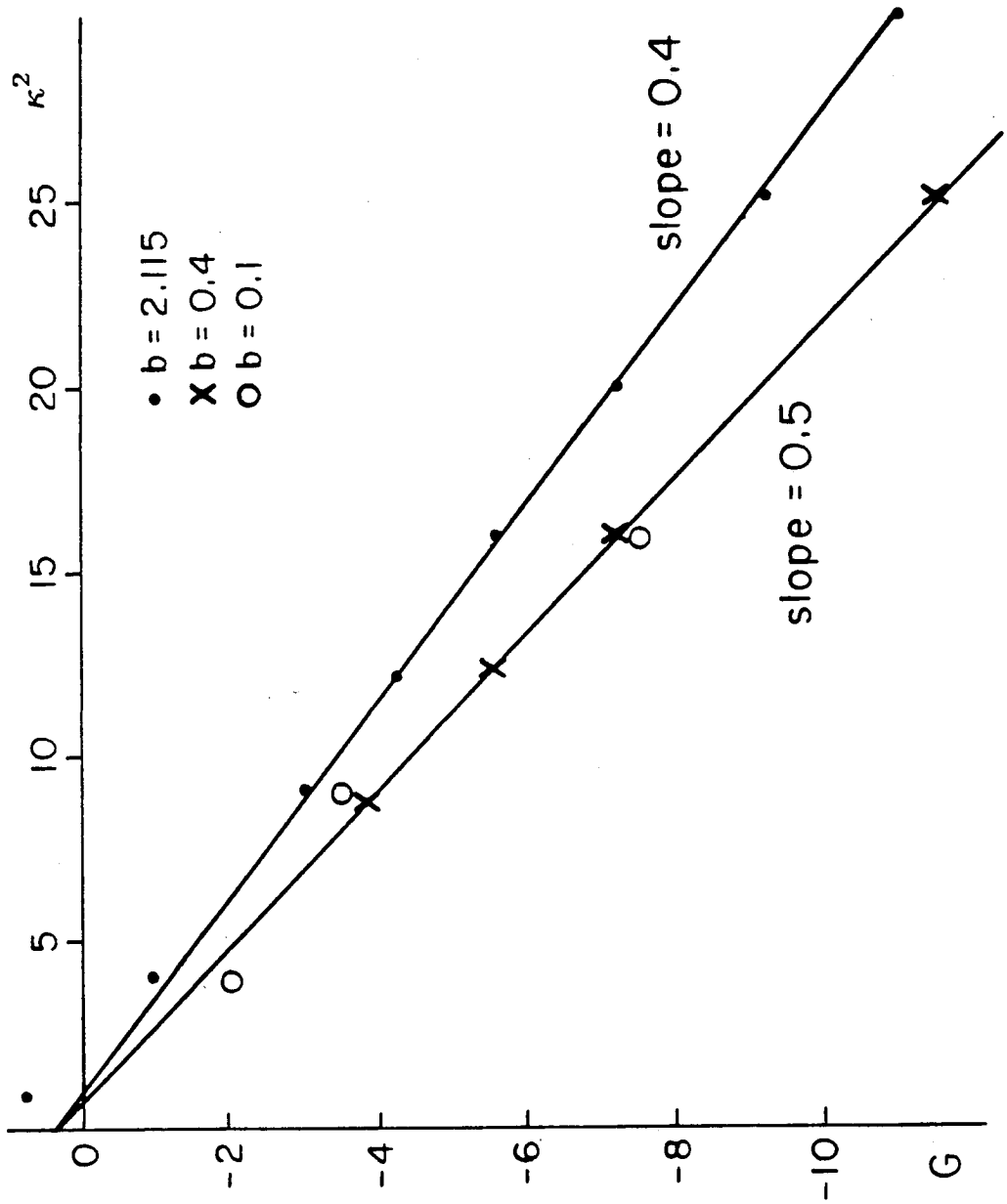

Figure 4.16: $G = \ln[(\Delta\mu/\cos\zeta_0)\kappa^{-1/4}\sqrt{b/\mu E}]$ plotted against κ^2. The slope gives the coefficient of $-\kappa^2$ in the exponent. For $b = 0.4$ the slope is 0.5, for $b = 2.115$ the slope is 0.4. For $b = 0.1$ the slope is also approximately 0.5.

where

$$u' = \left(\frac{v_\perp}{v}\right)^2 = sin^2\theta_0 \tag{4.14}$$

with θ_0 being the pitch angle of the particle as it crosses the reversal layer. Eq. 4.13 is a slowly varying function of u' that lies within a factor of two of the exact value for all value of u' except those close to $u' = 1$ (Coronoti, 1980). For values of the normal field typical in the magnetotail ($b = 0.05$–$b = 0.2$), the coefficient of $-\kappa^2$ is close to one-half.

Due to the $\cos\zeta_0$ dependence of $\Delta\mu$, the jumps in the value of the magnetic moment every time the particle passes through the neutral line region are statistically uncorrelated, especially for the particles for which

$$\Delta\zeta \approx \frac{1}{2}\tau_b\omega_0 \gg 1$$

where τ_b is the bounce period of the particle in the magnetic mirror. This allows us to treat the problem as a random walk (eg. Chirikov, 1979) and write the diffusion coefficient as

$$D_\mu = \left\langle \frac{(\Delta\mu)^2}{2\Delta t} \right\rangle \tag{4.15}$$

where Δt is the time between two successive jumps in the value of the magnetic moment. In our case that time is equal to half the bounce period τ_b of the particle as it mirrors in the high-field region, so that

$$D_\mu = \frac{\langle(\Delta\mu)^2\rangle}{\tau_b}. \tag{4.16}$$

The bounce period τ_b can be evaluated using the fact that the magnetic moment is a good adiabatic invariant far from the sheet (Coroniti, 1980) and is given by

$$\begin{aligned} \tau_b &= \frac{4a}{B_0}\left(\frac{mB_n}{2\mu}\right)^{1/2}\int_1^{u_0}\frac{u^2}{(u_0-u)^{1/2}(u^2-1)^{1/2}}\,du \\ &\approx \frac{16aE}{3B_0^2 b}\sqrt{\frac{m}{2}}\frac{1}{\mu^2} \end{aligned} \tag{4.17}$$

where $u = 1/\sin^2\theta$, θ is the pitch angle, θ_0 is the pitch angle of the particle as it crosses the $z = 0$ plane, and we have used the approximation $u_0 = 1/\sin^2\theta_0 \gg 1$.

Using the estimate for the diffussion coefficient given by Eq. 4.16 with $\Delta\mu$ given by Eq. 4.11, Büchner and Zelenyĭ (1987) calculated the tearing mode growth rate to be

$$\gamma_{BZ} = 0.25\,\omega_0 \left(\frac{T_e + T_i}{T_e}\right) \frac{b^{5/2}}{\kappa_e^{3/2}\sqrt{ka}} e^{-2\kappa_e^2} \tag{4.18}$$

under the condition that

$$b < ka < (\pi b)^{1/3} \tag{4.19}$$

The main feature of the above expression for the growth rate is its exponential dependence on κ. For $\kappa_e \gg 1$ the growth rate is exceedingly small. As κ_e decreases the growth rate increases exponentially until, for $\kappa_e \to 1$, it can be more than an order of magnitude greater than the one-dimensional case (Coppi et. al.). For typical magnetotail parameters (cf. Section 3.3) and for $\kappa_e \to 1$ the above expression gives a growth time of a few seconds.

We finally need to discuss the value of time the particle spends in the reversal layer, a quantity that enters directly in the calculation of $\langle j \cdot E \rangle$and the growth rate (cf. Eq. 3.12). As we mentioned in Sec. 4.3 we estimate that, for $\kappa < 1$ the time is given by

$$\tau \approx \frac{\pi}{kv + b\omega_0}$$

so that, for $kv \ll b\omega_0$,

$$\tau\omega_0 \approx \frac{\pi}{b}.$$

In Fig. 4.17 we plot the time histories of the magnetic moment and pitch angle for different values of the normal field component. In all three cases $\tau \lesssim \pi/b$. The value of kv ranges between 10^{-3} and 10^{-2}.

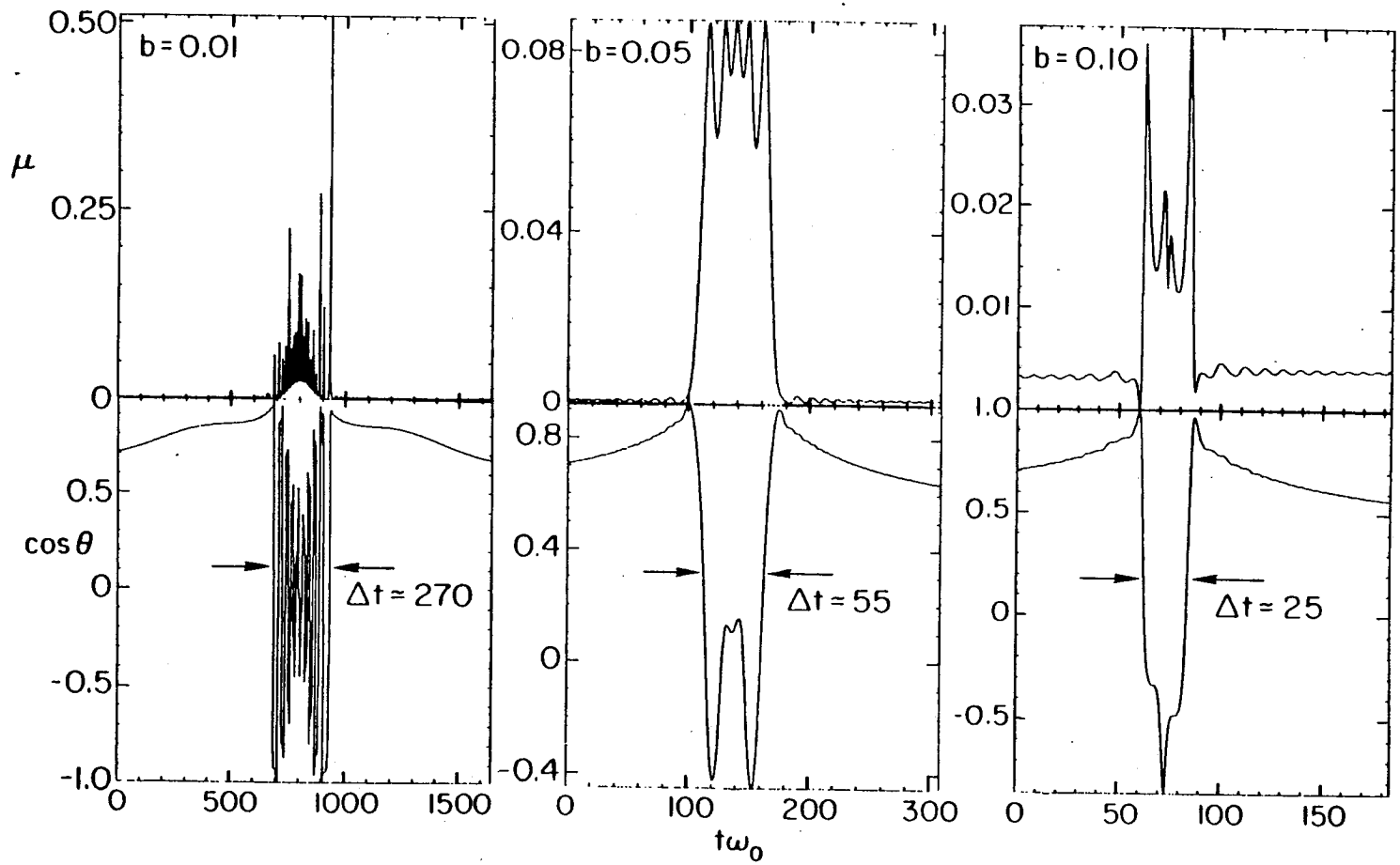

Figure 4.17: Time histories of μ and $\cos\theta$ for different values of b, for $\kappa < 1$. The time the particle spends in the neutral layer is approximatelly $\pi/b\omega_0$.

Chapter 5

NUMERICAL RESULTS

5.1 Description and Testing of the Code

As we mentioned in Sec. 3.2, we use a test particle code to calculate numerically the width of the current layer Δz and the in-phase part of the current $\langle j \cdot E \rangle$. The numerical results are used to obtain analytical expressions for Δz and τ which are then substituted into Eq. 3.12 to give the collisionless reconnection growth rate γ.

To advance the particles we use the equations of motion for the full system, which are given by

$$
\begin{aligned}
\dot{x} &= v_x \qquad \dot{y} = v_y \qquad \dot{z} = v_z \\
\dot{v}_x &= \omega_0 b v_y + \omega_0 \psi_0 v_y k \sin(kx) e^{\gamma t} \\
\dot{v}_y &= -\omega_0 b v_x + \omega_0 v_z \tanh\left(\frac{z}{a}\right) + \omega_0 \psi_0 \gamma \cos(kx) e^{\gamma t} - \\
&\quad -\omega_0 \psi_0 v_x k \sin(kx) e^{\gamma t} \\
\dot{v}_z &= -\omega_0 v_y \tanh\left(\frac{z}{a}\right).
\end{aligned}
$$

We introduce dimensionless variables by scaling length to the perturbation wavelength $\lambda = 2\pi/k$, time to the ion gyroperiod in the asymptotic field $T_{0i} = 2\pi/\omega_{0i} = 2\pi(m_i c/eB_0)$, mass to the ion mass and charge to the unit charge e

(electrons have charge $-e$). The equations of motion thus become

$$
\begin{aligned}
\dot{x} &= v_x \qquad \dot{y} = v_y \qquad \dot{z} = v_z \\
\dot{v}_x &= 2\pi b v_y + (2\pi)^2 \psi_0 v_y \sin(2\pi x) e^{\gamma t} \\
\dot{v}_y &= -2\pi b v_x + 2\pi v_z \tanh\left(\frac{z}{a}\right) + 2\pi \psi_0 \gamma \cos(2\pi x) e^{\gamma t} - \\
&\quad -(2\pi)^2 \psi_0 v_x \sin(2\pi x) e^{\gamma t} \\
\dot{v}_z &= -2\pi v_y \tanh\left(\frac{z}{a}\right).
\end{aligned}
\tag{5.1}
$$

where, in our units, $k = \omega_{0i} = 2\pi$. From now on all values given for the parameters and all variables in equations will be dimensionless unless otherwise stated. Whenever needed to avoid confusion, the dimensionless quantities will be denoted by a hat (eg. $\hat{x} = x/\lambda$). The system is described by four parameters. The amplitude of the tearing mode ψ_0, the normal magnetic field component b, the aspect ratio of the tearing mode $ka = 2\pi a$ and its growth rate γ.

We are careful to fully resolve the smallest time and space scales in the problem. For the parameters used, the smallest length scale is the particle gyroradius in the asymptotic field, $\rho_0 = v/\omega_0$ with v the total particle velocity. The length scale over which the magnetic field reverses direction, a, is always at least two orders of magnitude larger than ρ even in very high energy test runs, and the wavelength of the tearing perturbation is the longest scale in the system. Approximate values for these parameters in the magnetotail are $\lambda = 8\text{-}80\, R_e$ and $a \approx 1\, R_e$ where $R_e = 6380\, km$ is the radius of the Earth. In contrast the electron gyroradius is of the order of a few kilometers, and the ion gyroradius a few hundred kilometers. The smallest timescale is the particle gyroperiod in the asymptotic field $T_0 = 2\pi/\omega_0 = 1$. The only other timescale in the problem is the tearing mode growth time, $\tau_e = 1/\gamma$, and the shortest growth time we used was 20 ion gyroperiods.

Sample populations of 16000-64000 particles are advanced in time according to the equations of motion 5.1 using a fourth order Runge-Kutta method. Electrons and ions are treated separately so that a realistic ion to electron mass ratio of 1836 can be used. The electron gyrofrequency is therefore $\omega_{0e} = -1836 \times (2\pi)$. The code is completely vectorized. The time step h is chosen so that the particle (electron or ion) gyroperiod is adequately resolved and the final (cumulative) error in the particle position $|\delta\vec{x}|$ is much smaller than the particle gyroradius in the asymptotic field. To get an estimate for the error in the particle position a small percentage of particles ($\sim 1\%$) are also advanced with a sixth order Runge-Kutta and half the timestep. The estimated error $|\delta\vec{x}|$ is then given by

$$|\delta\vec{x}| = |\vec{x}_{h/2} - \vec{x}_h| \tag{5.2}$$

where $\vec{x}_{h/2}$ is the position of the particle calculated with the higher order method and half the timestep, while $\vec{x}_h$ is the position calculated with the same method and timestep used for all the particles. The lowest value of T_0/h used in any run is 110, and the lowest value of $\rho/|\delta\vec{x}|$ is of the order of 10^2.

The equations of motion are periodic in the x-direction so the particles are kept in a cell with an x-dimension of one, but are allowed to move freely in z. The particles are loaded with a flat distribution in both velocity and configuration space, i.e.

$$-ax' \leq x \leq ax' \quad , \quad -z' \leq z \leq z' \quad , \quad -v' \leq v_j \leq v'. \tag{5.3}$$

The velocity space limit v' is chosen so that the average particle energy will be approximately $2\,keV$ for ions and $1\,keV$ for electrons. For ions the system is advanced for a maximum $200 - 300\,T_{0i}$, which is approximately one to four exponentiation times for the values of γ used. The electrons were advanced

for a maximum of $\sim 2000\,T_{0e}$, which is approximately one T_{0i}. We can look at the average density, velocity (x, y and z-component), current (x, y and z-component), temperature and $\langle j \cdot E \rangle$ as a function of x and z, at any given time t.

The average velocity is defined by

$$\langle v_j \rangle_{(s,t)} = \frac{v_0}{n} \sum_{i=1}^{n} \hat{v}_j^i = v_0 \langle \hat{v}_j \rangle_{(s,t)} \tag{5.4}$$

where n is the number of particles whose s-coordinate is in the range $s \rightarrow s + \delta s$ irrespective of the value of the other coordinate, and $\hat{v}_j^i$ is the j-component of the dimensionless velocity of the ith particle in units of the scale velocity $v_0 = \omega_{0i}/k$.

Using the average velocity we can define the current by

$$j_j(s,t) = e\rho_p \langle v_j \rangle \tag{5.5}$$

where ρ_p is the real particle number density and $\langle v_j \rangle$ the average velocity of all particles whose s-coordinate has a value between s and $s + \delta s$. We therefore have

$$\begin{aligned} \rho_p &= \frac{n_r}{\delta s(a\lambda^2)} = \frac{n(\rho_n a\lambda^2/N)}{\delta s(a\lambda^2)} \\ &= \rho_n \frac{n}{N\delta s} \end{aligned} \tag{5.6}$$

where n has the same meaning as in Eq. 5.4, N is the total number of particles in the simulation, n_r the number of real particles simulated by n, $\rho_n = 0.1\ cm^{-3}$ the real number density in the magnetotail and δs the dimensionless cell size. The factor $n/N\delta s$ is a density factor that describes how the density at position s differs from the average magnetotail number density ρ_n. If $n = N\delta s$, then

$\rho_p = \rho_n$.With that definition of the density we can now rewrite 5.5 as

$$\begin{aligned} j_j(s,t) &= e\rho_p\langle v_j\rangle_{(s,t)} = e\frac{\rho_n n}{N\delta s}v_0\frac{\sum_{i=1}^n \hat{v}_j^i}{n} \\ &= e\rho_n v_0\left(\frac{1}{N\delta s}\sum_{i=1}^n \hat{v}_j^i\right) = j_0\langle\hat{j}_j\rangle_{(s,t)} \end{aligned} \tag{5.7}$$

where $j_0 = e\rho_n v_0$ is the scale current.

The in-phase part of the reconnection current $\langle j \cdot E\rangle$ is computed in the same way by using

$$\begin{aligned} \langle j\cdot E\rangle_{(s,t)} &= (e\rho_n v_0)\left(B_0\psi_0\frac{\gamma}{c}\right)\left(\frac{1}{N\delta s}\sum_{i=1}^n \hat{v}_z^i\cos(2\pi\hat{x}^i)\right) \\ &= (e\rho_n v_0)\left(B_0\psi_0\frac{\gamma}{c}\right)\langle\hat{j}\cdot\hat{E}\rangle \end{aligned} \tag{5.8}$$

and the temperature is given in keV using

$$\begin{aligned} &\frac{1}{2}m\langle v^2\rangle = \frac{1}{2}mv_0^2\langle\hat{v}^2\rangle \\ &\langle\hat{v}^2\rangle = \left\langle(\hat{v}_x - \langle\hat{v}_x\rangle)^2\right\rangle + \left\langle(\hat{v}_y - \langle\hat{v}_y\rangle)^2\right\rangle + \left\langle(\hat{v}_z - \langle\hat{v}_z\rangle)^2\right\rangle \end{aligned} \tag{5.9}$$

An important point to note here is that time enters explicitly the equations of motion 5.1 exclusively through the combination $\psi_0 e^{\gamma t}$, so that a sweep in the value of ψ_0 is equivalent to running longer times, with only the initial conditions distinguishing the two cases. This observation is supported qualitatively by the simulations and was used in several occasions to shorten lengthy runs. The reference value of γ used in the runs was $\gamma = .01$, corresponding to a growth time of $100\,T_{0i} \approx 5\,min$.

5.2 Numerical Results

We have fifteen ion runs and four of the much more expensive electron runs. Although ninteen runs are insufficient for a systematic exploration of the

parameter space (there are four parameters that describe the system, ψ_0, b, ka and γ), their qualitative results are so similar, even for widely different values of the parameters, that we feel confident we can draw broad conclusions about the behavior of the system even from a limited sample. We will go here in detail through two runs (one for ions and one for electrons) that exibit the main behavior patterns of the system.

For the ion run, the dimensionless variables are $\psi_0 = 0.001$, $b = 0.05$, $\gamma = 0.01$, and $a = 0.02$. Substituting these values into Eq. 4.9, we find that the neutral line will appear at time $t = 207.4$ (the dimensionless time is in units of ion gyroperiods, $T_{0i} = 2\pi/\omega_{0i} = 3.28\ sec$). In Figs. 5.1–5.5 we show plots of the phase space and the density at different times. On the phase space plot we also superimpose a sample 200 particles. The dashed vertical lines are located at $z = \pm a$. As we see in Fig. 5.1-a and -b, the particles are loaded at time $t = 0$ with a flat distribution between $z = -a$ and $z = a$, and over a whole wavelength in x. The initial velocity distribution is also flat in all velocity components ($-v'_j < v_j < v'_j$, cf. Eq. 5.3), with $v'_j = 1.4 \times 10^{-4}$ so that the initial temperature is only $0.8\,eV$. As we shall see, even this run, with a very low initial temperature, will give us results qualitatively very similar to runs with more realistic initial temperatures.

In Fig. 5.2-a and -b we show a phase space plot, and the particle density ρ plotted against x and z at time $t = 83.3$. We see that, apart from a depression in the density around $z = \pm 0.2a$ the picture remains relatively unchanged. In particular, even after 83 ion gyroperiods the particles have not left the area in which they were placed at $t = 0$. At time $t = 183.3\,T_{0i}$, less than 25 ion gyroperiods before the neutral line appears, the density profile (Fig. 5.3-b) has changed. The particles are concentrated in a very narrow channel around

the reversal layer at $z = 0$, while there is an appreciable depression in the x density at the area where the in-phase current flows (cf. Fig. 5.7). Although some particles are now outside $z = \pm a$, the bulk is still inside (notice how the density falls off steeply outside $z = \pm 1$). The concentration around the reversal layer and the deepening of the depression in the x density at the point of maximum current flow continue (cf. Fig. 5.4) until, long after the appearance of the neutral line, the magnetic island expands well beyond $\pm a$ and all particles are expelled from the neutral line region (Fig. 5.5). Our run is terminated shortly afterwards, since we can no longer make any meaningfull measurements of the current or temperature in the neutral line area.

The time history of the in-phase current $\langle j \cdot E \rangle$and the particle temperature is shown in Figures 5.6 through 5.9. After only 16.7 gyroperiods (Fig. 5.6) appreciable current is flowing through a well defined channel (at least in z, the channel in x will take a little longer to develop) and the temperature has increased by a factor of two to three in the same narrow channel in which the current flows. Both the temperature and the magnitude of the current will continue to grow in time and the temperature profile will broaden a little in z, but the picture will remain qualitatively the same until shortly before the appearance of the neutral line. In Fig. 5.7 we show the current and temperature at time $t = 166.7\, T_{0i}$, approximately fourty gyroperiods before the neutral line appears. The value of the current is now higher and the channel in x is better defined, but the main difference is that the temperature profile in z, which was getting broader, has just developed a new narrow channel around $z = 0$, where the temperature is going to increase dramatically between now and the appearance of the neutral line. Also the temperature profile in x has started to develop a sharp gradient at the point where the neutral line is going to appear (at $x = -\lambda/4$). Fig. 5.8 shows the current and temperature at time

$t = 216.7$, just nine gyroperiods after the appearance of the neutral line. The temperature in the narrow channel around the reversal layer has increased by almost a full order of magnitude while the rest of the temperature profile in z has broadened even more, and in x the temperature gradient has become even bigger, with high temperatures being confined to tailward of the neutral line at $x = -\lambda/4$. Finally in Fig. 5.9 we show the current and temperature profiles at time $t = 273.3$. Although some current is still flowing, it will soon disappear as the last few remaining particles are being expelled from the area. The temperature profile in z has already crashed in the center, with all the energetic particles expelled from the center and injected into the Plasma Sheet Boundary Layer (PSBL) where the temperature is now a few keV, close to the observed 2–5 keV.

There are two points that need to be stressed here. One is that when we calculate the temperature we subtract the average velocity (cf. Eq. 5.9), so what we plot is indeed the temperature and not the total particle energy. The other point is that although we started with an extremely low temperature ($0.8\,eV = 8 \times 10^{-4}\,keV$) we ended up with temperatures of a few keV, comparable to the actual temperatures in the tail. When we start with more realistic temperatures, (eg. $0.2\,keV$) the overall heating is much lower than the four orders of magnitude we saw in this run, and the final temperature in the PSBL is a little higher (8–10 keV) but still close to the observed values. Also, if we start the run at a time closer to the time the neutral line appears (by using a larger ψ_0, see Sec. 5.1 above) the system will still end up with approximately the same temperature. This tendency of the system to end up at the same state (qualitatively) around the time of the appearance of the neutral line is quite general and not confined to the temperature, as we shall see later.

In Fig. 5.10 we show the time history of the x (earthward-tailward) component of the particle velocity. At $t = 33.3$, there is a small (approximately $15\,km/sec$) earthward drift in a narrow channel around the reversal layer at $z = 0$ (Fig. 5.10-a). At later times, both before (Fig. 5.10-b) and shortly after the appearance of the neutral line (Fig. 5.10-c), the channel gets a little wider and the velocity is higher, but still quite low, of the order of 40–80 km/sec. After the particles are expelled from the neutral line region and into the PSBL (Fig. 5.10-d) the earthward streaming velocity rises quickly to approximately $900\,km/sec$. Earthward streaming ions with speeds "in excess of $400\,km/sec$" have been observed in the PSBL (DeCoster and Frank, 1979). Again, as in the case of the particle temperature, the qualitative picture is insensitive to initial conditions. In particular, the final earthward streaming velocity in the PSBL is always in the region of a few hundred kilometers per second.

For the electron run the dimensionless parameters are $b = 0.003$, $a = 0.02$ and $\gamma = 0.01$. Since the electron gyrofrequency is 1836 times higher than the ion gyrofrequency, following an electron run over several ion gyroperiods is prohibitively expensive. We therefore use the fact that time and ψ_0 are equivalent (see Sec. 5.1 above) to study the system at different times. This particular run was divided into two parts. In the first we use $\psi_0 = 4.0 \times 10^{-4}$, which places the system $17.7\,T_{0i}$ before the appearance of the neutral line (cf. Eq. 4.9), and in the second we use $\psi_0 = 6.0 \times 10^{-4}$, which places the system $22.8\,T_{0i}$ after the appearance of the neutral line. We will henceforth disregard the value of ψ_0, and refer to the two parts of the run by the equivalent time. The run at $t = -17.7$ for instance, or the early run, is the part with $\psi_0 = 4.0 \times 10^{-4}$. Similarly the late run is the part with $\psi_0 = 6.0 \times 10^{-4}$. In both cases the initial distribution was flat in both configuration and velocity space, with $v_j' = 1.4 \times 10^{-4}$, which gives an initial temperature of $5 \times 10^{-5}\,keV$.

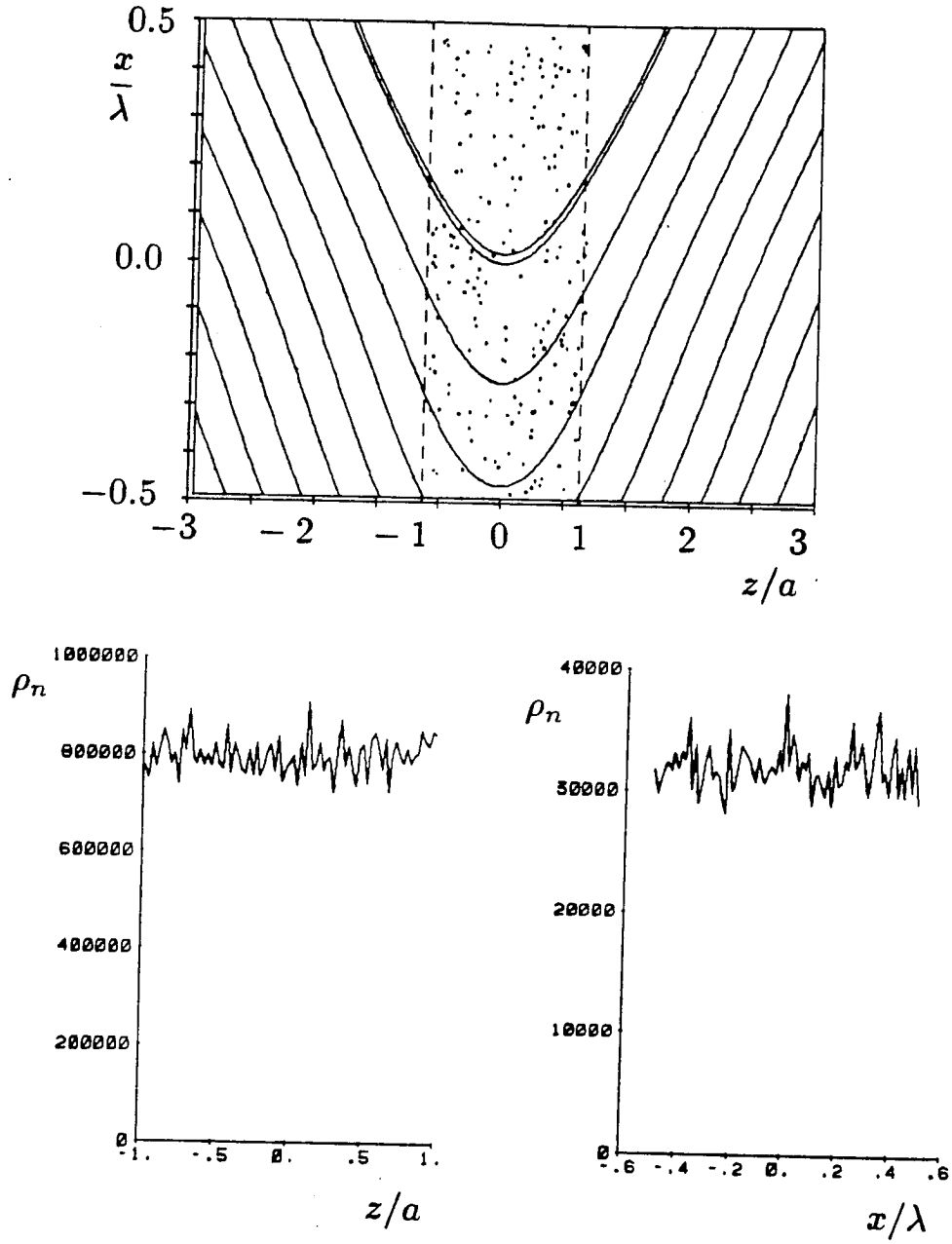

Figure 5.1: Phase space and density for the ion run. $t = 0$

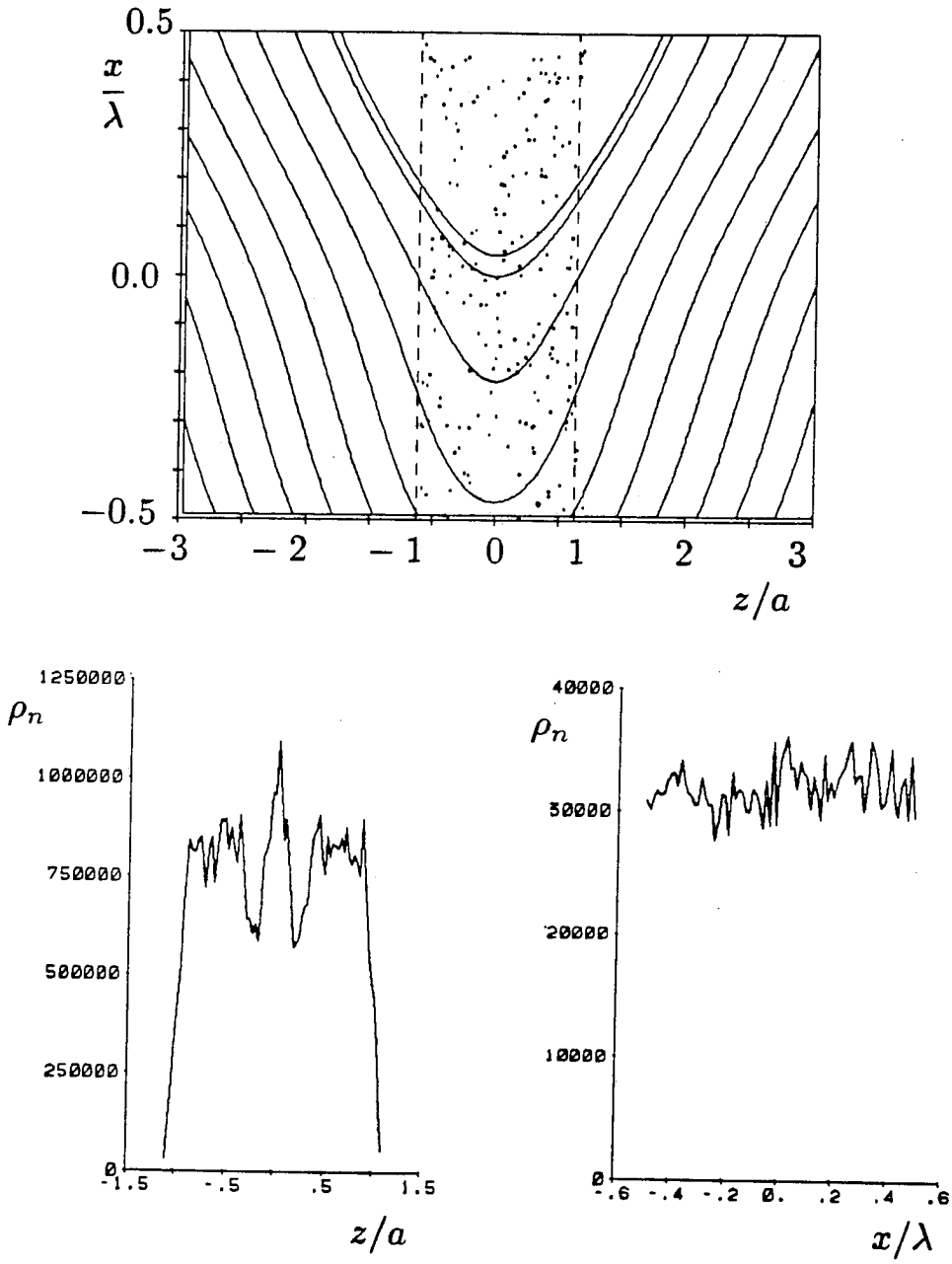

Figure 5.2: Phase space and density for the ion run. $t = 83.3$

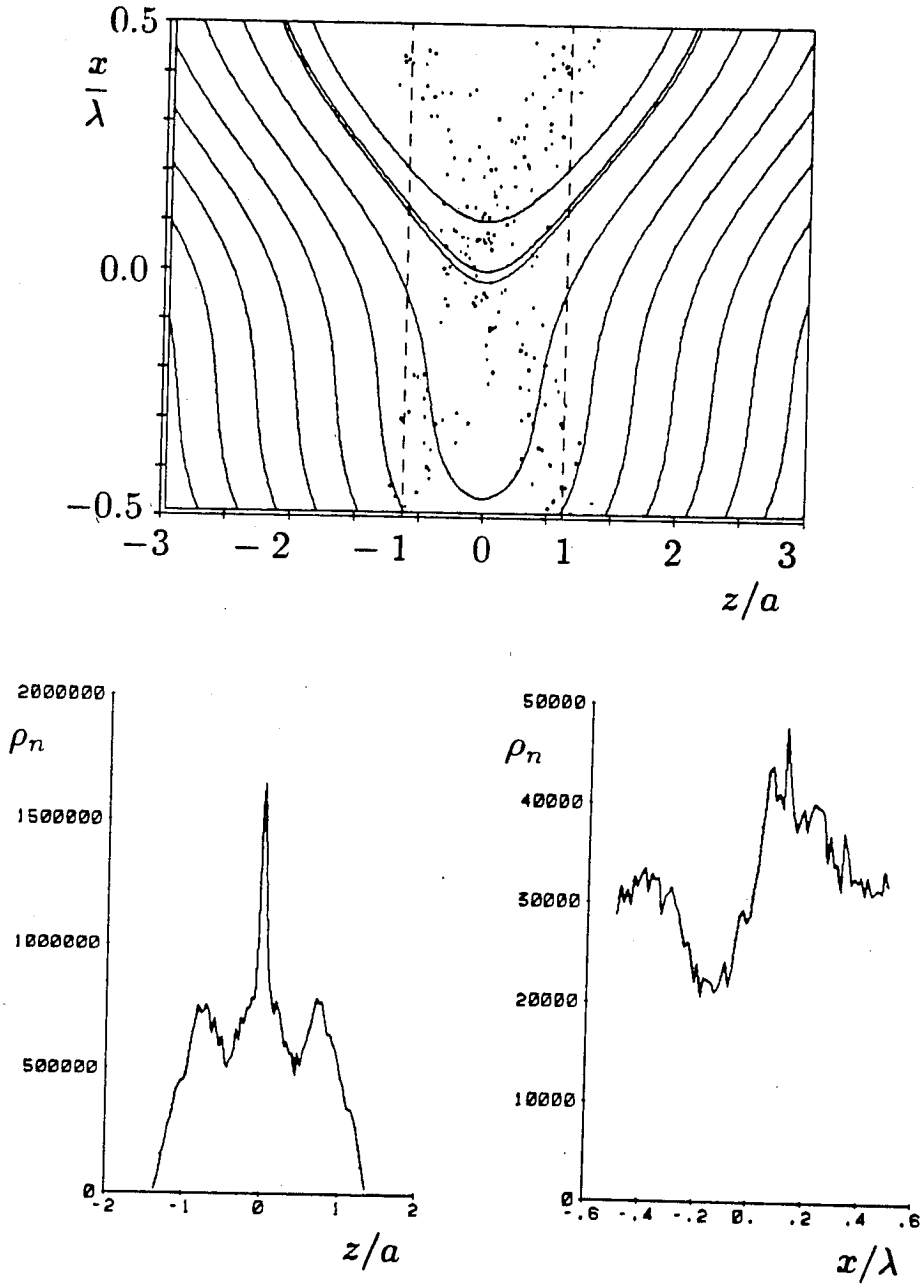

Figure 5.3: Phase space and density for the ion run. $t = 183.3$

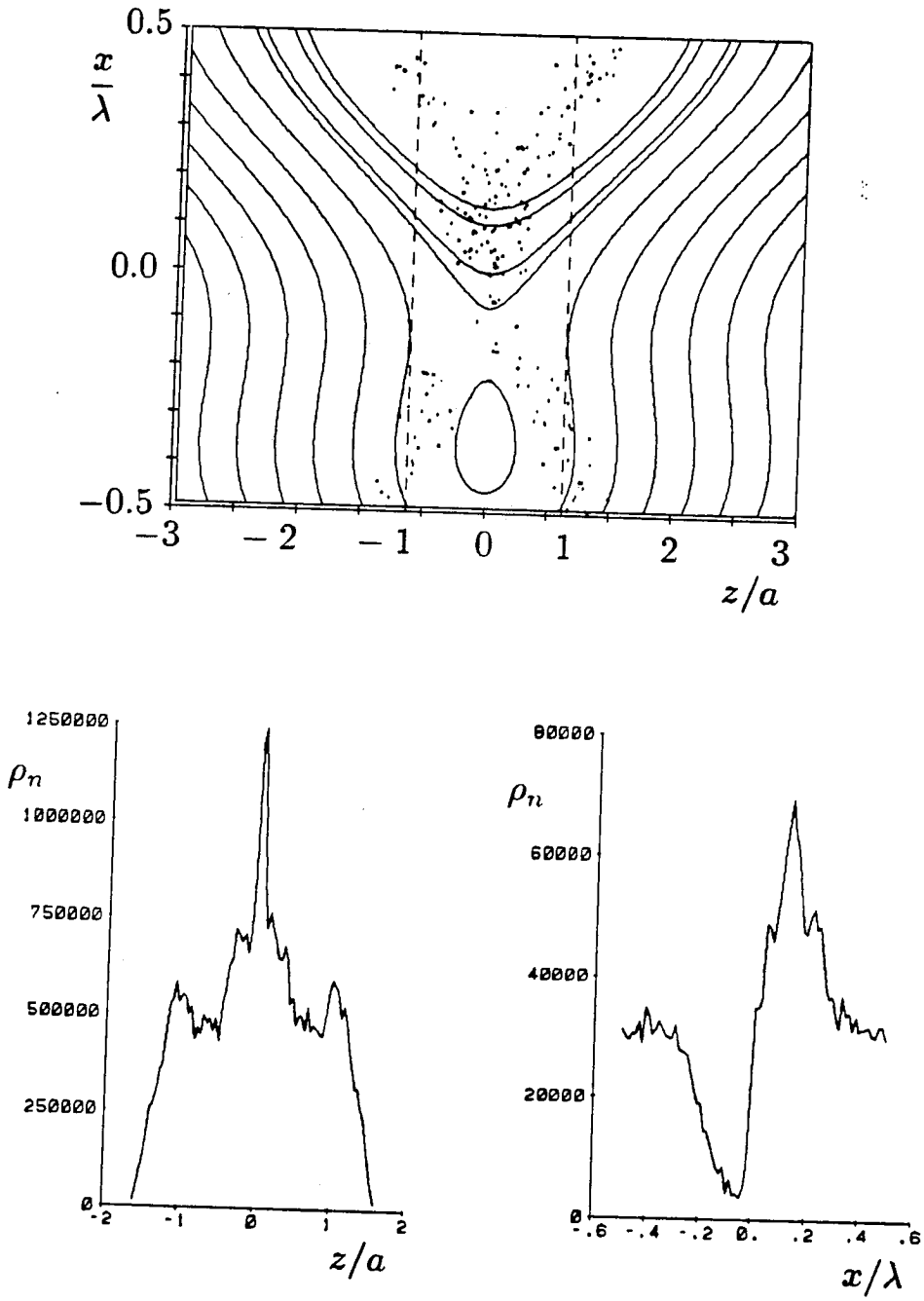

Figure 5.4: Phase space and density for the ion run. $t = 233.3$

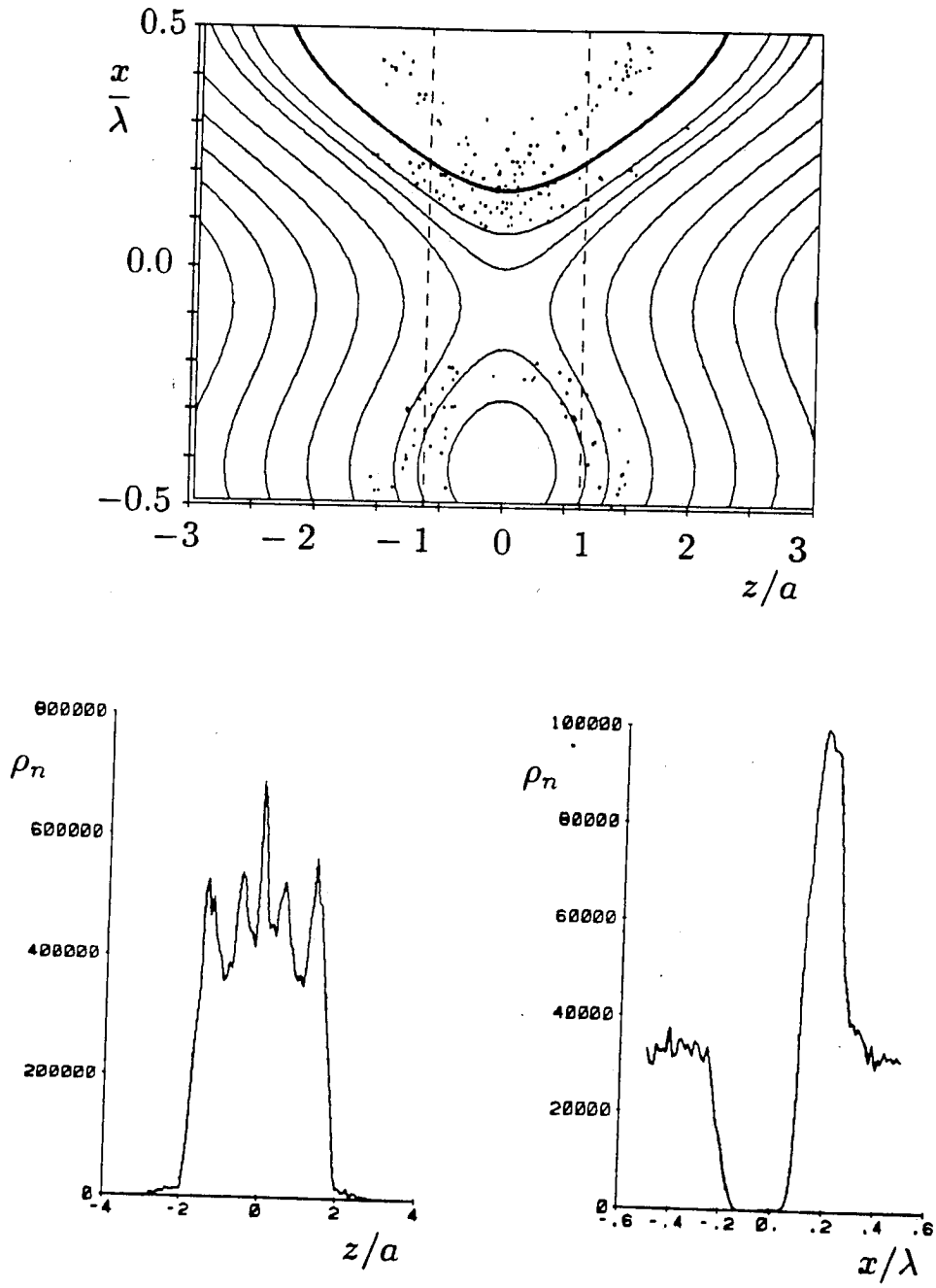

Figure 5.5: Phase space and density for the ion run. $t = 280.0$

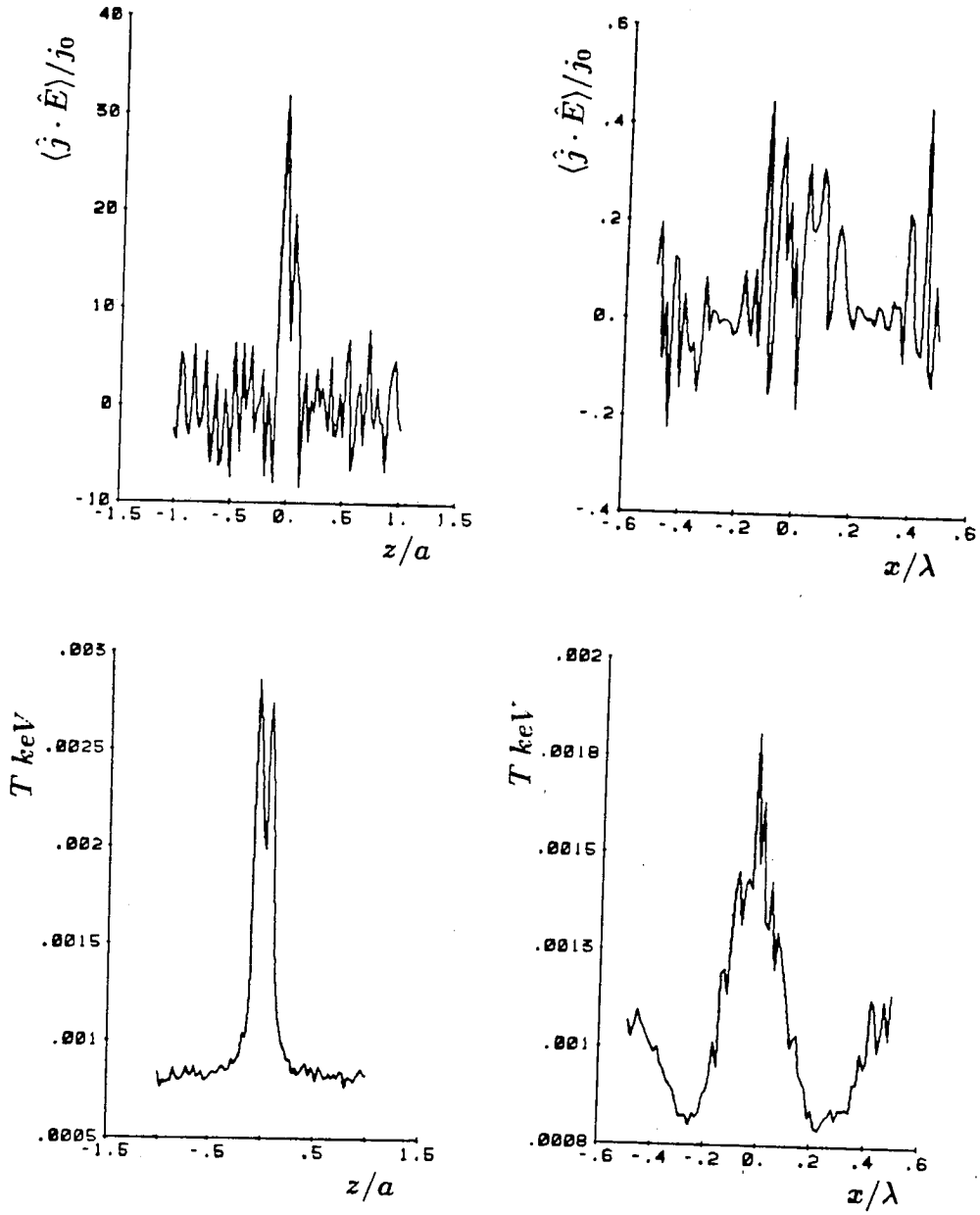

Figure 5.6: Temperature and $\langle j \cdot E \rangle$ plots for the ion run. $t = 16.7$

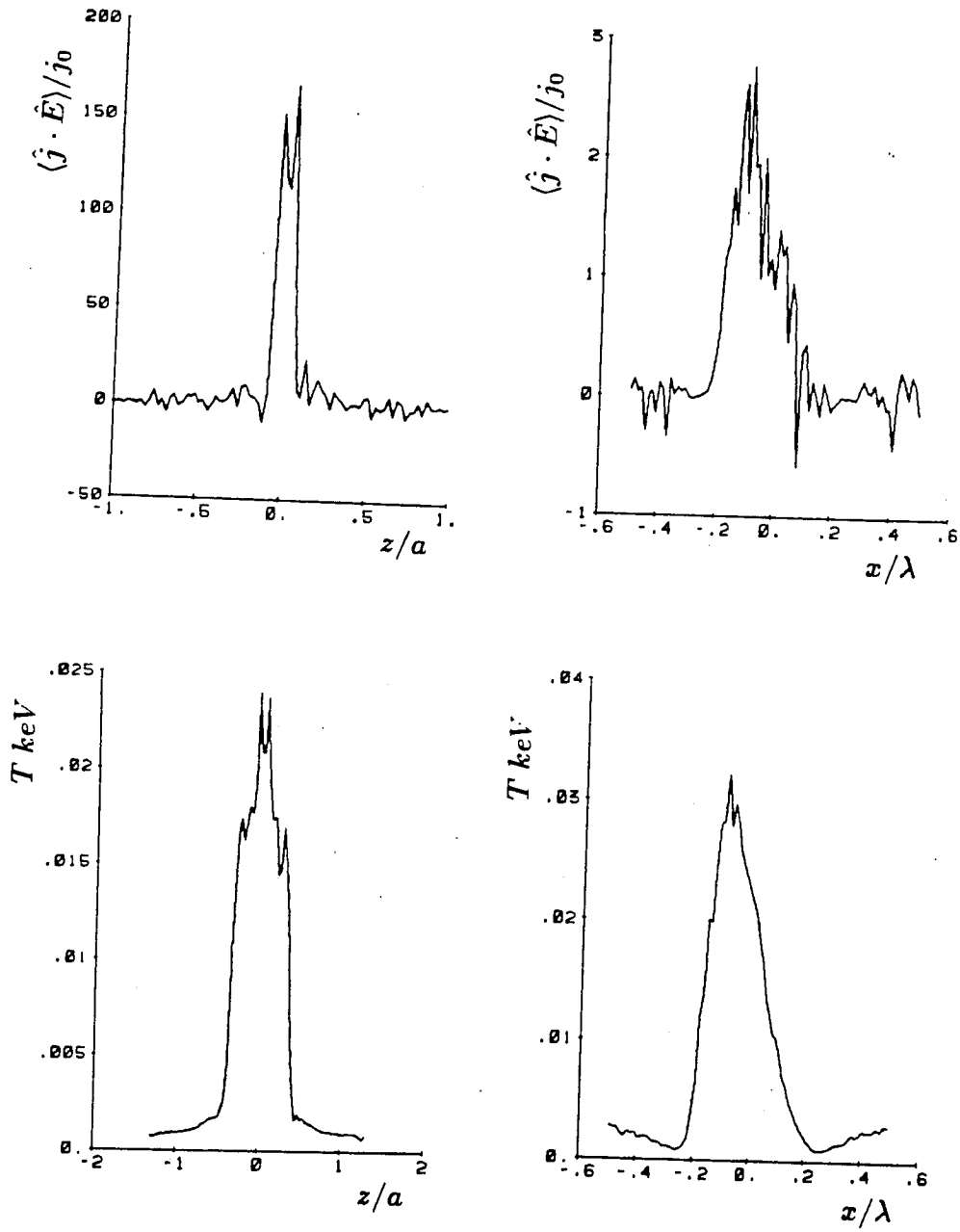

Figure 5.7: Temperature and $\langle j \cdot E \rangle$ plots for the ion run. $t = 166.7$

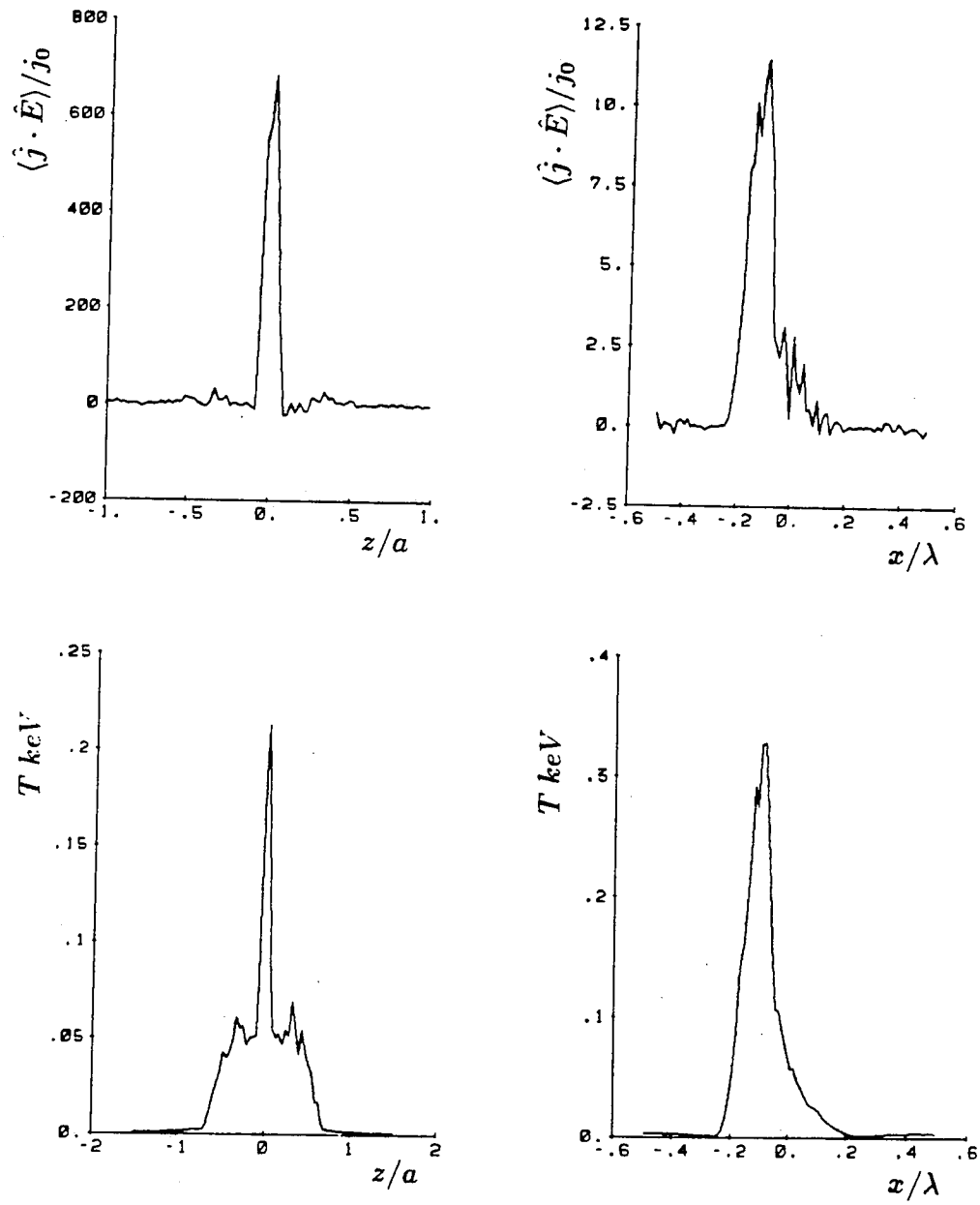

Figure 5.8: Temperature and $\langle j \cdot E \rangle$ plots for the ion run. $t = 216.7$

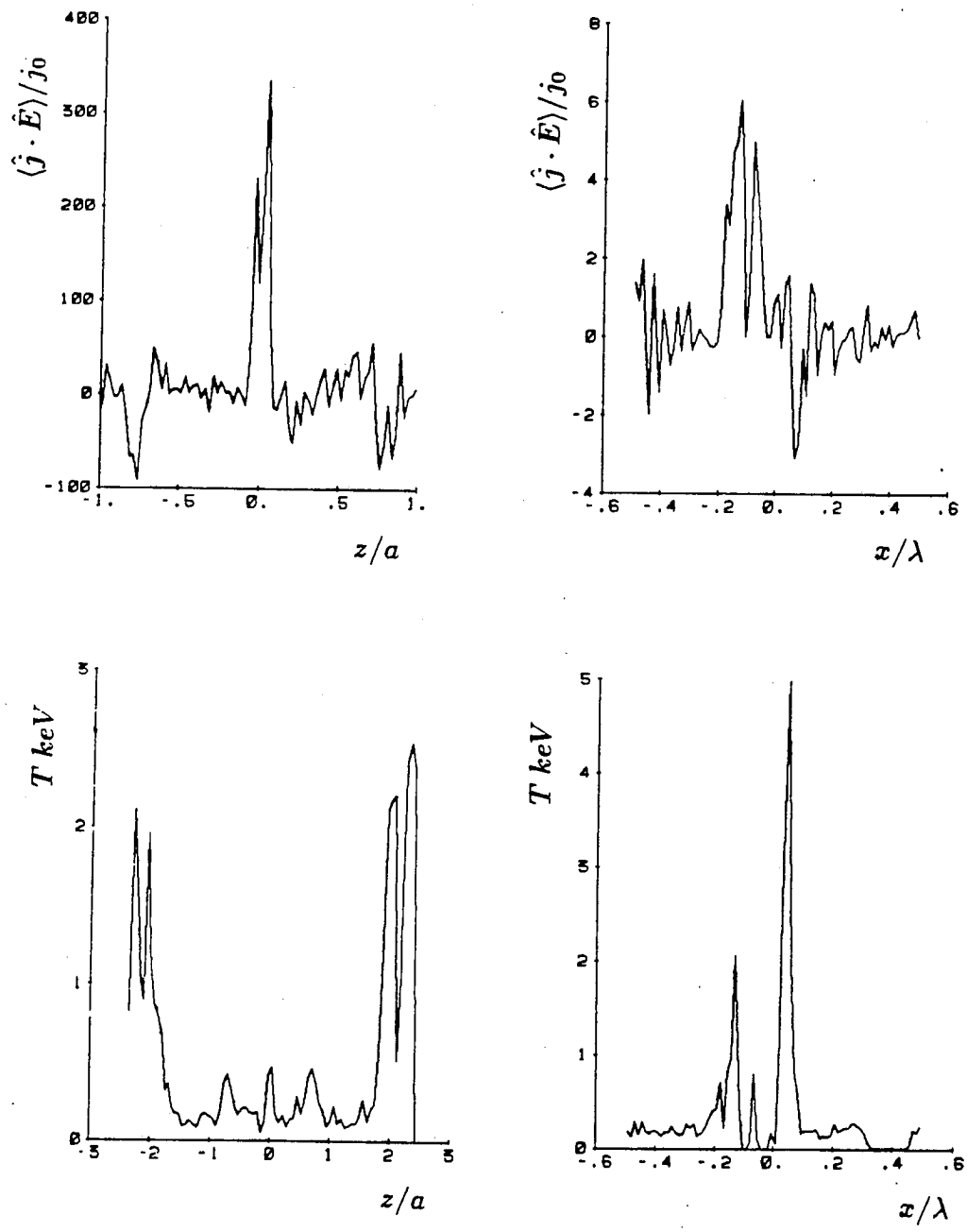

Figure 5.9: Temperature and $\langle j \cdot E \rangle$ plots for the ion run. $t = 273.3$

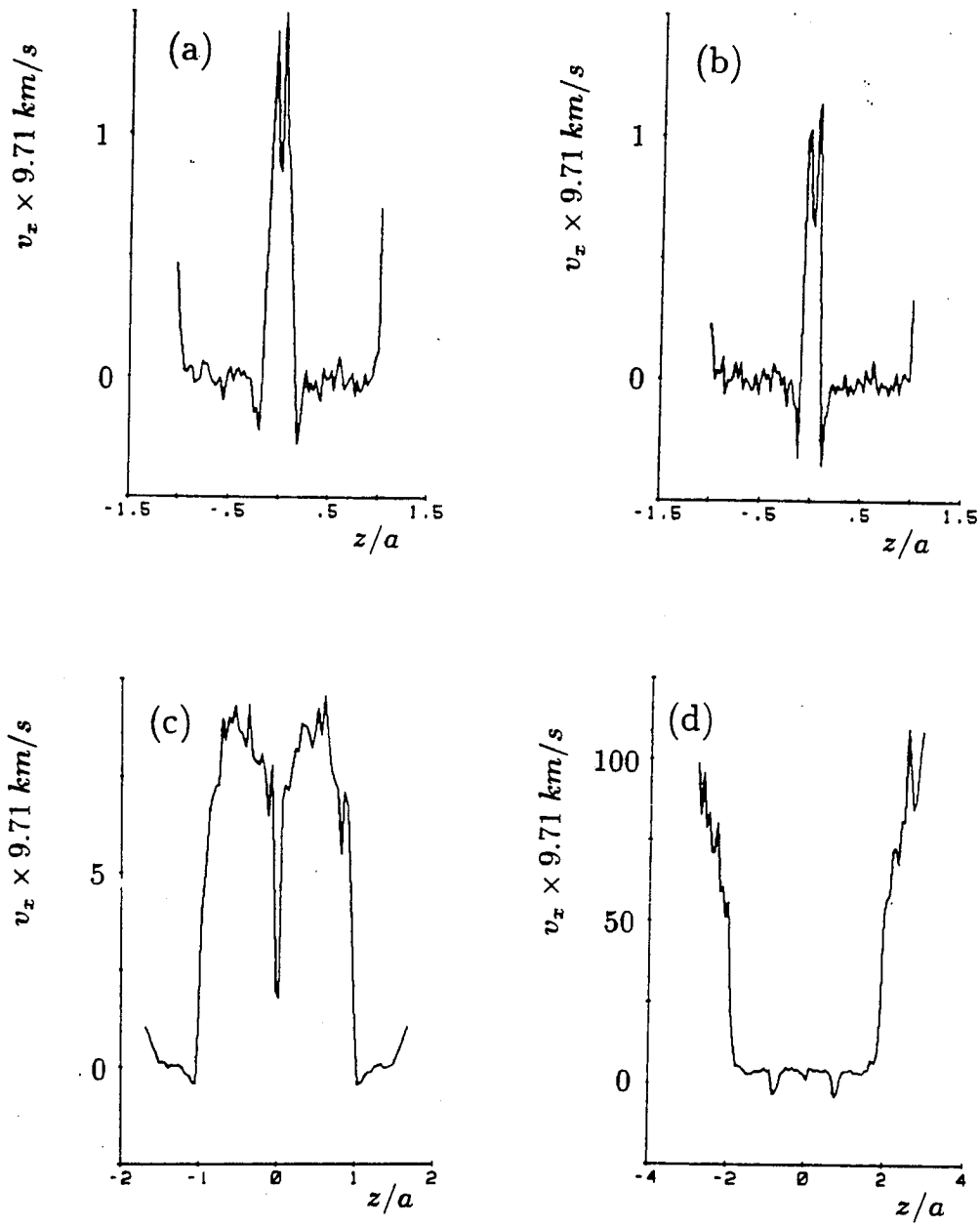

Figure 5.10: The x-velocity at different times for the ion run. **a)** $t = 33.3$, b) $t = 166.7$, c) $t = 246.7$, d) $t = 280.0$

In Figs. 5.11 and 5.12 we plot the phase space and density at times $t = 0$ and $t = 636.4\,T_{0e} = 0.35\,T_{0i}$ for the early run. The density profile has not changed in that time. In particlular, the particles are still inside the area they were placed at $t = 0$, which is between $z = \pm 0.1a$. Contrary to the density profile however, the temperature has changed considerably. In Figs. 5.13 and 5.14 we show the in-phase current $\langle j \cdot E \rangle$ and the temperature at time $t = 90.9\,T_{0e}$ (that is 90.9 electron gyroperiods after the start of the run) for both the early and the late run. The current is again flowing in a well defined channel around the reversal layer at $z = 0$. The main point here however is the tremendous temperature increase (up to three orders of magnitude) in the same narrow channel. If we keep in mind that 90.9 electron gyroperiods correspond to only 0.05 ion gyroperiods, we see that the electron temperature has risen by three orders of magnitude in only $0.05\,T_{0i} = 0.16\,sec$. This again demonstrates the system's tendency to be in the same (qualitatively) state around the time the neutral line appears. When we start with higher initial temperatures, we see in the electron runs, as we did in the ion runs, that the heating is much less severe, and the final temperature is comparable to the one we have here. In Figs. 5.15 and 5.16 we show the in-phase current $\langle j \cdot E \rangle$ and temperature for both runs at time $t = 636.4\,T_{0e}$. Notice how the current in the early run (Fig. 5.15) has decreased compared to its value at $t = 90.9\,T_{0e}$ (Fig. 5.13), while for the late run it has increased (Fig. 5.16). We will address this point in more detail later. Also notice how, after shooting up by as much as three orders of magnitude in $90.9\,T_{0e}$, the temperature has only increased by a factor of two to five in the remaining $545.5\,T_{0e}$. The temperature for the late run is also higher than that of the early run, as is to be expected since the current is higher too.

We finally need to discuss the time history of the height-integrated

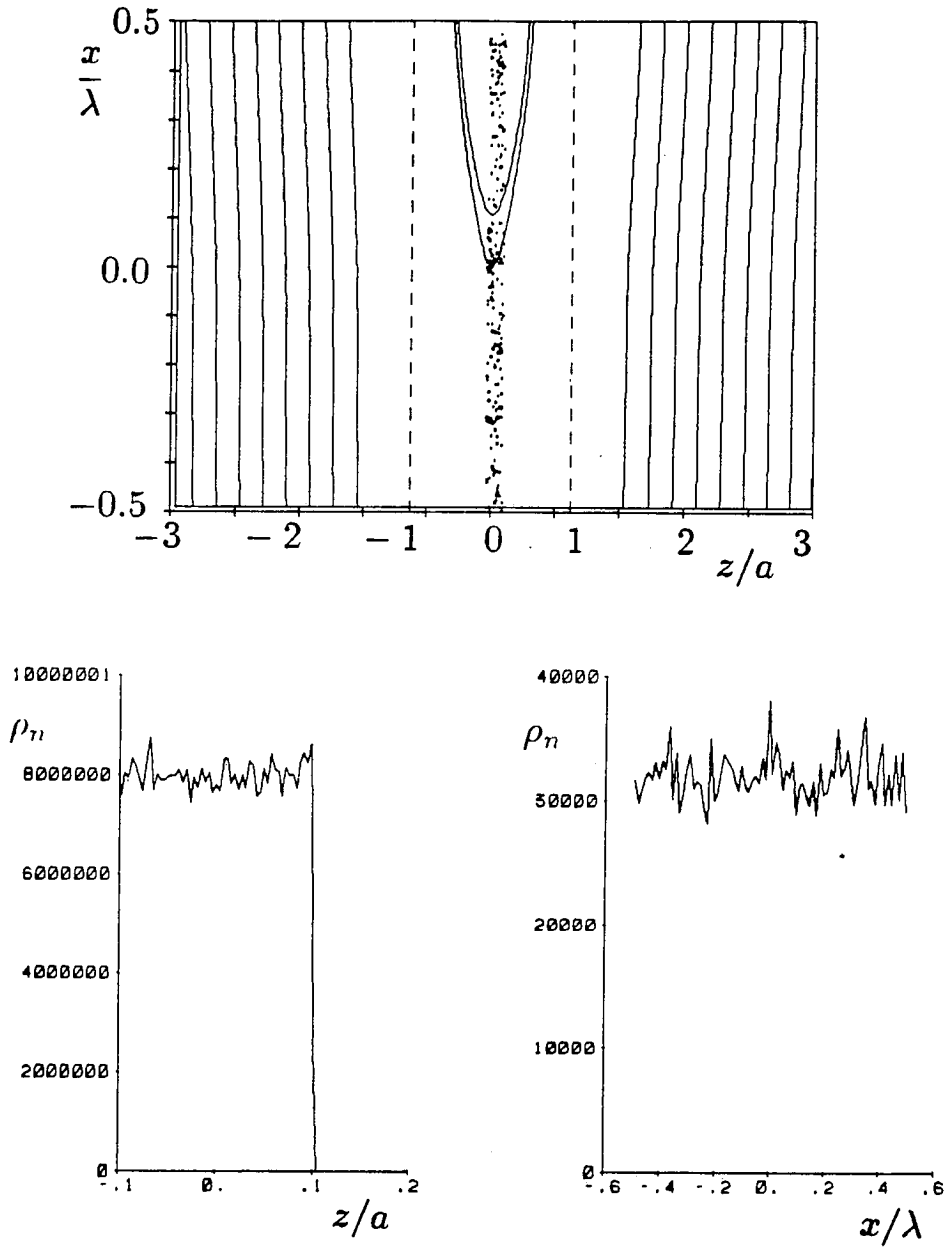

Figure 5.11: Phase space and density plot for the early electron run. $t = 0$.

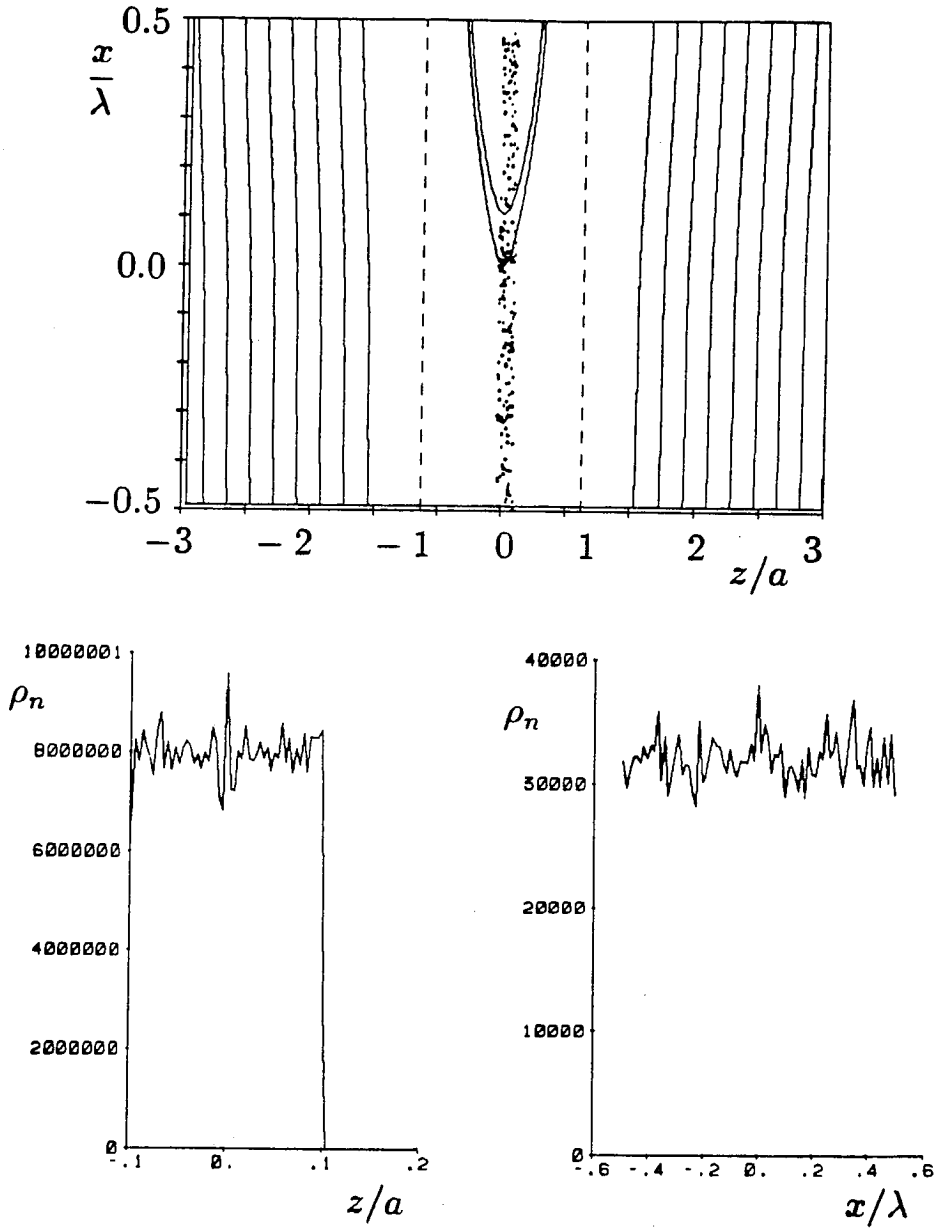

Figure 5.12: Phase space and density plot for the early electron run. $t = 636.4\,T_{0e}$.

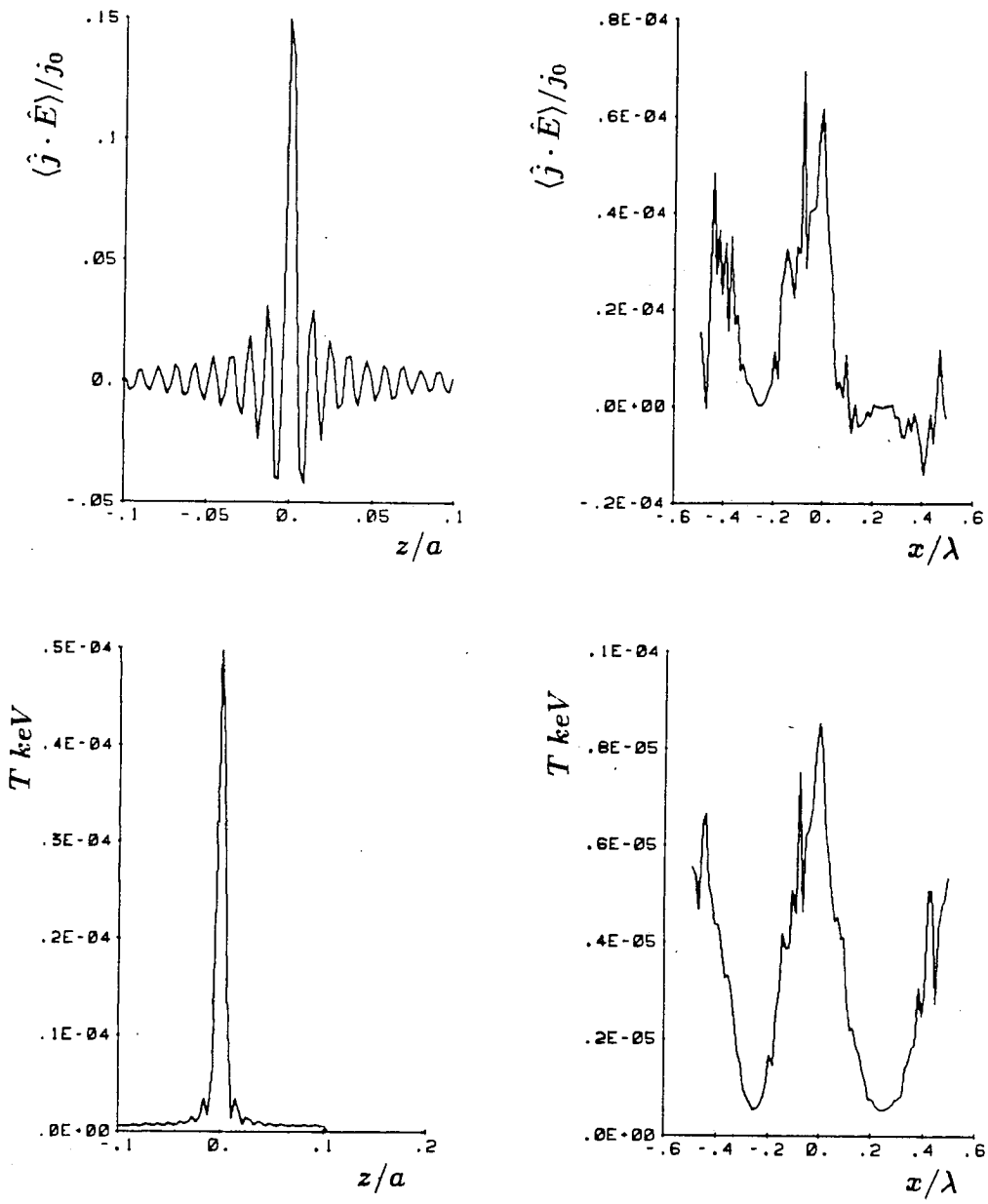

Figure 5.13: Current and temperature plots for the early electron run. $t = 90.9\,T_{0e}$.

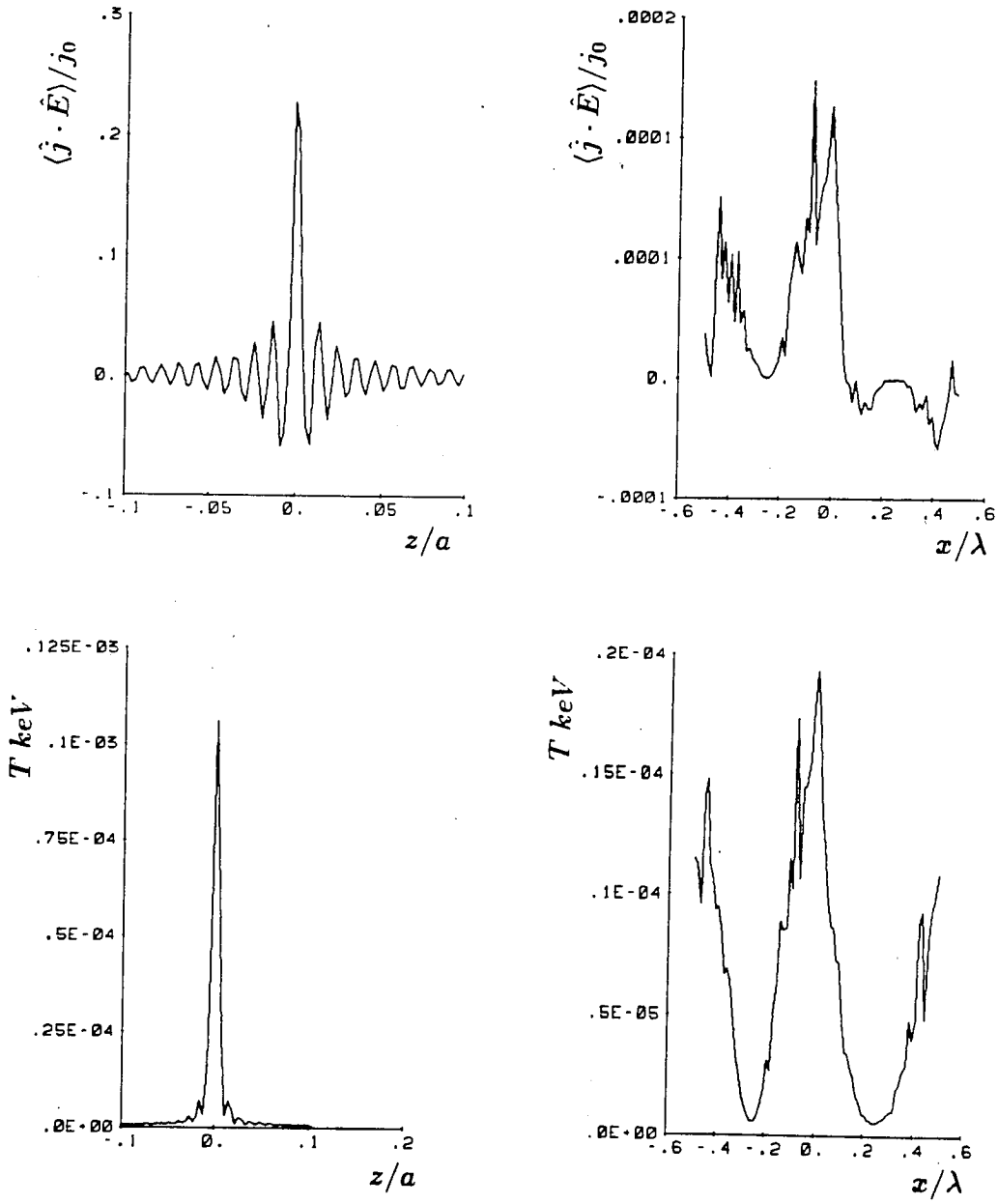

Figure 5.14: Current and temperature plots for the late electron run. $t = 90.9\, T_{0e}$.

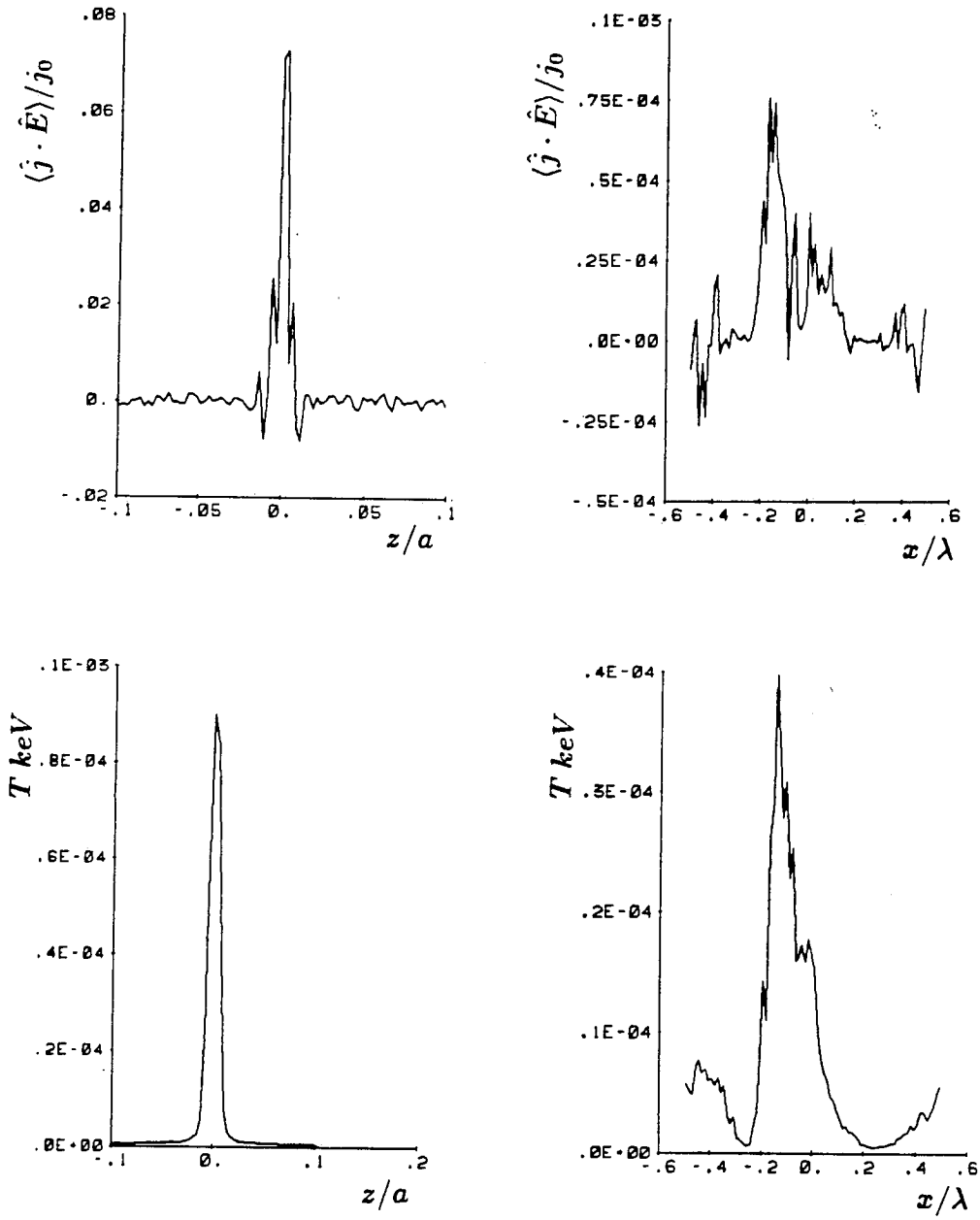

Figure 5.15: Current and temperature plots for the early electron run. $t = 636.4\, T_{0e}$.

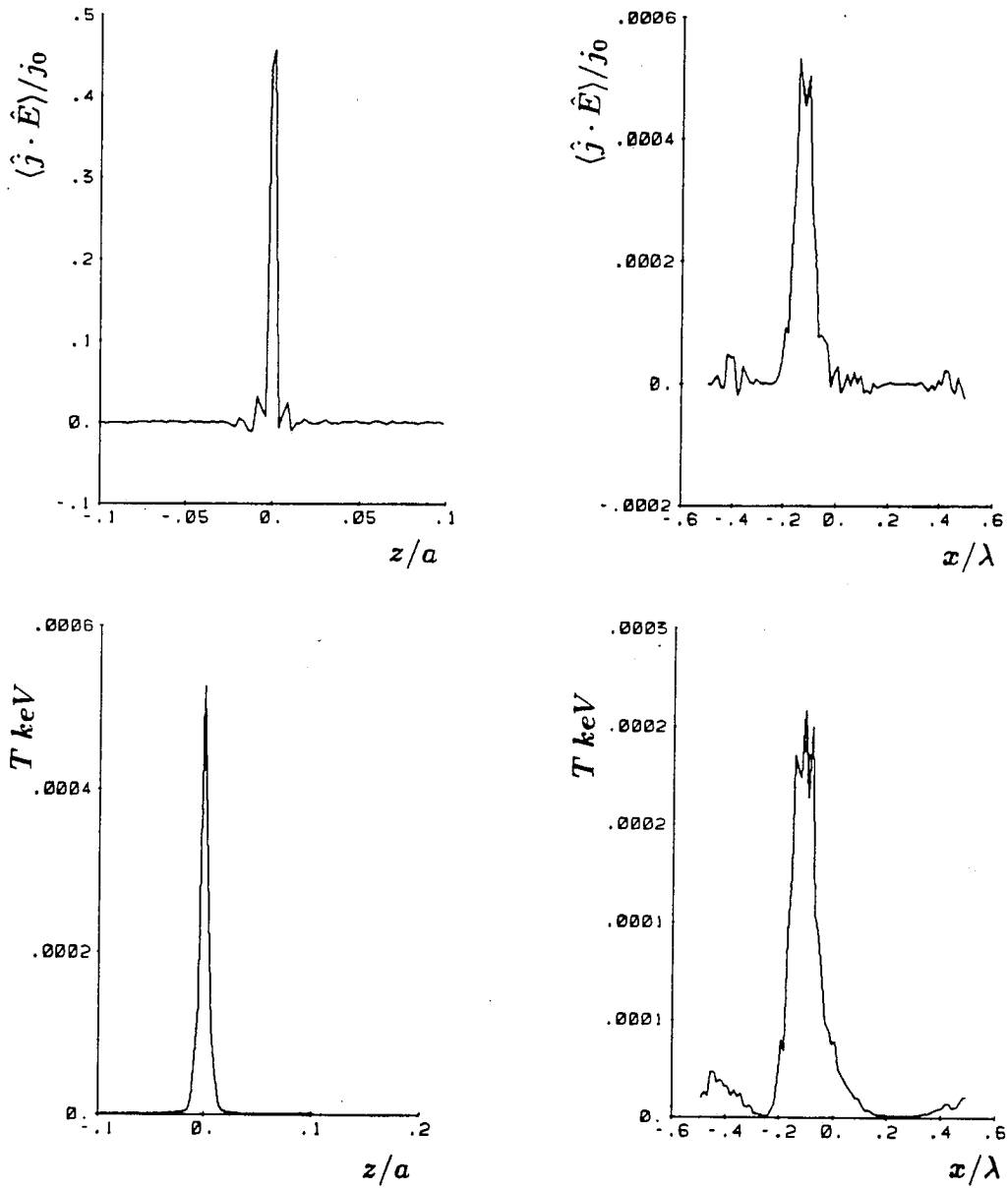

Figure 5.16: Current and temperature plots for the late electron run. $t = 636.4\, T_{0e}$.

in-phase current given by

$$\int_{-\Delta z/2}^{\Delta z/2}\int_{-\lambda/2}^{\lambda/2} j_y \cos(kx)\, dx\, dz = \int_{-\Delta z/2}^{\Delta z/2} \langle j_y \cos(kx)\rangle\, dz. \tag{5.10}$$

Keeping in mind that $E_y = (B_0\psi_0\gamma/c)e^{\gamma t}\cos(kx)$ and that the in-phase current flows in a narrow channel of width (Δz) around the reversal layer at $z = 0$, we can rewrite Eq. 3.11 as

$$\overline{\langle j \cdot E\rangle} = \int_{-a}^{a} \langle j \cdot E\rangle\, dz = \frac{\rho_n e^2}{2m}\left(B_0\psi_0\frac{\gamma}{c}e^{\gamma t}\right)^2 (\Delta z)\tau \tag{5.11}$$

In the code the hight-integrate $\langle j \cdot E\rangle$ is given by

$$\begin{aligned}\overline{\langle j \cdot E\rangle} &= (e\rho_n v_0)\left(B_0\psi_0\frac{\gamma}{c}e^{\gamma t}\right)\left(\frac{1}{N}\sum_{i=1}^{N}\hat{j}_y^i\cos(2\pi\hat{x}^i)\right)\\ &= (e\rho_n v_0)\left(B_0\psi_0\frac{\gamma}{c}e^{\gamma t}\right)\overline{\langle \hat{j}\cdot\hat{E}\rangle}\end{aligned} \tag{5.12}$$

where the bar denotes the integration over z and the hat denotes the dimensionless quantities used in the code. Notice that, unlike Eq. 5.8, the sum is now over all particles, since we have integrated in z as well as in x. Solving equations 5.11 and 5.12 for $\overline{\langle \hat{j}\cdot\hat{E}\rangle}$ we find

$$\overline{\langle \hat{j}\cdot\hat{E}\rangle} = \frac{\omega_0}{2v_0}\psi_0\gamma e^{\gamma t}(\Delta z)\tau. \tag{5.13}$$

In Fig. 5.17 we plot $\overline{\langle \hat{j}\cdot\hat{E}\rangle}$ against time for the ion run. If we calculate the value of $\overline{\langle \hat{j}\cdot\hat{E}\rangle}$ from Eq. 5.13 with

$$\tau = \frac{\pi}{kv}$$

where v is the thermal speed, the values of $\overline{\langle \hat{j}\cdot\hat{E}\rangle}$ we get are too big by almost two orders of magnitude. Moreover, since the temperature increases dramatically with time, $1/kv$ gives the wrong scaling, decreasing rather than increasing with time. If on the other hand we use $\tau = \pi/(b\omega_0)$ in Eq. 5.13, and if we also

require that b in the expression for τ is the root-mean-square average of b in the current channel, so that

$$\tau = \frac{\pi}{\omega_0 b_{rms}}$$

with

$$b_{rms}^2 = \frac{1}{x_2 - x_1} \int_{x_1}^{x_2} \left(b + \psi_0 k e^{\gamma t} \sin(kx)\right)^2 \, dx$$

where x_1 and x_2 are the limits in x of the current channel (eg. $x_1 = -\lambda/4$, $x_2 = 0$ in the ion run we are considering), then $\overline{\langle \hat{j} \cdot \hat{E} \rangle}$ has the right scaling, although it is still rising much more slowly than the numerical value (see Fig. 5.17; the dots give the theoretical values of $\overline{\langle \hat{j} \cdot \hat{E} \rangle}$).

For the early electron run, the value of $\overline{\langle \hat{j} \cdot \hat{E} \rangle}$ is plotted against time in Fig. 5.18, and for the late run in Fig. 5.19. Because of the similarity of the plots in the begining, it it fair to assume that during that time the system is reaching its 'preferred stated', while after the initial 'equilibration' we can see the real response of the system. Notice how, in the early run, $\overline{\langle \hat{j} \cdot \hat{E} \rangle}$ reaches a constant value (except for small oscillations), while in the late run it increases almost linearly in time. Since the only difference in the two runs is the existence of the neutral line in the late run, we see that the appearance of the neutral line causes the value of the height-integrate $\langle j \cdot E \rangle$ to increase rapidly with time, and since $\overline{\langle j \cdot E \rangle} \sim \tau$ and $\gamma \sim 1/\tau$, it causes the tearing mode growth rate to decrease. This feature was common to all four of the electron runs, although it does not seem to be true for the ions. Looking at fig. 5.17 we see that $\overline{\langle \hat{j} \cdot \hat{E} \rangle}$ for the ions starts increasing long before the neutral line appears at $t = 207.4\, T_{oi}$. When we calculate $\overline{\langle \hat{j} \cdot \hat{E} \rangle}$ for the electron run using the theoretical values for τ, we see that both expressions underestimate the value of $\overline{\langle \hat{j} \cdot \hat{E} \rangle}$ by approximately two orders of magnitude, although $\tau = \pi/\omega_0 b_{rms}$ has again the right scaling for the early run, while $\tau = \pi/kv$ does not. Since the electron

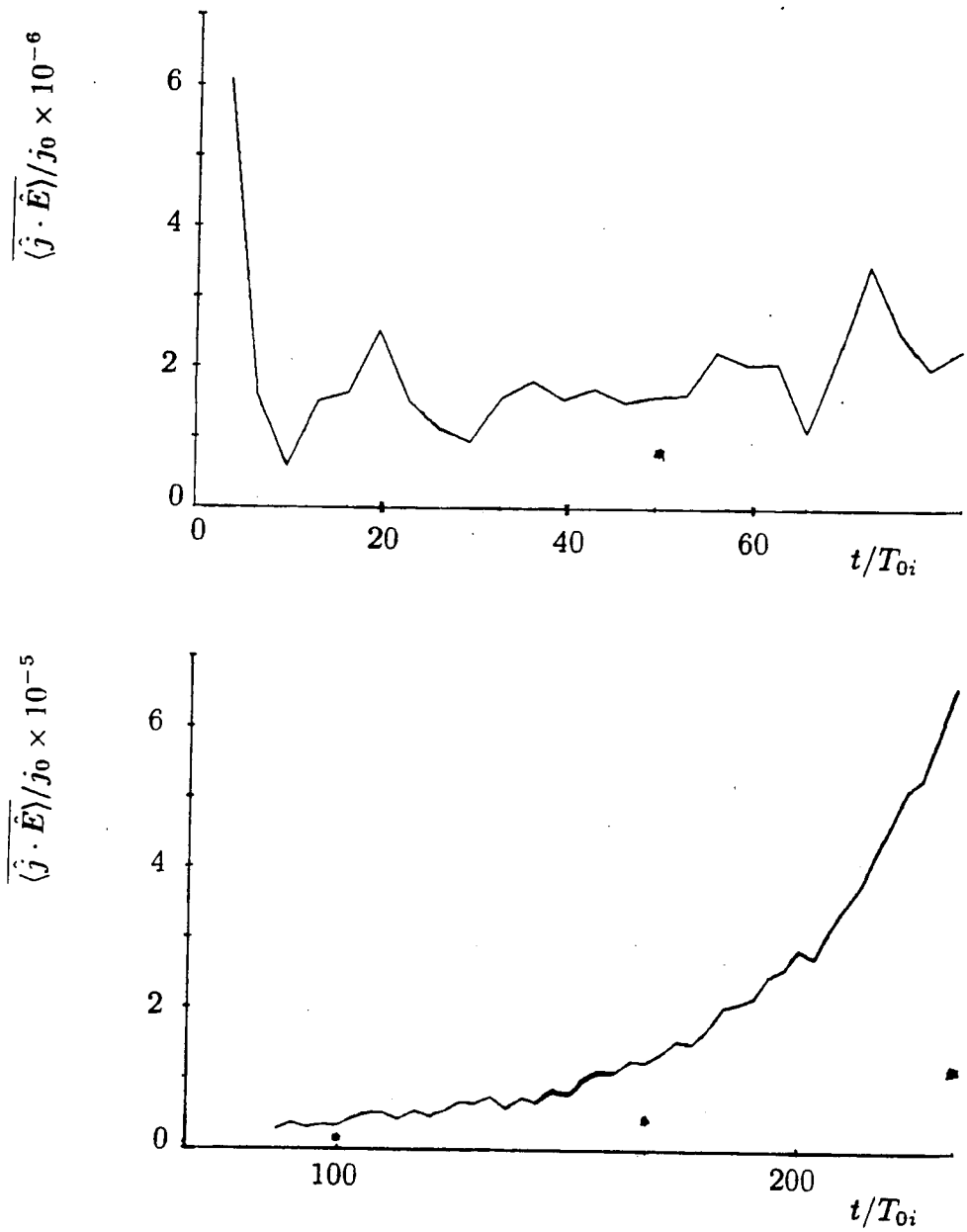

Figure 5.17: $\overline{\langle \hat{j} \cdot \hat{E} \rangle}$ plotted against time for the ion run.

gyroperiod is 1836 time smaller than the ion gyroperiod, the value of $e^{\gamma t}$ changes very little over the course of an electron run so that b_{rms}, and therefore $\overline{\langle \hat{j} \cdot \hat{E} \rangle}$ is almost constant, in agreement with the results of the simulation. In contrast v increases rapidly over the course of the run, so that π/kv decreases.

We therefore see that even the simple system we are studying here appears to give correctly a lot of the qualitative features of the magnetotail, with the final ion temperature and earthward drift in the PSBL in good quantitative agreement with the observed values. Also the neutral line is seen to play an important role in the development of the electron tearing mode, with the growth rate rapidly decreasing after its appearance, and although $\tau = \pi/\omega_0 b_{rms}$ gives the wrong value for the hight-integrate $\langle j \cdot E \rangle$, it has the correct scaling with time, contrary to $\tau = \pi/kv$ which always decreases in time. Finally the system seems to always end up in the neighborhood of the same state at around the time the neutral line appears, and the further from that state it is when we start the simulation, the faster it will converge to it. This state appears to be characterised by $\kappa \approx 1$. Runs that are otherwise similar, can end up with final temperatures differing by more than an order of magnitude, while their κ's only differ by 20%–30%. The value of κ is drastically reduced in a very short time (one particular run went from $\kappa \approx 40$ to $\kappa \approx 0.6$ in less than $0.05\, T_{0i} = 0.16\, sec$) and then remains more or less unchanged, with $\kappa \lesssim 1$. All final κ's in our runs range between 0.6 and 0.9. Also, since this is a test particle code and the particles have no mechanism by which to lose energy, the temperature can only increase and κ can therefore only decrease. A run that is started with a low initial temperature and low initial κ will experience mild heating, while an otherwise similar run with a high initial κ will undergo much more severe heating. There is therefore considerable evidence that κ is the parameter that determines the state of the system around the time of the

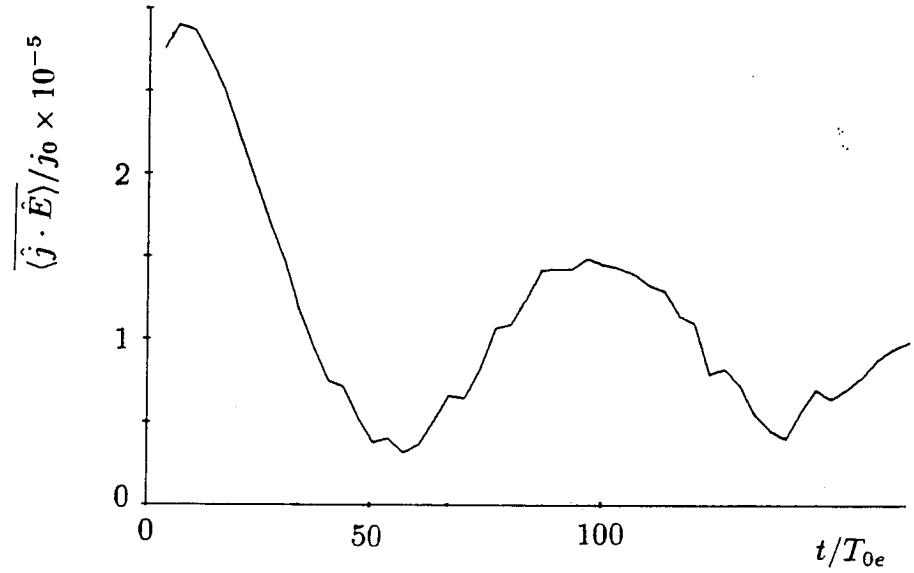

Figure 5.18: $\overline{\langle \hat{j} \cdot \hat{E} \rangle}$ plotted against time for the early electron run.

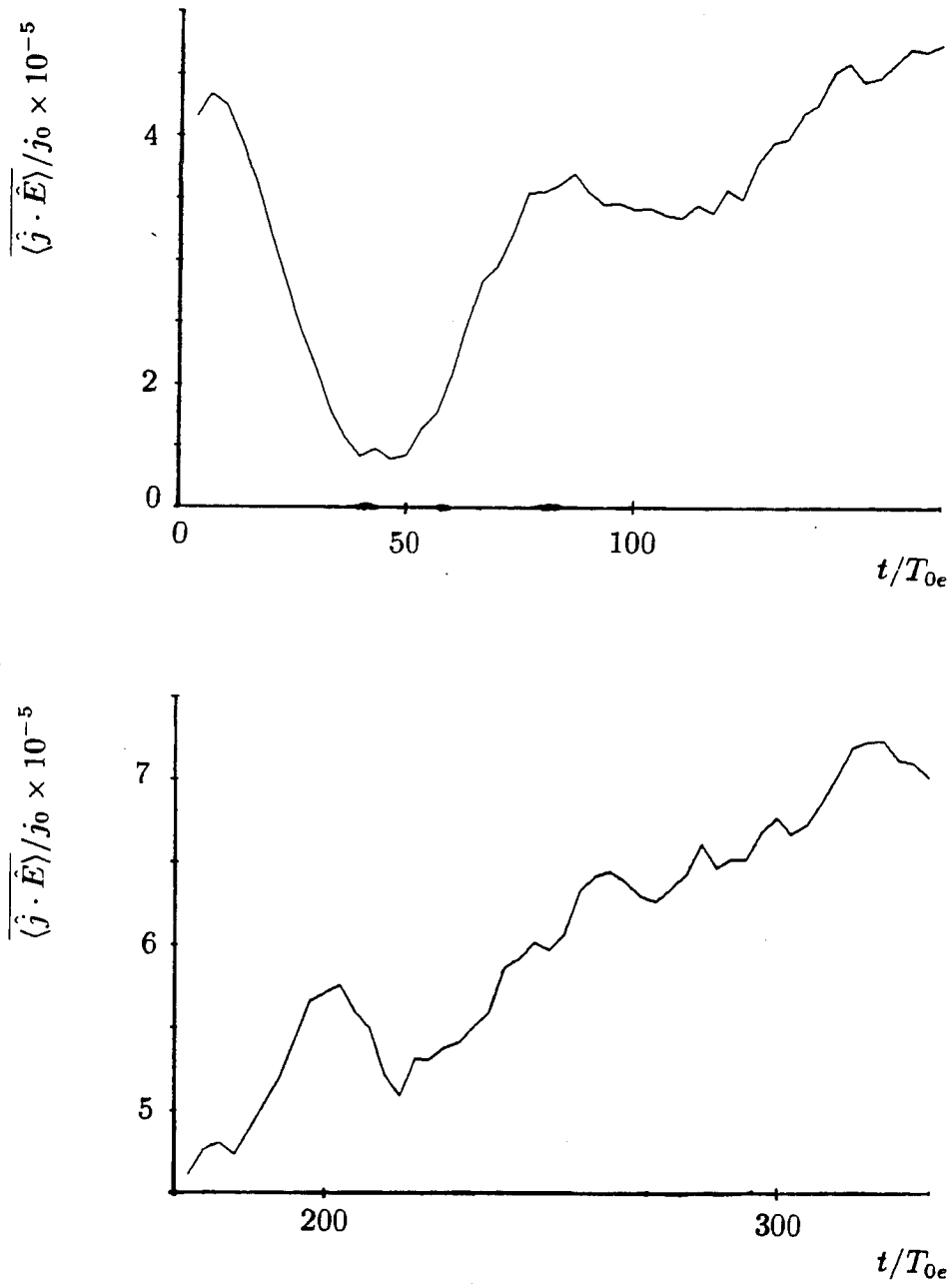

Figure 5.19: $\overline{\langle \hat{j} \cdot \hat{E} \rangle}$ plotted against time for the late electron run.

appearance of the neutral line. At this point however a cautionary note needs to be made. Since $\kappa \sim \mathcal{E}^{-1/4}$, where $\mathcal{E}$ is the particle energy, a small difference in κ can account for a large difference in temperature. This fact, coupled with the qualitative nature of the 'preferred state' makes it difficult to obtain numerical results that prove that κ (rather than the temperature) is the determining parameter, although intuition would suggest that this is indeed the case.

Chapter 6

CONCLUSIONS

In the present work we have studied two well known but distinct problems of plasma theory: anomalous transport from $\vec{E} \times \vec{B}$ drift motion and collisionless reconnection. Both problems were modeled by simple, low degree of freedom hamiltonian systems. Even though the two physical problems are quite different, the hamiltonian systems used to model them and the mathematical techniques used to study them are remarkably similar. Indeed, even the analytical forms of some of the solutions, for instance the expression in Eq. 2.28 for the change in energy and the expression in Eq. 4.11 for the change in the magnetic moment, are almost identical. On a more fundamental level, the detailed dynamical mechanism by which transport is achieved is the same in both systems.

In Part I we describe one-wave $\vec{E} \times \vec{B}$ motion in a slab geometry, by a hamiltonian with a phase space composed of an infinite square lattice of counterrotating rolls, separated by a separatrix. No transport across the separatrix is possible in this configuration unless collisions are present. If however we add a small amount of a second wave to the hamiltonian, the hamiltonian becomes time dependent, the energy of a single particle is no longer conserved, and a particle can therefore wander throughout phase space sampling all possible energy values. When we calculate the total change in the energy of a particle

that moves close to the separatrix from the vicinity of one X-point to the next, we find that almost all of the energy change ΔH is imparted to the particle during a short interaction time around the midpoint of the particle's trajectory. The particle motion is therefore mostly regular, except for small 'kicks' the particle receives every quarter period of its oscillation around the O-point. The magnitude of these kicks has been calculated for two limiting cases. If the frequency of the perturbation Ω is low enough, ΔH is algebraically small in Ω. If Ω is sufficiently large, ΔH is exponentially small in Ω^2. In both cases however, the magnitude of ΔH also depends on the relative phase of the two oscillations (around the O-point and around the time torus). This sensitive dependence on the relative phase is the cause of the system's chaotic behavior. It also enables us to express the motion of a particle close to the separatrix by the standard map, and apply to our system the considerable knowledge accumulated in recent years about the standard map.

In Part II we study collisionless magnetic reconnection in the context of a reversed field, modelling the geomagnetic tail (which is topologically equivalent to one-half of a long FRC). The tearing instability, which is responsible for magnetic reconnection, requires some form of dissipation. In resistive MHD theory that dissipation is provided by coulomb collisions. In the collisionless regime this role is performed by stochastic changes in the value of the particles magnetic moment μ. The magnetic moment of a particle is adiabatically conserved when the particle is in the strong field region, far from the reversal layer. As the particle moves from one mirroring point, across the neutral layer, to its next mirroring point in the high field region, the magnetic moment changes. The magnitude of that change, $\Delta\mu$, is calculated for $\kappa \gg 1$ (where κ is the frequency of the x-oscillation in the reduced hamiltonian $h = \dot{x}^2 + \dot{z}^2 + (z^2/2 + \kappa x)^2$ that describes the system) and it is found to be exponentially small in κ^2 and

to depend on the phase of the gyromotion at the time of the layer crossing. Furthermore, most of the contribution to $\Delta\mu$ comes from a short interaction time around the reversal layer. We therefore see that once again the particle motion is mostly regular, except for small 'kicks' the particle receives every half bounce period. These 'kicks' in the particle magnetic moment can be exploited to provide the dissipation that the coulomb collisions provide in the collisional case, in the same way that the 'kicks' in the particle energy in Part I can be used to provide the transport that the collisions provide in the collisional case.

Finally we use a test particle code to study the time evolution of ensembles of particles placed in our model fields. We find that our simple model gives correctly a lot of the qualitative features of the geomagnetic tail, with the ion temperature and earthward drift in the PSBL in good quantitative agreement with observed values as well. The height-integrated in-phase current $\langle j \cdot E \rangle$ rises faster after the appearance of the neutral line and, for $\kappa < 1$, seems to be best described by the decorrelation time $\tau = \pi/\omega_0 b_{rms}$, although even that does not rise as fast as the simulation value of $\langle j \cdot E \rangle$. This discrepancy may be partly expained by the fact that this is a test particle code and there is no mechanism by which the particles can feed their energy back to the waves, and as a result the current grows faster than if the particles could shed some of their energy. Finally the system seems to always tend to the same (qualitatively) state around the time the neutral line appers, a state that appears to be characterised by a kappa value close to one.

Appendix A

Calculation of ΔH for $\Omega < s$.

The change in the value of the hamiltonian as the particle moves from the vicinity of one X-point to the next is given by

$$\Delta H = \epsilon\Omega \sin(kn\pi + \alpha) A_s(\Omega) \sin\beta \tag{A.1}$$

where

$$A_s(\Omega) = \int_{-\infty}^{\infty} \cos(sy' - \Omega\tau)\, d\tau \tag{A.2}$$

with

$$y' = 2\tan^{-1}(e^{\tau}) - \frac{\pi}{2}\,. \tag{A.3}$$

We can rewrite Eq. A.2 as

$$A_s(\Omega) = \mathrm{Re}\int_{-\infty}^{\infty} e^{isy' - i\Omega\tau}\, d\tau = \mathrm{Re}\left[e^{-is\pi/2}\int_{-\infty}^{\infty} e^{isy - i\Omega\tau}\, d\tau\right] \tag{A.4}$$

with

$$y = 2\tan^{-1}(e^{\tau})\,. \tag{A.5}$$

We can calculate the integral in Eq. A.4 by the method of steepest descent. From Arfken (1970)

$$\int e^{f(z)}\, dz \approx \sqrt{2\pi}\frac{e^{f(z_s)}e^{i\alpha_s}}{|f''(z_s)|^{1/2}} \tag{A.6}$$

where z_s is the saddle point and α_s the direction along which we cross the saddle point. In our case

$$f(\tau) = isy - i\Omega\tau\,. \tag{A.7}$$

From Eq. A.5 we see that

$$\tau = \ln\left[\tan\left(\frac{y}{2}\right)\right] \quad \text{and} \quad \dot{y} = \sin y \tag{A.8}$$

so that

$$\begin{aligned} f'(\tau) &= is\sin y - i\Omega \\ f''(\tau) &= is\sin y\cos y\,. \end{aligned} \tag{A.9}$$

The saddle point is given by $f' = 0$, so that

$$\sin y_s = \frac{\Omega}{s} = R \tag{A.10}$$

where the subscript s stands for saddle point and is not to be confused with the parameter s. If we now put $y = \xi + \pi/2$ we get from Eq. A.10

$$\cos\xi_s = R \Rightarrow \xi_s = \pm\cos^{-1}R \Rightarrow y_{s\pm} = \frac{\pi}{2} \pm \cos^{-1}R\,. \tag{A.11}$$

Substituting this into A.9 and A.5 we obtain

$$f''(\tau_{s\pm}) = is\sin y_s\cos y_s = \mp i\Omega\sqrt{1-R^2} \tag{A.12}$$

and

$$\tan\left(\frac{y_{s\pm}}{2}\right) = \frac{sin y_{s\pm}}{1+\cos y_{s\pm}} = \frac{R}{1\mp\sqrt{1-R^2}} \tag{A.13}$$

so that

$$\tau_{s\pm} = \ln\left[\tan\left(\frac{y_{s\pm}}{2}\right)\right] = \ln\left[\frac{R}{1\mp\sqrt{1-R^2}}\right]\,. \tag{A.14}$$

If we Taylor expand f around the saddle point we get

$$f_{(\tau)} = f_{(\tau_s)} + \frac{1}{2}f''_{(\tau_s)}(\tau-\tau_s)^2$$

since $f'(\tau_s) = 0$. If we now put $\tau = \tau_s + \delta e^{i\alpha}$, the second order term in the Taylor expansion becomes

$$B = \frac{1}{2}f''_{(\tau_s)}(\tau-\tau_s)^2 = \mp i\frac{\Omega}{2}\sqrt{1-R^2}\delta^2 e^{2i\alpha} \tag{A.15}$$

so that

$$\mathrm{Re}\, B = \pm \frac{\Omega}{2} \sqrt{1 - R^2} \delta^2 \sin(2\alpha) \,. \tag{A.16}$$

We require that $\mathrm{Re}\, B < 0$ and $|\mathrm{Re}\, B| = max$, which gives

$$\begin{aligned} y_{s+} &\rightarrow \sin 2\alpha = -1 \qquad \Rightarrow \alpha_+ = -\frac{\pi}{4} \\ y_{s-} &\rightarrow \sin 2\alpha = +1 \qquad \Rightarrow \alpha_- = +\frac{\pi}{4} \end{aligned} \tag{A.17}$$

If we now note that $\tau_{s-} = -\tau_{s+}$ and if we put

$$\gamma = \frac{R}{1 + \sqrt{1 - R^2}},$$

then Eqs. A.4 and A.6 give

$$A_s(\Omega) = 2 \left[\frac{2\pi}{\Omega \sqrt{1 - R^2}} \right]^{1/2} \cos \left[\left(\frac{\cos^{-1} R}{R} - \ln \gamma \right) \Omega - \frac{\pi}{4} \right] \tag{A.18}$$

which, when substituted into Eq. A.1 gives

$$\begin{aligned} \Delta H \quad = \quad & 2\epsilon \left[\frac{2\Omega\pi}{\sqrt{1 - R^2}} \right]^{1/2} \cos \left[\left(\frac{\cos^{-1} R}{R} - \ln \gamma \right) \Omega - \frac{\pi}{4} \right] \\ & \sin(k\pi - \alpha) \sin \beta \qquad\qquad \Omega < s \end{aligned} \tag{A.19}$$

Appendix B

Particle Trajectories

We give below the particle trajectories that result from the equations of motion 4.1 with $b = \psi_0 = 0$. In these expressions cn and dn are Jacobi elliptic functions, am is the amplitude function and E is the complete elliptic integral of the second kind. We distinguish three cases:

$P_y > 0$ or $P_y < 0$, $\mathcal{E}' > 0$.

These are the crossing trajectories shown in Figs. 4.2-a and -b. They are given by

$$z(t) = \beta_- \mathrm{cn}[\omega_1 t, K_1]$$

$$\begin{aligned} y(t) &= \frac{P_y}{m} t + \\ &\quad \frac{1}{m}(\sqrt{2m\mathcal{E}'} - P_y)\left(\frac{1}{\omega_1 K_1^2} E[\mathrm{am}(\omega_1 t), K_1] - \frac{K_1'^2}{K_1} t\right) \end{aligned}$$

where

$$\beta_\pm^2 = \frac{2ca}{eB_0}(\sqrt{2m\mathcal{E}'} \pm P_y)$$

$$K_1 = \frac{\beta_-}{\sqrt{\beta_+^2 + \beta_-^2}} \quad , \quad K_1' = \frac{\beta_+}{\sqrt{\beta_+^2 + \beta_-^2}}$$

$$\omega_1 = \frac{1}{m}\sqrt{\frac{eB_0}{ca}}(2m\mathcal{E}')^{1/4}.$$

$P_y < 0$, $\mathcal{E}' < 0$.

These are the noncrossing trajectories shown in Fig. 4.2-c. They are given by

$$z(t) = \alpha_+ \mathrm{dn}[\omega_2 t, K_2]$$

$$\begin{aligned} y(t) &= -\frac{|P_y|}{m}t + \\ &\quad \frac{1}{m\omega_2}(|P_y| + \sqrt{2m\mathcal{E}'})E[\mathrm{am}(\omega_2 t), K_2] \end{aligned}$$

where

$$\alpha_\pm^2 = \frac{2ca}{eB_0}(|P_y| \pm \sqrt{2m\mathcal{E}'})$$

$$\omega_2 = \alpha_+ \frac{eB_0}{2mca} \quad , \quad K_2 = \frac{\sqrt{\alpha_+^2 - \alpha_-^2}}{\alpha_+}.$$

$P_y < 0$, $\mathcal{E}' = 0$.

This is the separatrix orbit and is shown in Fig. 4.2-d.

$$z(t) = 2\sqrt{|P_y|\frac{ca}{eB_0}}\mathrm{sech}(\omega t)$$

$$\begin{aligned} y(t) &= -\frac{|P_y|}{m}t + \\ &\quad 2\sqrt{|P_y|\frac{ca}{eB_0}}\tanh(\omega t) \end{aligned}$$

where

$$\omega = \frac{1}{m}\sqrt{|P_y|\frac{eB_0}{ca}}$$

Equivalent expressions for these trajectories can also be found in Speiser, 1965 where an electric field is also included in the $+y$-direction. As Speiser notes, for $b \neq 0$ and $k = 0$ the electric field can be transformed away by the Lorentz transformation

$$E_y' = \gamma(E_y - v_x B_0 b) = 0$$

If $b = 0$, there is no Lorentz transformation that will make $E'_y = 0$. If $k \neq 0$ the transformation does not appear to be useful because of the spatial nonuniformity in x.

Appendix C

Calculation of $\Delta\mu$ for the magnetotail

The change $\Delta\mu$ in the magnetic moment of a particle as it moves from the high-field region into the quasineutral sheet and out into the high-field region again (eg. Figs. 4.8, 4.11) has been calculated before for many different magnetic field configurations (eg. Hastie et. al. 1969; Grad and Van Norton 1962; Cohen et. al. 1978; Birmingham 1984). The method we employ here was first introduced by Hastie et. al. and was extended to more general field configurations by Cohen et. al. The outline we give here is for the general method for the restricted problem (time independent, two-dimensional fields) and follows Birmingham, 1984. We will then apply the results of that calculation to our magnetic fields.

The total change in μ is given by

$$\Delta\mu = \int_{t_i}^{t_f} \frac{d\mu}{dt}\, dt \tag{C.1}$$

where t_i and t_f are two suitably chosen times before and after the neutral layer crossing, at which the particle is far enough from the neutral layer that the magnetic moment is well defined. The integral in Eq. C.1 is evaluated by transforming it to an integral over the particle gyrophase ζ and deforming the contour in the complex ζ-plane.

The time derivative of the magnetic moment is given by

$$\frac{d\mu}{dt} = \frac{d}{dt}\left(\frac{mv_\perp^2}{2B}\right) = \frac{m}{2B}\left(\frac{dv_\perp^2}{dt} - \frac{v_\perp^2}{B}\frac{dB}{dt}\right) \tag{C.2}$$

To evaluate this derivative along the particle trajectory we introduce the following set of unit vectors

$$\hat{b} = \frac{\vec{B}}{|\vec{B}|} \qquad \text{along the field line,}$$

$$\hat{n} = \frac{(\hat{b}\cdot\nabla)\hat{b}}{|(\hat{b}\cdot\nabla)\hat{b}|} \qquad \text{along the the field curvature,}$$

$$\text{and} \quad \hat{\phi} = \frac{\hat{n}\times\hat{b}}{|\hat{n}\times\hat{b}|} \qquad \text{in the normal direction.}$$

The gyrophase is measured from the direction of the field curvature $\hat{n}$ according to the right-hand rule.

Using these coordinates we obtain

$$\begin{aligned}\frac{dv_\perp^2}{dt} &= -v_\perp v_\parallel\Big[v_\perp\Big(\hat{n}\cdot(\hat{n}\cdot\nabla)\hat{b} + \hat{\phi}\cdot(\hat{\phi}\cdot\nabla)\hat{b}\Big) \\ &\quad +2v_\parallel\,\hat{n}\cdot(\hat{b}\cdot\nabla)\hat{b}\cos\zeta \\ &\quad +v_\perp\Big(\hat{n}\cdot(\hat{n}\cdot\nabla)\hat{b} - \hat{\phi}\cdot(\hat{\phi}\cdot\nabla)\hat{b}\Big)\cos(2\zeta)\Big]\end{aligned} \tag{C.3}$$

and

$$\frac{dB}{dt} = (v_\parallel\hat{b} + v_\perp\cos\zeta\,\hat{n})\cdot\nabla B \tag{C.4}$$

so that

$$\begin{aligned}\frac{d\mu}{dt} &= -\frac{mv_\perp}{B}\Big[\Big(\frac{v_\perp^2}{2B}\hat{n}\cdot\nabla B + v_\parallel^2\,\hat{n}\cdot(\hat{b}\cdot\nabla)\hat{b}\Big)\cos\zeta \\ &\quad +\frac{v_\parallel v_\perp}{2}\Big(\hat{n}\cdot(\hat{n}\cdot\nabla)\hat{b} - \hat{\phi}\cdot(\hat{\phi}\cdot\nabla)\hat{b}\Big)\cos(2\zeta)\Big]\end{aligned} \tag{C.5}$$

In deriving the above expressions we have used the fact that $\nabla\cdot\vec{B} = 0$ and that $dv_\perp^2/dt = -dv_\parallel^2/dt$ because of energy conservation. Since we also have

$$\frac{d\zeta}{dt} = \frac{eB}{mc} + \text{H.O.T.} \tag{C.6}$$

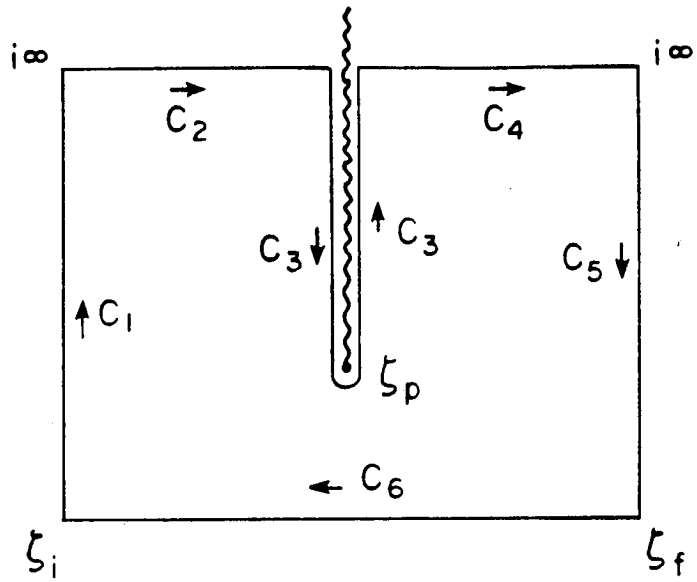

Figure C.1: The integration path for calculating $\Delta\mu$.

(Northrop, 1963), we can rewrite C.5 as

$$\begin{aligned}\frac{d\mu}{d\zeta} &= -\frac{m^2 c v_\perp}{eB^2}\left[\left(\frac{v_\perp^2}{2B}\hat{n}\cdot\nabla B + v_\parallel^2\hat{n}\cdot(\hat{b}\cdot\nabla)\hat{b}\right)\cos\zeta\right.\\ &\left.+\frac{v_\parallel v_\perp}{2}\left(\hat{n}\cdot(\hat{n}\cdot\nabla)\hat{b} - \hat{\phi}\cdot(\hat{\phi}\cdot\nabla)\hat{b}\right)\cos(2\zeta)\right] \qquad \text{(C.7)}\end{aligned}$$

which gives

$$\begin{aligned}\Delta\mu &= -\frac{m^2 c}{e}\mathrm{Re}\int_{\zeta_i}^{\zeta_f} d\zeta\\ &\frac{v_\perp}{B^2}\left[\left(\frac{v_\perp^2}{2B}\hat{n}\cdot\nabla B + v_\parallel^2\hat{n}\cdot(\hat{b}\cdot\nabla)\hat{b}\right)e^{i\zeta}\right.\\ &\left.+\frac{v_\parallel v_\perp}{2}\left(\hat{n}\cdot(\hat{n}\cdot\nabla)\hat{b} - \hat{\phi}\cdot(\hat{\phi}\cdot\nabla)\hat{b}\right)e^{2i\zeta}\right] \qquad \text{(C.8)}\end{aligned}$$

We now calculate the integral in C.8 by going around the pole at ζ_p, where the magnetic field B vanishes, along the path shown in fig. C.1. The contribution of C_2 and C_4 is zero since they are at $i\infty$, and C_1 and C_5 contribute higher order terms (Hastie et. al., 1969). As we shall see next, the integrand of C.8 also includes fractional powers in B so that the two parts of C_3 lie on either

side of a branch cut and therefore give a nonzero contribution. We therefore have

$$\begin{aligned}\Delta\mu &\approx -\frac{m^2c}{e}\mathrm{Re}\int_{C_3} d\zeta \\ &\frac{v_\perp}{B^2}\left[\left(\frac{v_\perp^2}{2B}\hat{n}\cdot\nabla B + v_\parallel^2\,\hat{n}\cdot(\hat{b}\cdot\nabla)\hat{b}\right)e^{i\zeta}\right. \\ &\left.+\frac{v_\parallel v_\perp}{2}\left(\hat{n}\cdot(\hat{n}\cdot\nabla)\hat{b} - \hat{\phi}\cdot(\hat{\phi}\cdot\nabla)\hat{b}\right)e^{2i\zeta}\right]. \qquad \text{(C.9)}\end{aligned}$$

We are now ready to apply C.9 to our model of the magnetotail fields, given by

$$\begin{aligned}B_x &= B_0\tanh\left(\frac{z}{a}\right) \\ B_z &= B_0 b. \qquad \text{(C.10)}\end{aligned}$$

We will need the following relations

$$\begin{aligned}\hat{n}\cdot\nabla B &= -\frac{B_0}{a}\frac{\tanh^2(z/a)\,\mathrm{sech}^2(z/a)}{[b^2+\tanh^2(z/a)]} \\ \hat{n}\cdot(\hat{b}\cdot\nabla)\hat{b} &= \frac{b^2}{a}\frac{\mathrm{sech}^2(z/a)}{[b^2+\tanh^2(z/a)]^{3/2}} \\ \hat{n}\cdot(\hat{n}\cdot\nabla)\hat{b} &= -\frac{b}{a}\frac{\tanh(z/a)\,\mathrm{sech}^2(z/a)}{[b^2+\tanh^2(z/a)]^{3/2}} \\ \hat{\phi}\cdot(\hat{\phi}\cdot\nabla)\hat{b} &= 0.\end{aligned}$$

As we shall see shortly, most of the contribution to the integral in Eq. C.9 comes from the vicinity of the pole where B vanishes. Since the neutral line is, if anywhere, on the $z = 0$ plane, we can use the small-z approximation and put $\tanh(z/a) \approx (z/a)$, $\mathrm{sech}(z/a) \approx 1$. We therefore get

$$\begin{aligned}\hat{n}\cdot\nabla B &= -\frac{B_0^3 z^2}{a^3 B^2} \\ \hat{n}\cdot(\hat{b}\cdot\nabla)\hat{b} &= \frac{B_0^3 b^2}{aB^3} \qquad \text{(C.11)} \\ \hat{n}\cdot(\hat{n}\cdot\nabla)\hat{b} &= -\frac{B_0^3 bz}{a^2 B^3}\end{aligned}$$

where we have used $B = B_0\sqrt{b^2 + (z/a)^2}$. Substituting these expressions into Eq. C.9 we obtain

$$\begin{aligned}\Delta\mu &= \mathrm{Re} - \frac{m^2 c}{e}\int_{C_3} d\zeta\, \frac{\sqrt{2\mu^*}}{B^{3/2}} \\ &\quad \left[\left(-\frac{\mu^* B_0^3 z^2}{a^3 B^2} + (v^2 - 2\mu^* B)\frac{B_0^3 b^2}{aB^3}\right)e^{i\zeta}\right. \\ &\quad \left. -\left(\sqrt{\frac{\mu^*}{2}}\sqrt{v^2 - 2\mu^* B}\,\frac{B_0^3 bz}{a^2 B^{5/2}}\right)e^{2i\zeta}\right] \qquad \text{(C.12)}\end{aligned}$$

Where $\mu^* = \mu/m$ is a reduced magnetic moment per unit mass, the perpendicular velocity is given by $v_\perp = \sqrt{2\mu^* B}$ and the parallel velocity by $v_\parallel^2 = v^2 - 2\mu^* B$. We see now why we were justified in making the small-z approximation. Since we are moving along the imaginary ζ axis the integrant goes as $e^{-\zeta_i}$ and most of the contribution will come from the vicinity of the pole at ζ_p. To find ζ_p we note that

$$\zeta_p = \int^{t_p} \omega\, dt = \frac{e}{mc}\int^{s_p} \frac{ds}{v_\parallel} B$$

If we now substitute $ds = B/(B_0 b)dz$ and $v_\parallel = \sqrt{v^2 - 2\mu^* B}$, and note that the pole occurs at $z_p = \pm iab$, we obtain

$$\begin{aligned}\zeta_p &= \zeta_0 + \frac{e}{mc}\frac{1}{B_0 b}\int_0^{z_p} \frac{B^2}{\sqrt{v^2 - 2\mu^* B}}\, dz \\ &= \zeta_0 + i\frac{eaB_0 b^2}{mcv}\int_0^1 \frac{1 - x^2}{[1 - u'\sqrt{1 - x^2}]^{1/2}}\, dx \qquad \text{(C.13)}\end{aligned}$$

where we have put $z/(ab) = ix$ so that $dz = iab\,dx$, and $u' = 2\mu^* B_0 b/v^2 = \sin^2\theta_0$ where θ_0 is the pitch angle of the particle as it crosses the $z = 0$ plane. The intergal in Eq. C.13 depends only on u'. For small u' it can be expanded to give $F \approx 2/3 + (3\pi/32)u' + (1/15)u'^2$ which for small u' varies slowly in the range 0.66-1.03. The integral can be expressed in terms of elliptic functions but the analytically much simpler expansion in small u' is off by less than a factor of two from the exact value for $u' < 1$ (Coroniti, 1980). From here on

we will therefore assume for simplicity that $F = 1$, so that

$$\zeta_p - \zeta_0 = i\frac{eaB_0b^2}{mcv} = i\kappa^2. \tag{C.14}$$

If we now substitute $\zeta = \zeta_p + i\eta = \zeta_0 + i\kappa^2 + i\eta$ into Eq. C.12 we obtain

$$\begin{aligned}\Delta\mu &= -\frac{m^2c}{e}\mathrm{Im}\int_{C_\eta} d\eta\frac{\sqrt{2\mu^*}}{B^{3/2}} \\ &\left[\left(-\frac{\mu^* B_0^3 z^2}{a^3B^2} + (v^2 - 2\mu^* B)\frac{B_0^3b^2}{aB^3}\right)\cos\zeta_0 e^{-\kappa^2}e^{-\eta}\right. \\ &\left.-\left(\sqrt{\frac{\mu^*}{2}}\sqrt{v^2 - 2\mu^* B}\frac{B_0^3bz}{a^2B^{5/2}}\right)\cos(2\zeta_0)e^{-2\kappa^2}e^{-2\eta}\right].\end{aligned} \tag{C.15}$$

Where C_η is the contour in the η-plane corresponding to the contour C_3 in the ζ-plane (cf. Fig. C.2). Dropping the $\exp(-2\kappa^2)$ term as second order in the exponentially small parameter $\exp(-\kappa^2)$ and keeping only the most divergent term $B^{-9/2}$ from the remaining expression we obtain

$$\Delta\mu = -\frac{m^2c}{e}\mathrm{Im}\int_{C_\eta} d\eta\,\sqrt{2\mu^*}v^2\frac{B_0^3b^2}{a}B^{-9/2}\cos\zeta_0 e^{-\kappa^2}e^{-\eta} \tag{C.16}$$

To evaluate this integral we need to relate B and η. To do this we first note that

$$\begin{aligned}B^2 &= (B_0)^2\left[b^2 + \left(\frac{z}{a}\right)^2\right] = \frac{B_0^2}{a^2}(z - z_p)(z - z_p') \\ &\frac{B_0^2}{a^2}(z - z_p)[(z - z_p) + z_p - z_p'] \approx 2\frac{B_0^2}{a^2}z_p(z - z_p) \\ &= 2i\frac{B_0^2b}{a}(z - z_p)\end{aligned} \tag{C.17}$$

where the pole we are expanding around is at $z = z_p = 2iab$ the other pole is at $z = z_p' = -iab$, and we only keep first order terms. To relate $z - z_p$ to η we use Eq. C.13 to obtain

$$\begin{aligned}\zeta - \zeta_p &\approx \frac{e}{mcB_0b}\int_{z_p}^{z}\frac{B^2}{v}dz = i\frac{eB_0}{mcva}(z - z_p)^2 \\ &= i\frac{1}{a\rho}(z - z_p)^2\end{aligned} \tag{C.18}$$

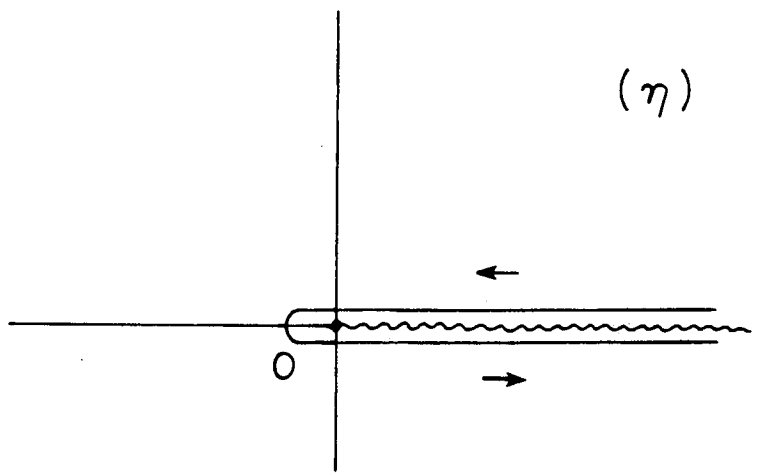

Figure C.2: The integration path for the η integration.

where we used the expansion

$$(v^2 - 2\mu^* B)^{-1/2} = (v^2 - v_\perp^2)^{-1/2} \approx \frac{1}{v}\left(1 + \frac{2\mu^* B}{v^2}\right)$$

and only kept the zeroth order term in B. Since η is defined by $\zeta - \zeta_p = i\eta$ we can use C.18 and C.17 to get

$$B^4 \approx 4B_0^4 \epsilon b^2(-\eta) \tag{C.19}$$

which gives

$$B^{-9/2} = 4^{-9/8} B_0^{-9/2} \epsilon^{-9/8} b^{-9/4} (-\eta)^{-9/8}$$

Substituting this expression into Eq. C.16 we obtain

$$\begin{aligned} \Delta\mu &= -\mathrm{Im}\left[\int_{C_\eta} (-\eta)^{-9/8} e^{-\eta}\, d\eta\right] \frac{mcv}{eB_0 a} \sqrt{2\mu m v^2} \\ &\quad B_0^4 b^2 2^{-9/4} B_0^{-9/2} \epsilon^{-9/8} b^{-9/4} e^{-\kappa^2} \cos\zeta_0 \\ &= \frac{\pi}{2^{3/4}\Gamma(9/8)} \sqrt{\frac{\mu E}{B_0 b}} \kappa^{1/4} e^{-\kappa^2} \cos\zeta_0. \end{aligned} \tag{C.20}$$

The path for the η integration is shown in Fig. C.2. It is related to the Γ-function via the Hankel integral.

REFERENCES

Akasofu, S.-I., The solar wind magnetosphere energy coupling and magnetospheric disturbances, *Planet. Space Sci.* **28**, 459, 1980.

Akasofu, S.-I., Energy coupling between the solar wind and the magnetosphere, *Space Sci. Rev.* **28**, 121, 1981.

Arfken, G., Mathematical methods for physicists, second edition, *Academic Press*, 376, 1970.

Birmingham, T.J., Pitch angle diffusion in the Jovian magnetodisc, *J. Geophys. Res.* **89**, 2699, 1984.

Biskamp, D. and H. Welter, Coalescence of magnetic islands, *Phys. Rev. Lett.* **44**, 1069, 1980.

Brunel, F., T. Tajima and J.M. Dawson, Fast magnetic reconnection processes, *Phys. Rev. Lett.* **49**, 323, 1982.

Büchner, J. and L.M. Zelenyĭ, Deterministic chaos in the dynamics of charged particles near a magnetic field reversal, *Phys. Lett. A* **118**, 395, 1986.

Büchner, J. and L.M. Zelenyĭ, Chaotisation of the electron motion as the cause of an internal magnetotail instability and substorm onset, *J. Geophys. Res.* **92**, 13456, 1987.

Chen, J. and P. Palmadesso, Chaos and nonlinear dynamics of single-particle orbits in a magnetotail-like magnetic field, *J. Geophys. Res.* **91**, 1499, 1986.

Chirikov, B.V., A universal instability of many-dimentional oscillator systems, *Physics Reports* **52**, 263, 1979.

Coppi, B., G. Laval and R. Pellat, Dynamics of the geomagnetic tail, *Phys. Rev. Lett.* **16**, 1207, 1966.

Coroniti, F.V., On the tearing mode of quasineutral sheets, *J. Geophys. Res.* **85**, 6719, 1980.

Coroniti, F.V., Explosive tail reconnection: the growth and expansion phases of magnetospheric substorms, *J. Geophys. Res.* **90**, 7427, 1985.

DeCoster, R.J. and L.A. Frank, Observations pertaining to the dynamics of the plasma sheet, *J. Geophys. Res.* **84**, 5099, 1979.

Dobrowolny, M., Instability of a neutral sheet, *Nuovo Cimento* **B 55**, 427, 1968.

Drake, J.F, and Y.C. Lee, Kinetic theory of tearing instabilities, *Phys. Fluids* **20**, 1341, 1977.

Drake, J.F., Kinetic theory of $m = 1$ internal instabilities, *Phys. Fluids* **21**, 1777, 1977.

Dungey, J.W., Conditions for the occurrence of electrical discharges in astrophysical systems, *Phil. Mag.*, **44**, 725, 1953.

Dungey, J.W., Interplanetary magnetic field and the auroral zones, *Phys. Rev. Lett.* **6**, 47, 1961.

Dupree, T.H., Nonlinear theory of drift-wave turbulence and enhanced diffusion, *Phys. Fluids* **10**, 1049, 1967.

Esarey, E. and K. Molvig, A turbulent mechanism for substorm onset in the earth's magnetotail, *Geophys. Res. Lett.* **14**, 367, 1987.

Escande, D.F., Stochasticity in classical hamiltonian systems: Universal aspects, *Phys. Rep.* **121**, 167, 1985.

Escande, D.F., Large scale stochasticity in hamiltonian systems, in *Hamiltonian dynamical systems*, R.S. MacKay and J.D. Meiss ed., Adam Hilger, Bristol, 1987.

Furth, H.P., Instabilities due to finite resistivity or finite current-carrier mass, in *Advanced Plasma Theory*, M.N. Rosenbluth ed., Academic Press, New York, 159, 1962.

Furth, H.P., J. Killeen and M.N. Rosenbluth, Finite resistivity instabilities of a sheet pinch, *Phys. Fluids* **6**, 459, 1963.

Galeev, A.A. and L.M. Zelenyĭ, Tearing instability in plasma configurations, *Sov. Phys. JETP* **43**, 1113, 1976.

Galeev, A.A., Reconnection in the magnetotail, *Space Sci. Rev.* **23**, 411, 1979.

Hagege, K., G. Laval and R. Pellat, Interaction between high-frequency turbulence and magnetospheric micropulsations, *J. Geophys. Res.* **78**, 3806, 1973.

Ham, T.S. and R.M. Kulsrud, Forced magnetic reconnection, *Phys. Fluids* **28**, 2412, 1985.

Harris, E.G., On a plasma sheeth separating regions of oppositely directed magnetic field, *Nuovo Cimento* **23**, 115, 1962.

Horton, W., Anomolous ion Construction from toriodal drift waves, *Plasma Phys.* **23**, 1107,1981.

Horton, W., Onset of stochasticity and the diffusion approximation in drift waves, *Plasma Phys. and Controlled Fusion* **27**, 937, 1985.

Horton, W. and T. Tajima, Linear theory of driven reconnection, *J. Geophys. Res.* **93**, 2741, 1988.

Huba, J.D., N.T. Gladd and K. Papadopoulos, Lower hybrid drift wave turbulence in the distant magnetotail, *J. Geophys. Res.* **83**, 5217, 1978.

Kadomtsev, B.B., Plasma turbulence, Academic Press, London, 1965.

Kim, J.-S. and J. Cary, Charged particle motion near a linear magnetic null, *Phys. Fluids* **26**, 2167, 1983.

Kleva, R.G. and J.F. Drake, Stochastic $\vec{E} \times \vec{B}$ particle transport, *Phys. Fluids* **27**, 1686, 1984.

Laval, G., R. Pellat, and M. Vuillement, Instabilites electromagnetiques des plasmas sans collisions, IAEA, VIENNA, 1965.

Lembège, B., and Pellat, Stability of a thick two-dimentional quasineutral sheet, *Phys. Fluids* **25**, 1995, 1982.

Lyons, L.R. and T.W. Speiser, Ohm's law for a current sheet, *J. Geophys. Res.* **90**, 8543, 1985.

Lyons, L.R. and D.W. Williams, Quantitative aspects of Magnetotail Physics, D. Reidel, 1984.

MacKay, R.S., J.D. Meiss and I.C. Persival, Transport in Hamiltonian systems, in *Hamiltonian dynamical systems*, R.S. MacKay and J.D. Meiss ed., Adam Hilger, Bristol, 1987.

Meiss, J.D., Transport near the onset of stochasticity, *Particle accelerators* **19**, 9, 1986.

Quest, K.B., and F.V. Coroniti, Linear theory of tearing in high-β plasma *J. Geophys. Res.* **86**, 3299, 1981.

Rosenbluth, M.N., H.L. Berk, I. Doxas and W. Horton, Effective diffusion in laminar convective flows, *Phys. Fluids* **30**, 2636, 1987.

Sato, T. and T. Hayashi, Externally driven magnetic reconnection and a powerful magnetic energy converter, *Phys. Fluids* **22**, 1189, 1979.

Shindler, K., A theory of the substorm mechanism, *J. Geophys. Res.* **79**, 2803, 1974.

Sonnerup, B.U.Ö., Adiabatic particle orbits in a magnetic null sheet, *J. Geophys. Res.* **76**, 8211, 1971.

Speiser, T.W., Particle trajectories in model current sheets; 1. Analytical solutions, *J. Geophys. Res.* **70**, 4219, 1965.

Speiser, T.W., Particle trajectories in model current sheets; 2. Applications to auroras using a geomagnetic tail model, *J. Geophys. Res.* **72**, 3919, 1967.

Speiser, T.W., Kinetic aspects of tail dynamics, in *Magnetotail Physics*, T.Y. Liu ed., John Hopkins University Press, 277, 1987.

VITA

Isidoros Doxas was born in Pireus, Greece on November 25, 1959 the son of George and Margaret Doxas. After graduating from the Second Zografou High School for Boys, he heeded the words of Horace Greeley and decided to 'go west'. After completing his GCE's in Athens, Greece he went to London, England, and to Queen Mary College of the University of London, where he earned his Bachelor of Science degree in Physics, in June of 1981. He then went to New York City and to Columbia University where he received his Master of Arts degree in Physics, in May of 1983. Continuing his westward trek he went to Austin, Texas and, in the Fall of 1983, entered the University of Texas where he has been employed as a research assistant since January 1984. He was married to Ronda Kathleen Garvin on April 2, 1988.

Permanent address: Pentelis 61
Amarousion, Athens
Greece

This dissertation was typeset[1] with LaTeX by the author.

[1] LaTeX document preparation system was developed by Leslie Lamport as a special version of Donald Knuth's TeX program for computer typesetting. TeX is a trademark of the American Mathematical Society. The LaTeX macro package for The University of Texas at Austin dissertation format was written by Khe-Sing The.